

Aus dem Zentrum für Medizinische Forschung
der Medizinischen Fakultät Mannheim
Direktor: Prof. Dr. med. Norbert Gretz

3D fluorescence imaging of the lung

Inauguraldissertation
zur Erlangung des medizinischen Doktorgrades
der
Medizinischen Fakultät Mannheim
der Ruprecht-Karls-Universität
zu
Heidelberg

vorgelegt von
Quanchao Sun

aus
Jiangxi, China
2020

Dekan: Prof. Dr. med. Sergij Goerd
Referent: Prof. Dr. med. Norbert Gretz

TABLE OF CONTENTS

	Page
ABBREVIATIONS	1
1 INTRODUCTION	2
1.1 Optical tissue clearing and labeling	2
1.2 Expansion microscopy.....	7
1.3 Microscopic imaging	9
1.4 Data storage and management	10
1.5 Lung and lung metastases	11
1.6 Aim of our project	14
2 MATERIAL AND METHOD	15
2.1 Animals:.....	15
2.2 Metastases specimen.....	15
2.3 Materials:.....	15
2.3.1 ECi based OTC:.....	15
2.3.2 ExM:	16
2.3.3 Antibodies:.....	16
2.4 Perfusion procedure and mouse lung extracting	17
2.5 ECi based OTC	20
2.6 ExM and 3D immunofluorescence staining	20
2.6.1 Infiltration of Amplifying Hydrogel Solution	20
2.6.2 Polymerization	21
2.6.3 Preparation of sections with vibratome	22
2.6.4 Denaturation	22
2.6.5 3D Immunofluorescence staining.....	23
2.7 Deparaffinization of tissue from paraffin-embedded blocks	24
2.8 Microscopy and data acquisition.....	24
2.8.1 Sample preparation and RI matching	24
2.8.2 3D image acquisition	25

2.9	Data storage and quantitative 3D cell morphometry of lung metastases.....	26
3	RESULTS.....	27
3.1	3D fluorescence imaging of MHI148-PEI-stained lung vasculature after ECi based OTC	27
3.2	3D immunofluorescence visualization of the normal lung by ExM	32
3.3	3D imaging of the vasculature in paraffin-embedded lung blocks	41
3.4	3D imaging of the microvasculature 10 year old in paraffin-embedded lung metastases	44
3.5	3D visualization and quantitative analysis of the neutrophil cell distribution in paraffin-embedded lung metastases	48
4	DISCUSSION	52
4.1	Animal perfusion.....	52
4.2	ECi based OTC	54
4.3	ExM and 3D immunofluorescence.....	57
4.4	ExM with lung metastases from paraffin blocks.....	60
5	SUMMARY	65
6	REFERENCES	66
7	APPENDIX (PUBLICATION)	76
8	CURRICULUM VITAE.....	77
9	ACKNOWLEDGMENTS.....	78

ABBREVIATIONS

2D	Two-dimensional
3D	Three-dimensional
3DISCO	3D imaging of solvent cleared organs
α -Ac-Tub	Acetylated α -tubulin
AHS	Amplifying hydrogel solution
AQP5	Aquaporin5
BW	Body weight
CLARITY	Clear Lipid-exchanged acrylamide-hybridized rigid imaging compatible Tissue gel
CUBIC	Clear, unobstructed brain imaging cocktails and computational analysis
ECi	Ethyl cinnamate
ExM	Expansion microscopy
ExPath	Expansion microscopy pathology
iDISCO	Immunolabeling-enabled 3D imaging of solvent cleared organs
LCFM	Laser confocal fluorescence microscopy
LSFM	Light sheet fluorescence microscopy
NA	Numerical aperture
OTC	Optical tissue clearing
PACT	Passive clarity technique
PBS	Phosphate buffered saline
PFA	Paraformaldehyde
RI	Refractive index
SeeDB	See deep brain
SDS	Sodium dodecyl sulfate.
SPF	Specific pathogen free
SWITCH	System-wide control of interaction time and kinetics of chemicals
WD	Working distance

1 INTRODUCTION

Conventional histological methods, such as Hematoxylin and eosin (H&E) staining, immunohistochemistry and in situ hybridization, provide abundant information about the morphological characteristics of cells and tissues. These technologies with bright-field microscopy are the foundation for histopathological diagnosis that helps the pathologist to examine inflammation, fibrosis, malignancy, and so on (Holt et al., 1993; Jin and Lloyd, 1997). However, they can provide only two-dimensional (2D) planar images that lack the three-dimensional (3D) structures consisting of a variety of constituents in tissue. For instance, in clinical pathology departments, only the typical lesions observed by a macroscopic detection are further examined. There may be additional lesions in the area not visible to the naked eyes still remaining to be diagnosed (Fujisawa et al., 2015).

To overcome this limitation and to get a more comprehensive pathological diagnosis, serial sections and scans followed by reconstruction of 3D images via computer software were established for large sample examinations (Wellings and Jensen, 1973; Wellings et al., 1975). However, this section-based 3D imaging approach failed to obtain accurate internal 3D structures of thick tissues. Especially structures on the cellular-level are difficult to recognize due to the inevitable discontinuity disruption of structure. Consequently, the cutting may lead to tissue deformation and a loss of detailed anatomical information especially from the edge of each slice. What is even worse, this method is labor-intensive, time consuming, expensive and needs a high level of training and expertise (Booth et al., 2015). Therefore, high-resolution 3D volume imaging of whole mount tissue will make a big difference to visualize complex structures such as immune cells distribution, cancer cell accumulation, vasculature and lymphatic vessels, which are difficult to investigate in 2D planar sections.

1.1 Optical tissue clearing and labeling

A possible solution has been reported already in 1914 (Spalteholz, 1914). This approach makes biological specimens optically transparent by reducing the refractive index (RI) difference within the tissues to enable 3D imaging. The whole process of RI adjustment and lipid removal is named optical tissue clearing (OTC) (Conchello and Lichtman, 2005). In general, OTC processing consists of a series of steps, such as

pretreatment, permeabilization, immunolabeling, RI matching, and imaging with advanced laser confocal fluorescence microscopy (LCFM) or light sheet fluorescence microscopy (LSFM). Normally, the light could not travel in straight lines after entering a tissue. It is absorbed and reflected by the tissue when the tissue has different RIs and contains lipids. After OTC the light scattering is reduced and allows a deeper laser penetration during scanning by using LCFM or LSFM, thus enables 3D deep imaging of whole mount tissues (Reyraud et al., 2008; Richardson and Lichtman, 2015).

Recently, there is a growing interest in optimizing OTC methods for 3D imaging of labeled structures in large samples or even entire organs. This allows us not only to study the 3D structure of normal tissues in unprecedented details, but also to investigate sparsely distributed pathological hallmarks in diseased models, for example, amyloid plaques in the brain of Alzheimer's disease mouse models (Murray et al., 2015; Susaki et al., 2014). Allowing us to access and assess the anatomic structures and functions in a broad range of biological systems, including the peripheral nervous system, more precisely than before (Tomer et al., 2012).

Various kinds of OTC protocols have been reported. They can be divided into three main categories according to the different working principles: (1) simple RI matching, (2) delipidation combined with dehydration (solvent-based) or hyperhydration (aqueous-based) followed by RI matching, and (3) tissue-gel hybridization followed by delipidation and RI matching, as shown in **Fig. 1**. (Costantini et al., 2019; Greenbaum et al., 2017; Seo et al., 2016).

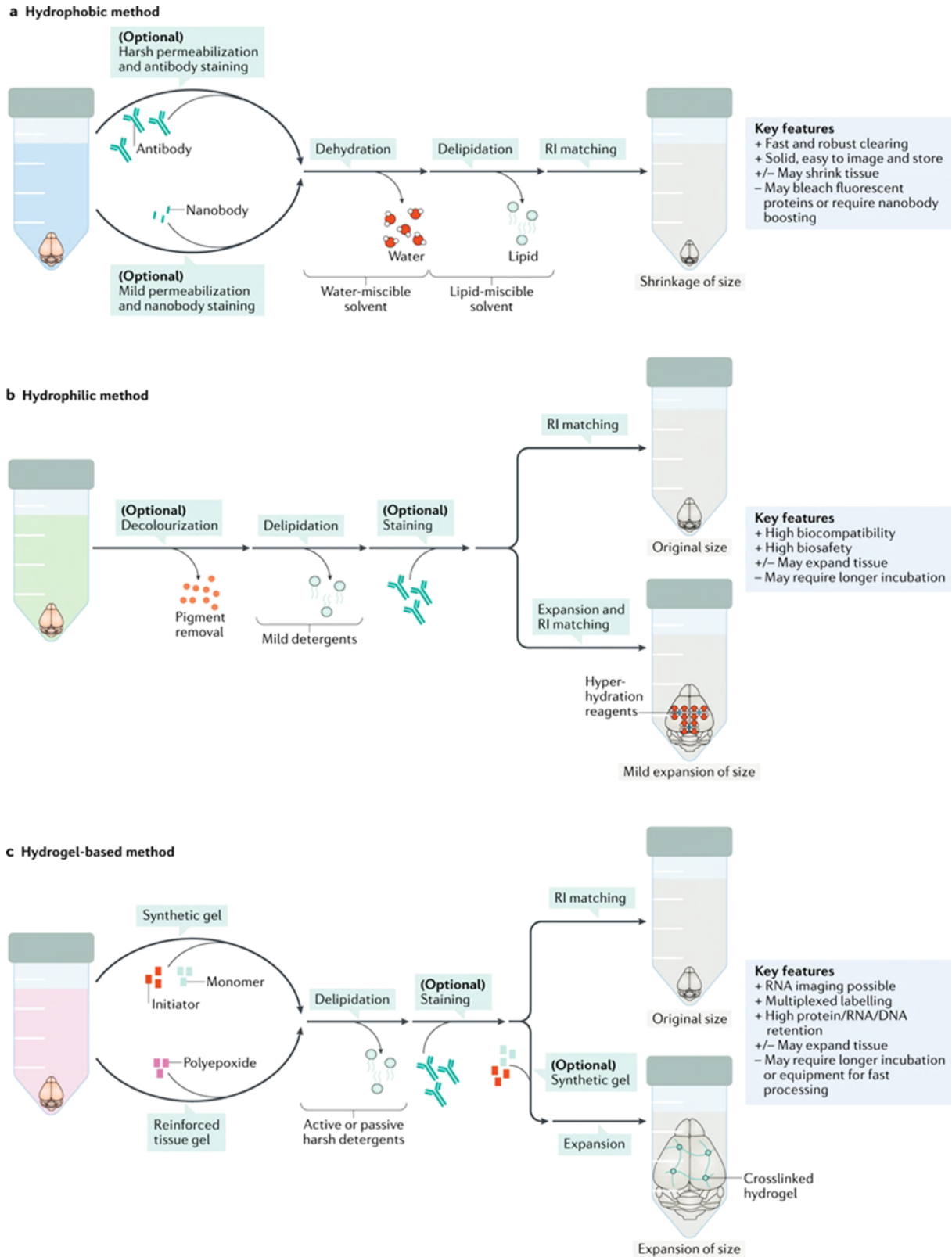


Figure 1. Three main categories of OTC according to the different working principles (Ueda et al., 2020).

1.1.1. Simple refractive index matching

The simplest approach to increase tissue transparency is to reduce light scattering by matching the RIs of the tissue constituents to one medium. Although the RIs of tissue components are different (protein: RI~1.43; lipids: RI~1.44; water: RI~1.33), the RI of overall tissue is almost 1.4~1.5 (Seo et al., 2016). Rendering the tissue transparency by replacing water with high concentration solutions of formamide (ClearT, RI~1.44), formamide and polyethylene glycol (PEG) (ClearT2, RI~1.44) or fructose with α -thioglycerol (SeeDB, RI~1.49) are easy to implement, reversible and cost effective (Costa et al., 2018; Ke et al., 2013; Kuwajima et al., 2013). Among these solutions, SeeDB exhibits the best ability to preserve fluorescence intensity because fructose does not disrupt the fluorescence of proteins. However, they are all limited to the labeled samples since most of the molecular probes penetrate into specimens hardly in these ways (Boutin and Hoffman-Kim, 2015).

1.1.2. Delipidation combined with dehydration/hyperhydration followed by RI matching

The main reason for the tissue opacity is that the lipids cause light scattering in the biological tissue. Removing lipids from the specimen is helpful to match the RI of tissue and make the tissue transparent. In order to achieve delipidation, organic solvents and denaturants or other detergents are utilized. Each of them have to be applied together with dehydration and hyperhydration (d'Esposito et al., 2015).

The organic solvent-based methods show a better clearing effect and are normally faster as compared with the simple immersion protocols mentioned above. For example, dibenzyl ether-based 3DISCO or iDISCO can make a whole mouse brain transparent in 2-3 days to enable the whole mount 3D imaging by using the LSFM. On the other side, the volumes of tissues after dehydration and delipidation are always reduced, which may be good for the 3D imaging for saving scanning time. However, the researchers must be careful with the dramatic signal loss of fluorescent proteins and the toxic organic solvents (Erturk et al., 2012; Renier et al., 2014).

Aqueous-based solution containing detergent (e.g. Triton X-100) and denaturants (e.g. urea) in ScaleS, ScaleA2, and CUBIC can remove lipids and denature endogenous proteins. These processes accelerate hyperhydration of tissue components and match

the RI of the overall tissue block to ~ 1.38 to increase tissue transparency (Hama et al., 2015; Hama et al., 2011; Susaki et al., 2015). Apart from the fact that the tissue microstructure may be damaged by the hydration-induced swelling, these methods shows strong clearing capability and are easy to carry out.

1.1.3. Tissue-gel hybridization followed by delipidation and RI matching

In view of the microstructure and biomolecules that can be destroyed during the application of clearing protocols involving delipidation, a gel network was developed to ensure the integrity of structure and molecules. Delipidation can be achieved by electrophoresis, normal or high temperature incubation, and perfusion with SDS solution (Lee et al., 2014). For example, the gel protected-tissue can undergo strong delipidation reaction while the structure and molecule are well preserved in CLARITY and variants of this protocol like PACT, PARS and SWITCH (Wan et al., 2018; Xu et al., 2019). Combined with RI-matching solution immersion (e.g. glycerol, commercially FocusClear, RIMS or CUBIC-mount), the tissue will become very transparent (Jensen and Berg, 2017; Moy et al., 2013; Yu et al., 2017). However, depending on how lipids are removed, the total clearing time varies from 2-3 days (CLARITY) to more than one month (PACT) for a mouse brain (Woo et al., 2016). The delipidation not only makes the tissue transparent combined with RI-matching but also accelerates the diffusion of molecular probes in further staining steps.

1.1.4. Labeling

How to label the target structure or molecules of interest inside the transparent tissue with probes (normally fluorescent protein conjugated antibodies) is critical for 3D imaging. First, the fluorescent proteins should be well preserved throughout the whole clearing process. Second, it always takes such a long time to complete the labeling in a large volume specimen because the conventional staining methods always rely on slow diffusion of molecular probes (Renier et al., 2014). Accelerating the transportation rate of probes into thick tissue has an enormous effect on spreading use/promotion of clearing protocols. The new developed techniques optimize these issues based on the following principles: (1) increasing tissue permeability, such as reducing fixation time, applying detergents or repeating dehydration-rehydration, (2) increasing probe concentration and improving probe target binding reaction kinetics and (3) applying

external power, such as pressure or force on electrically charged solutions (Palmer et al., 2018; Syed et al., 2017).

In the present research, we have applied a novel modified OTC protocol, which uses ethyl-3-phenylprop-2-enoate (ethylcinnamate, ECi) as a non-toxic and cheap clearing solvent for 3D imaging of the lung by using LCFM and LSM. This method is fast, simple, non-special instrument requiring and compatible with a near-infrared dye MHI148-PEI staining, which allows vessel staining.

1.2 Expansion microscopy

Expansion microscopy (ExM) is a recently described advanced method that enables 3D high-resolution imaging with conventional microscopes by physically expanding tissue isotropically via a series of chemical processes (Chen et al., 2015). In ExM, biomolecules and labels are chemically equipped with anchors that enable them to be fixed to a swellable polymer or hydrogel, which is synthesized evenly throughout the tissue. The peptide bonds in the gel-embedded tissues are mechanically disrupted by high temperature denaturation or proteolysis, and then tissues are swollen by washing with deionized water (**Fig. 2**). Because of this process, molecules will be separated apart from each other and samples are uniformly enlarged to enable them to be easily resolved (Chen et al., 2015; Chozinski et al., 2016; Tillberg and Chen, 2019). The whole process is analogous to drawing a picture on a balloon and then blowing it up: the ink particle will be distributed quite evenly on the surface, but their spatial organization is relatively well retained. However, if the mechanical homogenization of the sample is not performed adequately, the tissue and cell structure will be broken during ExM process (Gao et al., 2017).

Because the lipids that cause light scattering are not anchored to the hydrogel, they can be removed by a relatively gentle denaturation step using sodium dodecyl sulfate (SDS) which preserves most biomolecules well. The samples are expanded in water after denaturation, and the final specimens are mostly composed of water. A byproduct of this physical mechanism is that tissues are completely transparent and optical aberration free, which is the same as OTC. The final RI of tissue is about 1.33 after ExM, so water can serve as the mounting medium during imaging. Combined with the

conventional microscopes and probes, it allows the 3D structure analysis of thick tissues at high-resolution (Cahoon et al., 2017). Another benefit of ExM is that the de-bonded biomolecules are far away from each other, which facilitates antibodies diffusion in specimens and makes room for the chemical reaction around the molecules. The staining can be carried out in either a pre- or post-expansion state. In post-expansion staining protocol, since probes do not go through the gel embedding and homogenization process, any dye or antibodies should be suitable. However, some fluorescent proteins and dyes will be degraded in the pre-expansion staining protocol, so it is necessary to test the labeling in advance (Chen et al., 2015; Chozinski et al., 2016; Chozinski et al., 2018).

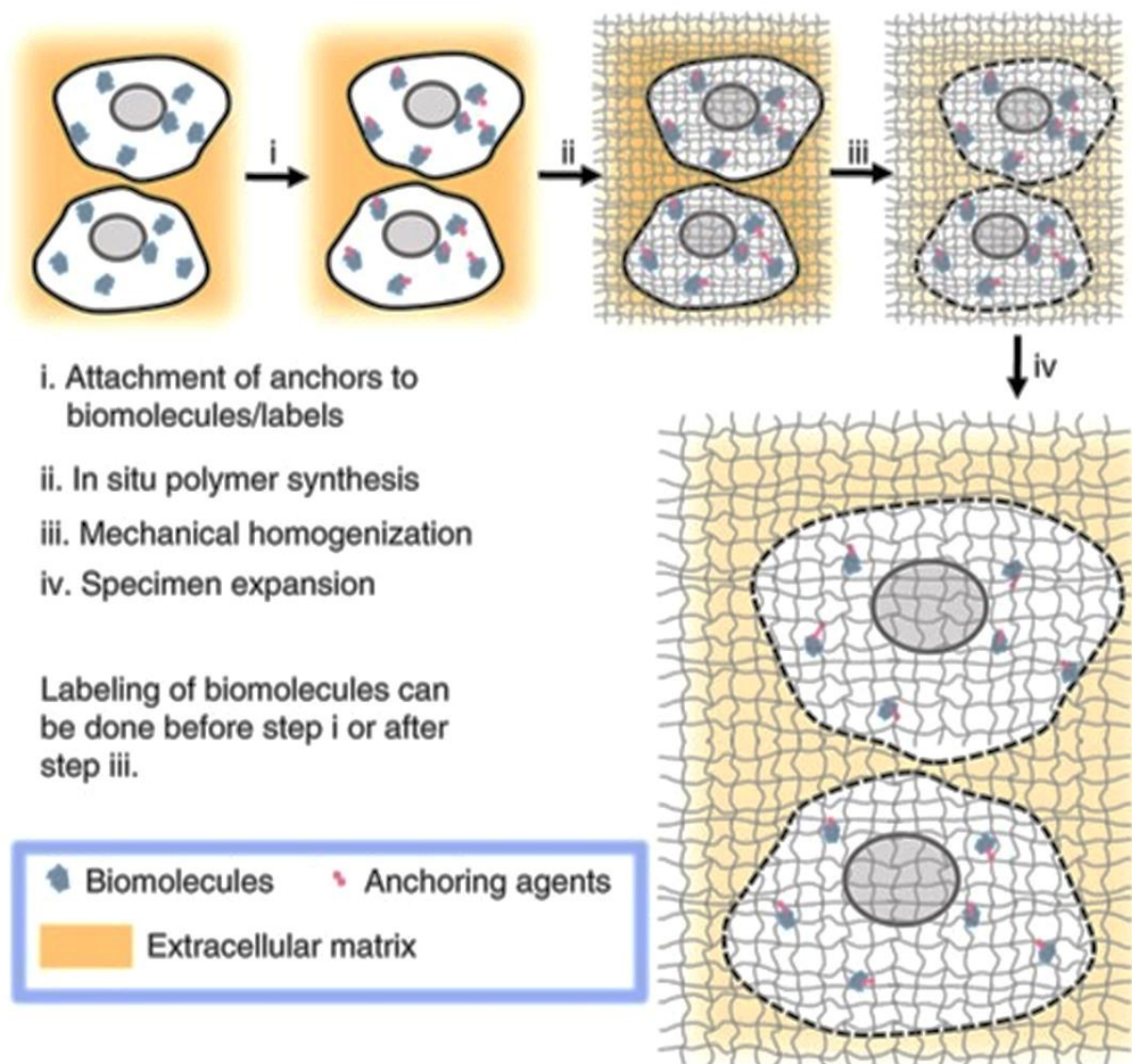


Figure 2. Schematic of the ExM process (Wassie et al., 2019).

1.3 Microscopic imaging

The goal of microscopic imaging is to get 3D visualization of thick tissues or even whole organs with a reasonable resolution in a high-throughput manner after OTC (Helmchen and Denk, 2005). The most commonly used instrument for small volume tissues is standard confocal microscopy, which is also characterized with a real high-resolution 3D imaging. The reason why it is limited to only a small volume tissue is that the confocal microscope scans the samples point by point, which can result in severe fluorescence photobleaching and quite long imaging time (Germroth et al., 1995; Silvestri et al., 2016). These problems are now addressed with the emerging technology: LSFM, which reduces the laser intensity of excitation on the tissue and allows for fast scanning by simultaneous illumination of a single thin plane. In this way, the photobleaching and photo-toxic effects are reduced significantly. LSFM is 10-100 times faster than the traditional confocal microscope that can image an intact mouse organ in only few hours (**Fig. 3**). Nevertheless, the resolution of the data obtained by LSFM is always inferior to confocal microscopy (Chakraborty et al., 2019; Dodt et al., 2007; Treweek et al., 2015).

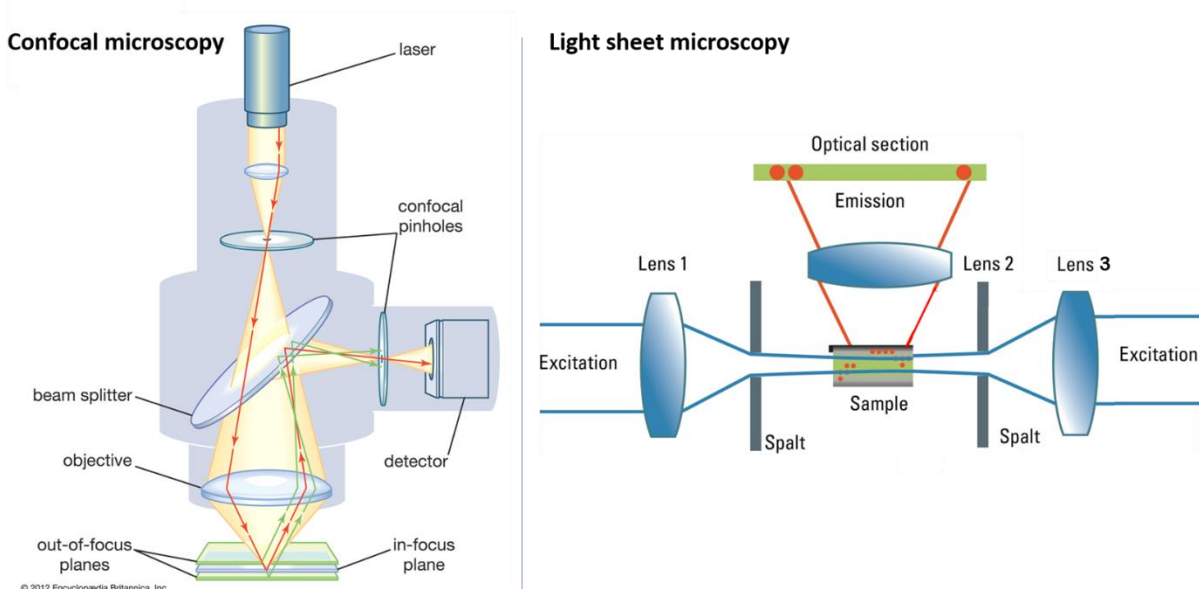


Figure 3. Working principle of LCFM and LSFM. (<https://www.britannica.com/technology/confocal-microscope> and <https://www.leica-microsystems.com/science-lab/confocal-and-digital-light-sheet-imaging/>; date of download:

01/12/2020)

Relevant parameters of the objectives, such as numerical aperture (NA), working distance (WD) and RI of immersion medium, are critical impact factors in 3D imaging microscopy. The common objectives with high NA can achieve high resolution scanning, but they are always designed with short and limited WD (Richardson and Lichtman, 2015; Ryan et al., 2017; Wang et al., 2019). After removing the laser penetration limit caused by light scattering via OTC, the short WD of objectives become the main limiting factor for 3D imaging. As mentioned above, the cleared samples have different RIs according to the different OTC methods applied. The mismatching between objective, mounting medium and cleared tissue will result in poor image quality and lead to a high degree of spherical aberration (Yu et al., 2018). Therefore, an objective precisely well matched with the RI of the cleared sample and mounting medium is very important for 3D imaging. To address this problem, long WD and high NA objectives with specific or tunable RI value to meet the requirement of different OTC methods are designed, and most of them are now commercially available. For example, XLPLN10xSVMP (Olympus, 10 x NA 0.6; WD 8.0 mm; RI~1.33-1.52) for clearing agents such as ScaleView, CLARITY and SeeDB. HC FLUOTAR L IMM motCORR VISIR (Leica, 25 x NA 1.0; WD 6.0 mm; RI = 1.457) for CLARITY-treated samples. LUCPLFLN 20 x corrected (Olympus, 20 x NA 0.45; WD 5 mm; RI = 1.56) for DISCO cleared samples (Marx, 2014; Pan et al., 2016; Tomer et al., 2014).

1.4 Data storage and management

3D imaging always produces tens to hundreds of gigabytes of data contents per thick sample or organ. Not only powerful computational ability and high-resolution screens for 3D visualization are needed, but also sufficient data transfer and storage capacity are critical technological issues that need to be addressed in the data handling. A workstation with enough memory space and stable net-work-attached storage is helpful to access and process the acquired data easily (Greenbaum et al., 2017). Nowadays, the advanced commercial Cloud services also make large data sharing with distant groups possible, but an efficient data transfer and sufficient storage capacity need to be improved.

For data analysis, the open-source platform Fiji (ImageJ, <https://imagej.net/Fiji>), including a set of useful plugins such as image filters, versatile file-format converter

and 3D viewer, is a powerful software for image processing. Other commercial softwares for data visualization and statistical analysis, such as MATLAB (<https://de.mathworks.com/products/matlab.html>), Imaris (<https://imaris.oxinst.com/>), VesSAP (<http://discotechnologies.org/VesSAP/>) and Amira (<https://www.thermofisher.com/de/de/home/industrial/electron-microscopy/electron-microscopy-instruments-workflow-solutions/3d-visualization-analysis-software/amira-life-sciences-biomedical.html>), can also be used for processing and quantitative analysis in 3D images. However, all of them require file-type conversion for further processing and focus on one specific issue, such as stitching, visualization or deconvolution. Therefore, it would make sense to develop a unified computational network and a shared standard file format.

1.5 Lung and lung metastases

Anatomical structures of both normal and diseased lungs were analyzed in this project. In order to identify the different structures better, a brief histological update about normal lung and lung metastases will be presented in the next paragraph.

The main pulmonary artery originates from the right ventricle and then divides into the left and right main pulmonary artery branches, of which the diameter is half of the main pulmonary artery. The left and right main pulmonary artery then further divide into smaller branches named as lobe arteries before entering the lung. After that, each lobe artery further subdivides into irregular small branches corresponding to the bronchi. All of the artery and vein branches are embedded in the lung and show up as a “vessel tree” (Murillo et al., 2012; Townsley, 2012).

The normal lungs are an air-filled organ responsible for respiration in both side of the chest. The bronchi conduct inhaled air into the lungs and then divide into smaller and smaller bronchioles, finally ending up in clusters of microscopic alveoli (Persson, 1996). They are embedded in the lung as a “bronchial tree” (progressive bronchial branching). The proximal airway is composed of ciliated cells, secretory club cells, goblet cells, undifferentiated basal cells and neuroendocrine cells; the distal airway is mainly composed of type I and type II alveolar epithelial cells. There are also some other cell types in the lung which include smooth muscle cells, fibroblasts, endothelial cells and various kinds of immune cells (Reid, 1965). The deoxygenated blood

collected from body organs are pumped by the right ventricle into the left and right main pulmonary arteries, which branch into smaller pulmonary arteries and capillaries that spread through the lungs. Oxygen from the air diffuses into the blood and carbon dioxide travels from the blood into the alveoli through a thin layer of cells called the alveolar interstitium or blood-air barrier, which mainly contains capillaries and alveolar epithelium (**Fig. 4**). After that, the oxygenated blood leaves the lungs through the pulmonary veins and goes back to the left part of the heart (Conhaim and Staub, 1980; West, 2013).

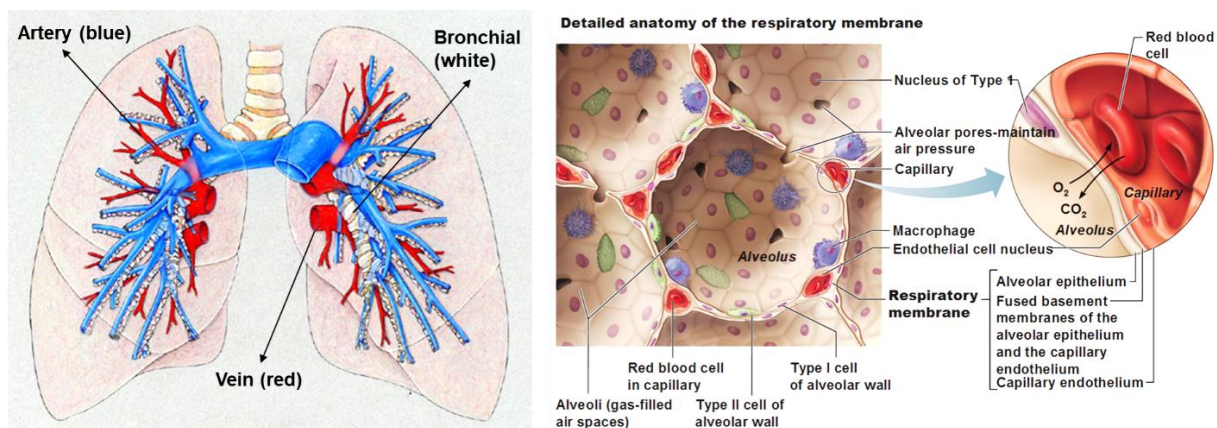


Figure 4. Anatomy of the normal lung and alveoli. (<https://www.med-ed.virginia.edu/courses/rad/cxr/anatomy6chest.html> and <https://antranik.org/wp-content/uploads/2011/12/detailed-anatomy-of-the-respiratory-membrane-type-1-type-2-cells-alveolus-capillary.jpg>; date of download: 01/12/2020)

Nowadays, malignant tumors are the main diseases that endanger human health and life in the world (Siegel et al., 2018). The lung is not only the most prevailing tumorigenic organ but also the most common tumor metastases harboring organ in our body (Herbst et al., 2018). The main reason for that is that cancer has the ability to recur and spread in the normal organs widely, which also makes it difficult to cure (Robinson et al., 2017). It is a common scenario that different types of cancer patients die for their lung metastases after primary tumor resection after a few years. Increasing evidence demonstrates that lung metastases develop from a few cancer stem cells and progress via the interaction with the tumor microenvironment, including the surrounding blood vessels, immune cells, fibroblasts, signaling molecules and the extracellular matrix (Quail and Joyce, 2013). Tumor microenvironment research has

resulted in an important breakthrough in the treatment of tumors, such as related tumor targeting and immunotherapy strategy (Mayekar and Bivona, 2017).

However, conventional 2D imaging systems are often failing in detecting these tiny and unknown-distributed metastases and the microenvironment completely. The reason is that light scattering caused by the different RIs of various components in the tissue, which limits the imaging depth and resolution of common microscopes (Nojima et al., 2017). Therefore, the current structural morphology studies on lung tissue and tumor microenvironment mostly rely on thin slices to generate 2D images, the volume of examined tissue is restricted. In order to achieve 3D structural images of whole mount lung tissue, researchers always have to count on reconstruction of a large number of high quality images from serial sections. However, the workflow and program are labor intensive and time-consuming.

Hence, to detect and quantify sparsely distributed metastases and tumor microenvironment in the whole lung at early stages of tumor metastasis, there is an urgent need for a novel imaging analytical platform, which can reveal the 3D spatial distribution of tumor metastases and microenvironment at signal cellular resolution level directly.

1.6 Aim of our project

Imaging the lung is not trivial as during preparation it may collapse. Also serial sections to get a 3D image may lead to artifacts. Thus the tasks of this thesis was:

- 1) to establish 3D imaging protocols of lung tissue based on two methods: optical tissue clearing and expansion microscopy.
- 2) to apply the ECI-based OTC method, which was modified by our group, to lung research and figure out the best conditions for the application.
- 3) to establish and modify the ExM protocol with perfused normal lung tissue and further extend it to paraffin blocks and metastases.
- 4) to figure out the best way to do 3D imaging in lung research.

2 MATERIAL AND METHOD

2.1 Animals:

Usually 8 weeks old, specific pathogen free (SPF) female C57BL/6 mice (25-38g) were used in our research. Animals were kept in a temperature-controlled SPF facility with a 12:12 h light:dark cycle and ad libitum access to food and water. All experimental procedures and methods were approved by the local authority and conducted in accordance with all guidelines and regulations set by the Germany Animal Protection Law and EC directive 2010/63 EU.

For the perfusion the mice were deeply anesthetized by intraperitoneal injection of ketamine/xylazine (120 mg/kg BW ketamine and 16 mg/kg BW xylazine). Once anesthetized, we used a toe-pinch reflex to determine the complete absence of responsiveness before proceeding to surgery.

2.2 Metastases specimen

The paraffin-embedded normal lung and lung metastases tissue blocks were provided by Prof. Dr. Jonathan P. Sleeman from Microvascular Biology and Pathobiology, Center for Biomedicine and Medical Technology Mannheim (CBTM), Medical Faculty Mannheim of Heidelberg university. The normal lung tissues were from the BALB/c mice. The lung metastases were induced by intravenous injection of Lewis lung cancer cells into BALB/c mice.

2.3 Materials:

2.3.1 ECI based OTC:

- Compressor (Jun-Air compressor, Rio Grande, 117301),
- Syringe pump (Chemyx, Fusion 100 infusion pump),
- tissue processor (Leica microsystems, TP1020),
- Ethyl cinnamate (Sigma-Aldrich, 112372),
- MHI148-PEI dye (designed by Medical Research Center of the Medical Faculty Mannheim, patent code WO/2018/100089),
- Paraformaldehyde (PFA) (Sigma-Aldrich, 158127)

- Black tube (Litesafe, TB5000),
- Tissue culture dishes (Orange Scientific, Cat# 5550200),
- Glue (UHU super, 45565),
- Immersion oil (RI=1.51, Thermo Fisher Scientific, NC0586121),
- Leica SP8 confocal microscope,
- Leica TCS SP8 DLS light-sheet microscope,
- Leica LAS X software.

2.3.2 ExM:

- 40% Acrylamide solution (BIO-RAD, Cat. # 1610140) Acrylamide solution is toxic, therefore, all procedure were performed under a fume hood,
- 2% Bis-acrylamide solution (BIO-RAD, Cat. # 1610142),
- Sodium acrylate (Sigma-Aldrich, Cat. # 408220),
- 16% Paraformaldehyde (Electron Microscopy Sciences, Cat. # 15710-S),
- VA-044 ((2,2'-Azobis[2-(2-imidazolin-2yl)propane]dihydrochloride), FUJIFLM, Cat. # 27776-21-2),
- Vibratome (Leica, VT1200 S),
- Sodium dodecyl sulfates (SDS) (Sigma-Aldrich, Cat. # L3771),
- Tris base (Sigma-Aldrich, Cat. # T6066),
- Agarose (Biozym, Cat. # 850074),
- Petri dish (Ibidi, Cat. # 81136).

2.3.3 Antibodies:

As shown in **Table 1**.

Table 1. Overview of antibodies validated to stain lung tissue with ExM.

Name	Company	Catalog No.	Concentration
Rabbit polyclonal anti-AQP5	Abcam	ab78486	1:100
Goat polyclonal anti CD31/PECAM-1	RD systems	AF3628	1:100
Rabbit polyclonal anti-E-cadherin	Cellsignal	24E10	1:100
Rabbit polyclonal anti-Acetyl-alpha-Tubulin	Sigma-Aldrich	ab5600	1:100
Ly-6G/Ly-6C Monoclonal Antibody	Invitrogen	MA1-10401	1:50
Donkey Anti-Rabbit IgG H&L-Alexa Fluor 647	Abcam	Ab150075	1:100
Donkey Anti-Rabbit IgG H&L-Alexa Fluor 568	Abcam	Ab175470	1:100
Donkey Anti-Goat IgG H&L-Alexa Fluor 568	Abcam	Ab175704	1:100
Donkey anti-Goat IgG (H+L) Cross-Adsorbed Secondary Antibody-Alexa Fluor 647	Thermofisher	A-21447	1:100
Donkey Anti-Rat IgG H&L-Alexa Fluor® 647	Abcam	Ab150155	1:100

2.4 Perfusion procedure and mouse lung extracting

The whole body perfusion was performed by inserting a needle into the bifurcation of the abdominal aorta in mice, which is named as retrograde perfusion protocol (**Fig. 5A**

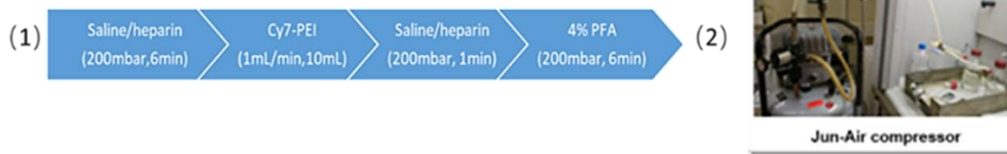
(1)). The perfusion device is made up of a series of tubes connected to a compressor with two bottles filled with saline/heparin (0.9% saline + heparin 5 IU/mL, pH=7.4) and 4% PFA (pH=7.4) (**Fig. 5A (2)**). Apart from that, a syringe pump is connected to the export tube via a T-junction, which can be used for the staining dye. The dye is administered at a constant rate (1ml/min). The whole perfusion process is pressure- and volume-controlled, and is performed automatically. The pressure is fixed at 200 mbar. By this way, all organs of the mice can be cleared from blood and are fixed at the same time. It was essential that there were no air bubbles in the whole system.

The process of perfusion was performed as follows:

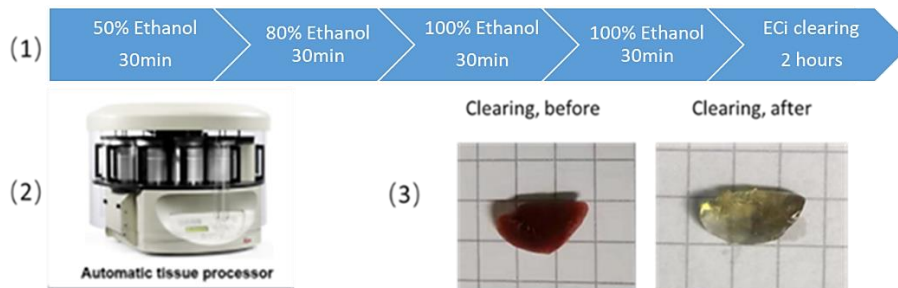
- i. The blunt scissor and surgical area of the abdomen were sterilized by 70% ethanol and the abdominal wall was opened using a scalpel. The omentum and intestine were removed to expose the abdominal aorta.
- ii. A 25G butterfly needle was inserted into the abdominal aorta at the bifurcation and the butterfly was fixed in place with a vascular clamp. The vena cave was opened at the same time.
- iii. The perfusion protocol starts with saline/heparin (200mbar, 6min, ~40 mL) to flush the blood out of the vasculature system of the mouse. This is followed by staining the whole vasculature with MHI148-PEI (1mL/min, 10mL) using the syringe pump.
- iv. Then a short term rinsing with saline/heparin (200mbar, 1min) follows again to remove the residual unbound MHI148-PEI. Finally, the 4% PFA (200mbar, 6min, ~40mL) is used to fix all the organs of the mouse.
- v. After that, all organs are collected and post-fixed in 4% PFA overnight at 4 °C. Then, the organs are washed 3 times (1h for each) with 1 × PBS at room temperature. The samples are stored in 1 × PBS at 4°C up to 2 weeks. During storage the samples are protected from light. For a long-term storage, 1× PBS with 0.05% sodium azide is applied.
- vi. Because of the lung is a real soft organ full of gas, avoiding lung collapse is a critical step to maintain the morphology. We usually extract the lung as follows:
 - 1) The cervical trachea is isolated and ligated with a suture. The trachea is detached from the larynx above the suture knot.
 - 2) The thoracic cavity is opened and extra connective tissues are removed from the lung.

- 3) The lung is taken out by dragging the suture, heart or esophagus with a tweezer. The thoracotomy and lung extraction are performed carefully, avoiding puncturing or squeezing the lung.
- 4) Post-fixation of the lung is done in 4% PFA for a few hour at room temperature or overnight at 4°C. A long time PFA-fixation may quench the fluorescence protein signal and increases the tissue autofluorescence.

A. Retrograde perfusion



B. ECI based OTC



C. Deparaffinization and ExM protocol

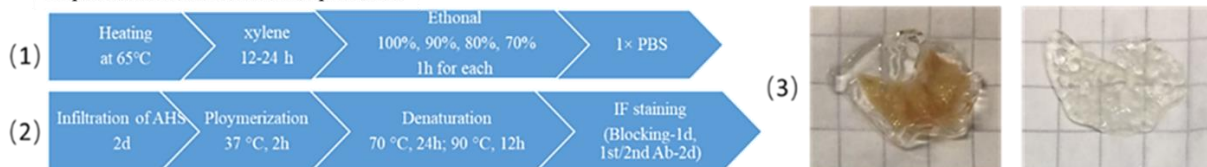


Figure 5. Overview for ECI based OTC and deparaffinized samples with ExM. A: (1). Schematic diagram of the retrograde perfusion protocol for lung; (2). Jun-Air compressor; B: (1). Schematic diagram of the ECI based OTC pipeline; (2). Automatic tissue processor; (3). The perfused and 4% PFA-fixed left mouse lung before and after ECI based OTC protocol. C: (1). Schematic diagram of deparaffinization-rehydration; (2). ExM-immunofluorescence protocol; (3). 500 µm thickness mouse lung slice (after polymerization and removal of the excess hydrogel) before and after ExM protocol.

2.5 ECI based OTC

The ethanol dehydration and ECI clearing were performed in a Leica tissue processor (TP1020) automatically (**Fig. 5B (2)**). Briefly, 4% PFA fixed lung were dehydrated by increasing concentrations of ethanol (50%, 80%, 100%, 100%) and then they were cleared in ECI, as shown in **Fig. 5B (1)**. The immersion time in ethanol for each step lasts 30 min, while the ECI clearing lasts 2 hours. However, according to the volume of different samples, immersion time in ethanol and ECI can vary. The whole procedure was performed at room temperature to improve the penetration rate of all the chemical reagents. After the end of the whole clearing process, specimens were moved into black tubes filled with ECI and stored at room temperature on a rotary.

2.6 ExM and 3D immunofluorescence staining

2.6.1 Infiltration of Amplifying Hydrogel Solution

- i. The Amplifying Hydrogel Solution (AHS) solution is prepared by mixing 40% acrylamide, 2% bis-acrylamide, 16% PFA, sodium acrylate, VA-044 and 10x PBS, then ddH₂O is added to reach the final concentration and volume as shown in **Table 2**. All of the reagents should be kept on ice, and AHS solution can be stored at -20°C until needed (several weeks).
- ii. The 4% PFA perfused and fixed lung is placed in AHS solution and incubated on a horizontal shaker for 2-3 days at 4°C. The AHS solution is protected from light by covering it with foil. According to the size of the sample, the incubation time can vary.

Table 2. Overview of the AHS solution recipe.

Amplifying Hydrogel Solution (AHS)		
Stock solution	Volume (ml)	Final concentration
40% acrylamide	25	20%
2% bis-acrylamide	1.25	0.05%
16% PFA	12.5	4%
Sodium acrylate	5g	10%
10% VA-044 in ddH ₂ O	0.5	0.1%
10x PBS	5	1x
Total volume	50ml (Fill up to final volume with ddH ₂ O)	

2.6.2 Polymerization

The tissue incubated with AHS solution is placed in a 6-well plate covered with freshly prepared AHS solution again. The samples are incubated in a humidified chamber (metal box with wet filter) at 37 °C for 2 hours until the AHS solution turns into a gel. To avoid oxidation, the AHS solution is sealed with parafilm or mineral oil.

2.6.3 Preparation of sections with vibratome

- i. Excessive gel is removed from outside the tissue with a scalpel. The tissue containing gel is cut into 500 μ m sections by the vibratome.
- ii. Then, the slices can be stored in 1 \times PBS at 4 °C until further processed.

2.6.4 Denaturation

- i. The denaturation solution is prepared as shown in **Table 3**, 10% SDS, 5M NaCl, 1M Tris-HCl (PH 9.0), 10 \times PBS and ddH₂O are mixed to reach the final concentration and volume.
- ii. The tissue is placed into 6-well plate and the well is covered with freshly prepared denaturation solution. The plate is wrapped with foil and placed into a humidified chamber (metal box with wet filter). The tissue is incubated for 24 hours at 75 °C, and then for 12 hours at 95 °C.
- iii. After that, the slices are washed with 1 \times PBS for 2 hours (refresh 1 \times PBS every 30min) on a horizontal shaker at room temperature.

Table 3. Overview of the Denaturation solution recipe.

Denaturation solution		
Stock solution	Volume (ml)	Final concentration
10% SDS	25	200mM
5M Nacl	1.25	200mM
1M Tris-HCl	12.5	50mM (PH 9.0)
10 \times PBS	5	1 \times
Total volume	50ml (Fill up to final volume with ddH ₂ O)	

2.6.5 3D Immunofluorescence staining

This part is quite similar to the conventional immunofluorescence staining protocol.

- i. For permeabilization and blocking, samples are transferred into 10 ml of the buffer, which is made up of 1× PBS, 2% BSA and 1% Triton-X-100. It is slowly shaken for 1 day at 37°C. Then, the buffer is carefully removed by aspiration.
- ii. The tissue-containing gel is cut into approximately 1.0×1.0 cm pieces with a sterilized scissor. The gel slides are placed into a 24-well plate.
- iii. 5 µl primary antibodies are diluted in 495 µl blocking buffer to prepare 500 µl primary antibody solutions. Then, the samples are incubated with diluted primary antibody (1:100) buffer at 37°C for 2 days while gently shaking.
- iv. The first antibody stained-samples are washed in blocking buffer three times (1 hour for each time) at 37°C while gently shaking.
- v. For the preparation of the secondary antibody incubation solution, 5 µl secondary antibodies are added into 495 µl blocking buffer. The antibody and samples are protected from light during the whole process. After removing the last washing buffer, samples are covered with secondary antibody solution and incubated at 37°C for 2 days while gently shaking.
- vi. The secondary antibody buffer is removed carefully. Samples are washed with 1× PBS three times (1 hour for each time) at 37°C while gently shaking.
- vii. After that, the samples can be stored in 1× PBS at 4°C until imaging.
- viii. The following antibodies were used for the staining: Anti-Aquaporin5 for the Type I alveolar epithelial cells; anti-CD31 for the vascular endothelial cell, anti-E-cadherin for the bronchial endothelial cell; anti-Acetyl-alpha-Tubulin for the cilia on the bronchial wall, as shown in **Table 1**. Samples were incubated in appropriate secondary antibodies according to the immune specificity and washed in 1× PBS. The crosstalk between different fluorescent dye conjugated secondary antibodies has to be prevented when two or more antibodies were used at the same time. A far-infrared fluorescence conjugated secondary antibody is recommended to avoid the tissue autofluorescence interference during imaging.

2.7 Deparaffinization of tissue from paraffin-embedded blocks

- i. As shown in **Fig. 5C (1)**, tissues were cut out with a blade from the paraffin blocks. The paraffin should be manually removed as much as possible.
- ii. Samples were heated in an incubator at 65 °C until paraffin was macroscopically removed from tissues.
- iii. The tissues were washed with xylene for 12-24 h at room temperature on a rotary. The xylene should be refreshed 1x.
- iv. After deparaffinization, samples were rehydrated with 100%, 90%, 80%, 70% ethanol diluted with ddH₂O for 1 hour respectively.
- v. Then, the samples were washed with 50 ml 1× PBS overnight at room temperature on a rotary. Before being subjected to expansion microscopy and 3D immunostaining as shown in **Fig. 5C (2)**, the lungs were washed with 1× PBS for 1 h again on the next day

2.8 Microscopy and data acquisition

All the samples were imaged on a Leica SP8 laser confocal fluorescence microscope (LCFM) or light sheet fluorescence microscope (LSFM) after OTC or ExM. MHI148-PEI was excited at 638 nm and the emission fluorescence was detected using Cy7 emission filter. Alexa Fluor 647 and Alexa Fluor 568 conjugated secondary antibodies were excited at 638 nm and 552 nm and fluorescence was detected using related emission filters. A 488 nm laser was used to detect the tissue autofluorescence. The way to mount tissue and RI matching are critical steps for 3D imaging.

2.8.1 Sample preparation and RI matching

The samples were imaged as soon as clearing or staining was finished as the samples may lose the fluorescence intensity over time. To this end, the samples were prepared for the microscopy following the next steps:

2.8.1.1 ECI based OTC:

- i. Confocal microscopy: samples were mounted in a Petri dish by a small drop of glue. The samples were immersed in immersion oil (RI = 1.51, nearly the same to the RI of ECI, which is 1.558)). Imaging was performed using a HC PL APO 20x/0.75 IMM CORR CS2 objective.

- ii. Light sheet microscopy: samples were mounted on a parafilm made-base in the central part of a petri dish by a small drop of glue (never too much). The width and height of the sample should be less than 4.0 mm and 5.0 mm. After immobilization, ECi was added carefully as RI matching medium. The objective and sample were immersed in ECi completely. HC PL FLUOTAR 5x/0.15 objective equipped lens with a 7.8 mm working distance dipping cap was applied in our study.

2.8.1.2 ExM:

ExM: The gel slices were transferred to a petri dish carefully, and were immobilized with 1% low melting agarose diluted in ddH₂O to prevent a drift during imaging. The whole slices are almost transparent and the RI matches to water (RI = 1.33), so 1 × PBS solution is used as immersion medium.

2.8.2 3D image acquisition

A brief description of the microscopy setting during 3D imaging will be provided in the next part. The following **Table 4.** illustrates the basic information of the objectives used in our project. All the data were acquired by LAS X software (Leica microsystems, Mannheim, Germany)

Table 4. Different objectives and their features (working distances, immersion media and refractive indexes.

MICROSCOPE	OBJECTIVE	WORKING DISTANCE (mm)	MOUNTING MEDIUM AND REFRACTIVE INDEX
Confocal	HC PL APO 20x/0.7 IMM CORR CS2	0.25	Adjustable to water, glycerol, immersion oil
Confocal	HCX PL APO 63x/1.2 Water CS	0.22	Water, RI: 1.33
Lightsheet	HC PL FLUOTAR 5x/0.15 IMM DLS	7.8	Glycerol, RI: 1.475; ECi, RI:1.558

2.8.2.1 Laser confocal fluorescence microscopy

The laser intensity, smart gain, pinhole and offset value for each fluorescence channel are used to modify the brightness and noise ratio of images. The start and end point of the scanning are determined by turning the Z-position knob to each end of the volume of interest. In order to get a high quality of the image and save scanning time, several parameters are kept constant: the z-step size: 4-5 μm ; format: 1024 \times 1024; speed: 600 Hz; bidirection: on; line average and frame average: 2.

After scanning, the reconstructed 3D images can be further modified by adjusting the options such as shading, opacity, minimum, maximum, gamma and intensity in the 3D viewer of LAS X software

2.8.2.2 Light sheet fluorescence microscopy

Based on the longer working distance of the objective with LSFM, the maximum scanning depth can reach 1.5 mm. The LSFM can acquire images at a speed 100 to 1000 times faster than a point-scanning confocal microscope. At the same time, it always generates the same amount of data. In order to balance the quality of image and amount of the data, several parameters are set: the resolution (in term of binning): 2 \times 2; the z-step size: 4-5 μm , speed: 600 Hz.

2.9 Data storage and quantitative 3D cell morphometry of lung metastases

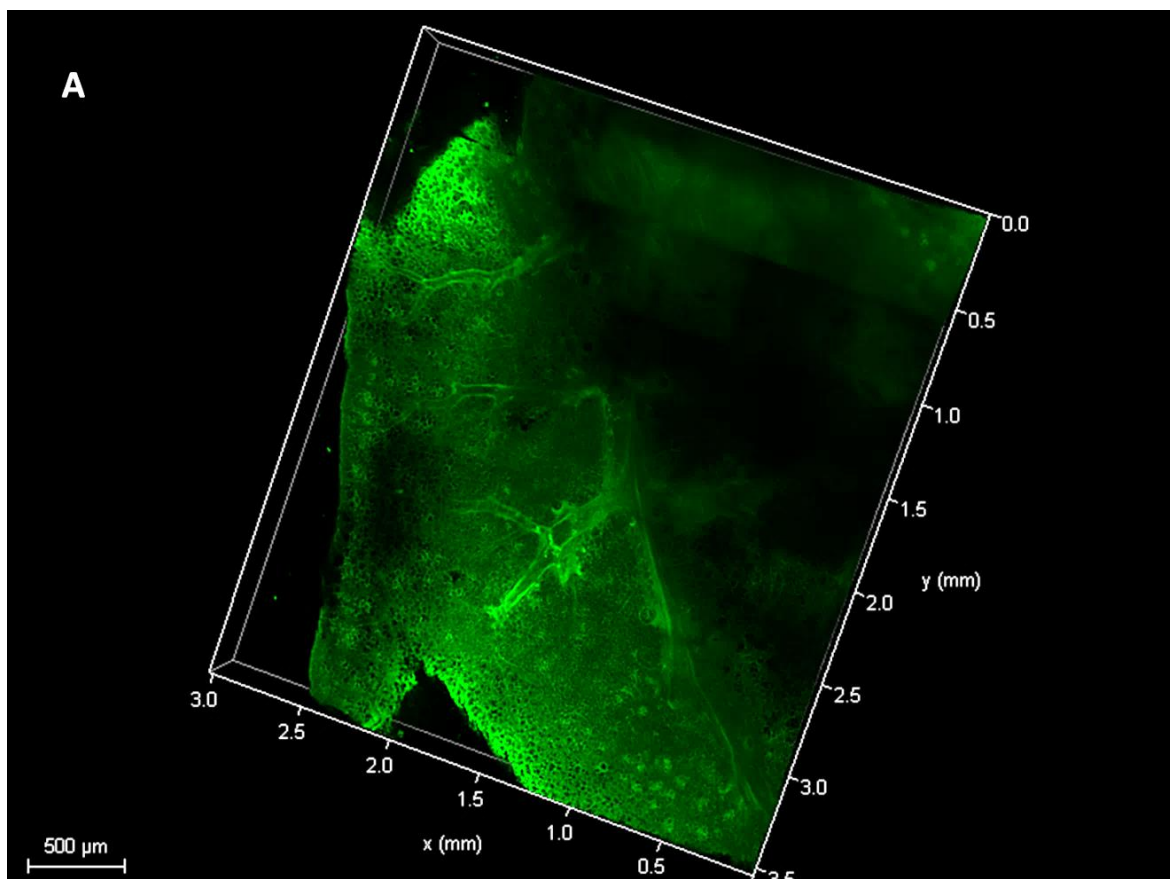
Both of the LCFM and LSFM are directly connected to the computing center of University of Heidelberg via light wires with a transfer rate of 10GB/sec. All the data are stored there in the Scientific Data Storage (SDS) where the data can be accessed in at high speed and in an efficient way.

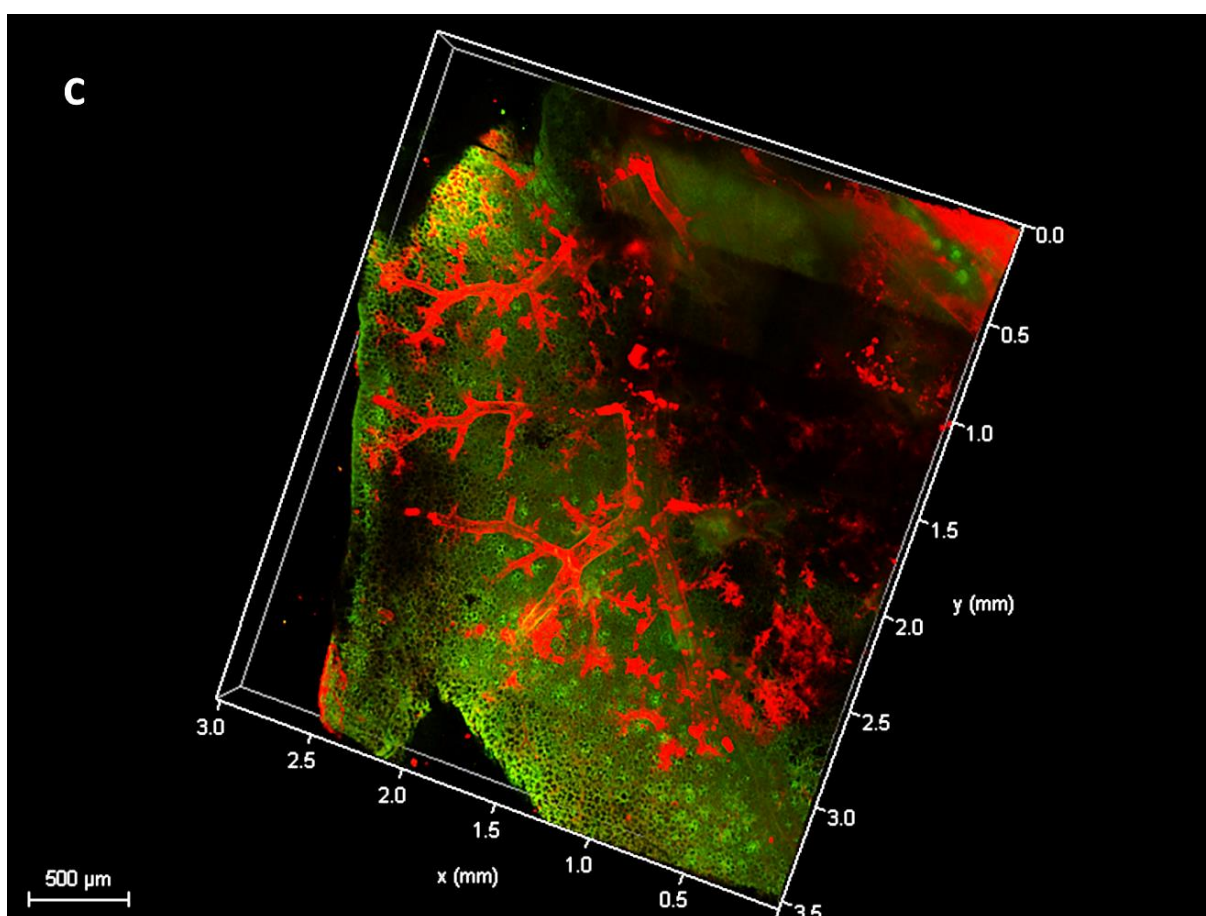
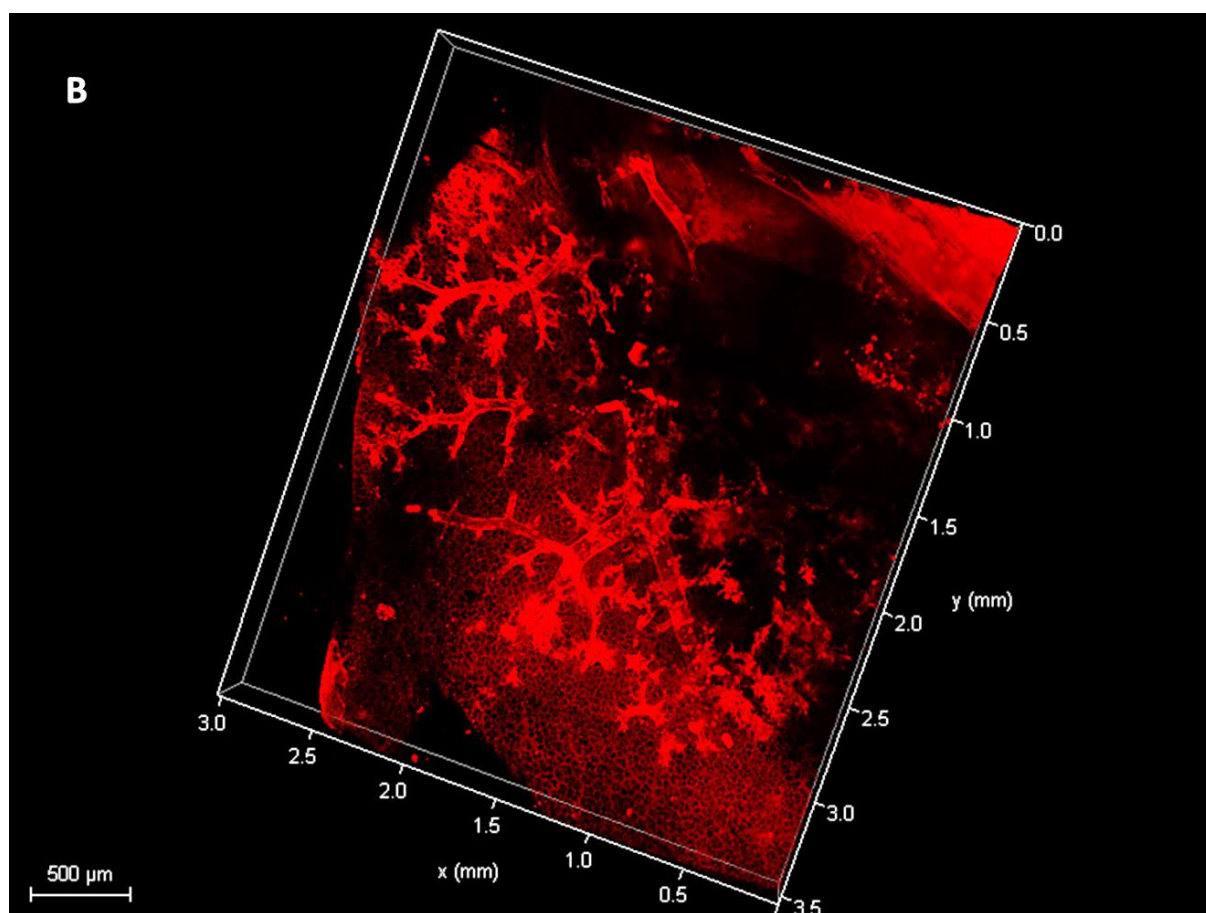
For the quantitative analysis of neutrophil cells distribution in the lung metastases, Fiji and MATLAB software were applied. Maximum intensity projection image after 3-class classification was achieved by Fiji plugin, Tainable Weka Segmentation. X*Y (40 \times 40) was defined as boxes, and the total pixels of neutrophil cells in 3D were calculated for each point by MATLAB. Finally, the histogram of neutrophil cells distribution was smoothed by Gaussian filter with std deviation=2.

3 RESULTS

3.1 3D fluorescence imaging of MHI148-PEI-stained lung vasculature after ECi based OTC

We sought to visualize the vascular network in the lungs after using the ECi clearing technique, an optimized method our group recently reported (Huang et al., 2019). To prove the strength of this advanced 3D imaging technique, we labeled during perfusion the lung vasculature with MHI148-PEI, a cationic dye which was developed by our group (EP 2 944 326 A1). The tissue showed a high degree of optical transparency after ECi based OTC (**Fig. 5B (3)**). As illustrated in **Fig. 6B**, the MHI148-PEI labeled lung vasculature was clearly revealed after ECi based OTC. The fluorescence intensity of the cationic dye was well preserved after the ethanol and ECi clearing process. By autofluorescence imaging, we can also get a rough 3D structure of the alveoli (**Fig. 6A**). **Fig 6C** and **6D** show the overlay and depth coding of these scans giving a better understanding of the vasculature distribution. A section of about 350 μm depth was scanned as indicated by the depth bar with color code. (Experiments were performed five times and repeated with similar results)





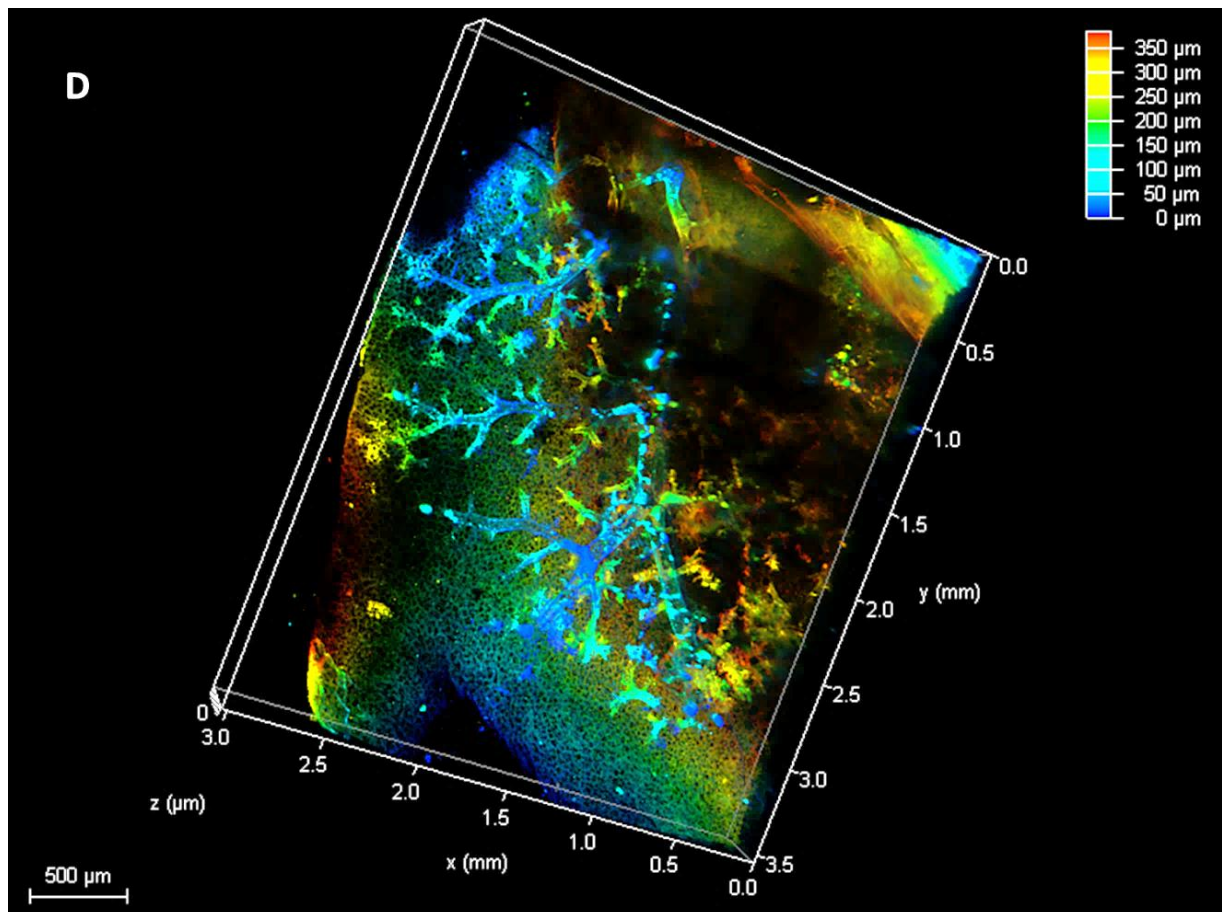
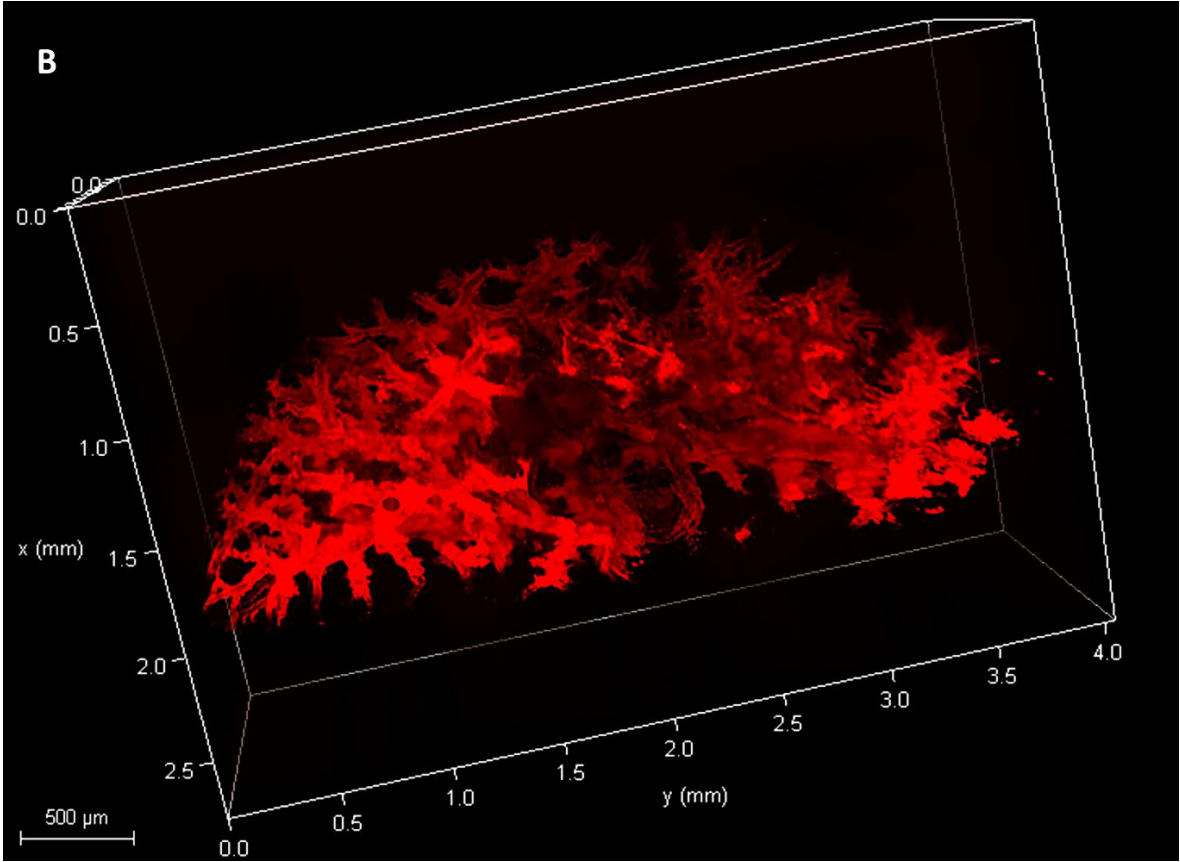
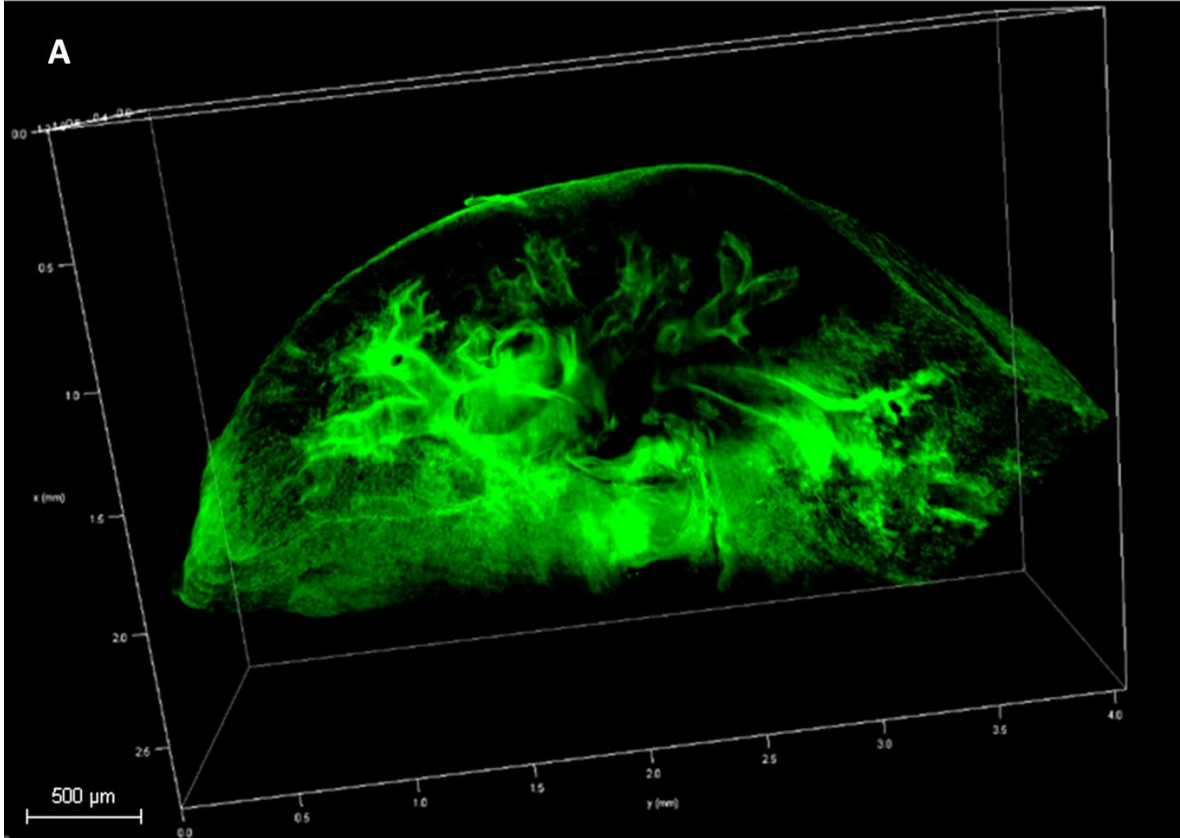


Figure 6. 3D imaging of MHI148-PEI-labeled vasculature in normal lung tissue scanned using the 20x objective of the LCFM. The dye was administered during perfusion via the abdominal aorta, and the lung was collected and processed by ECI based OTC. **A:** 3D visualization of the alveoli by using their autofluorescence (green). **B:** 3D reconstructed image of the vasculature (red) in normal mice lung. **C:** Overlay image of the autofluorescence (green) and vasculature scanning (red). **D:** Depth coding image of the fluorescence labeled lung vasculature. A thickness of about 350 μm was scanned as indicated by the depth bar with color code.

We also imaged the MHI148-PEI-stained and ECI cleared lung by LSFM equipped with 5x objective. Compared with 20x objective of the LCFM, we got a more comprehensive structure of the lung vasculature, but with a lower magnification. **Fig. 7A** shows the profile structure of the lung detected by the autofluorescence scanning, in which the tube-like structure with high green fluorescence intensity in the central part indicates the bronchi. We successfully visualized the vasculature in lung at a depth of > 1.4 mm as shown in **Fig. 7B** and **7D**. **Fig. 7C** gives the overlay of the autofluorescence and dye scanning in which we can find that the vasculature is distributed around the bronchi in 3D vision. (Experiments were performed five times and repeated with similar results)



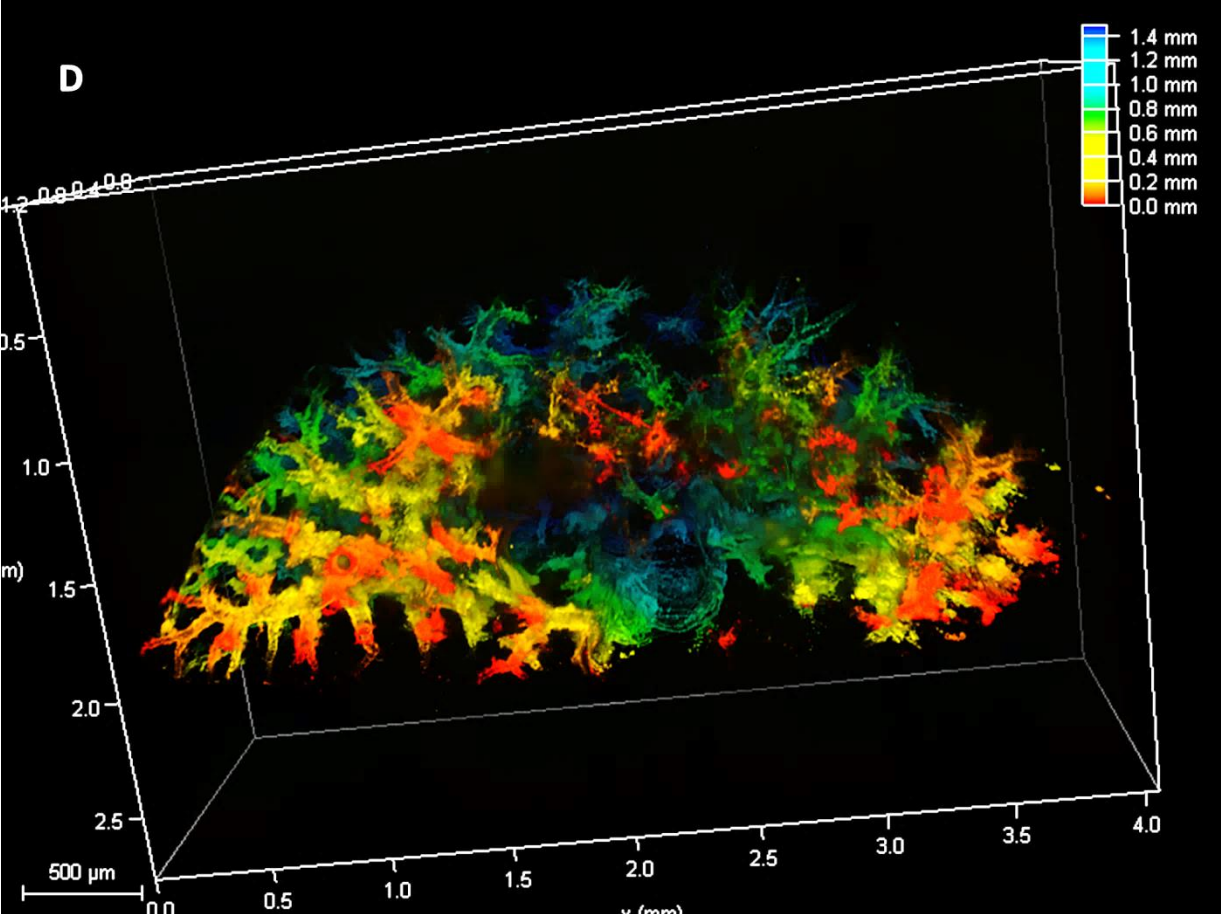
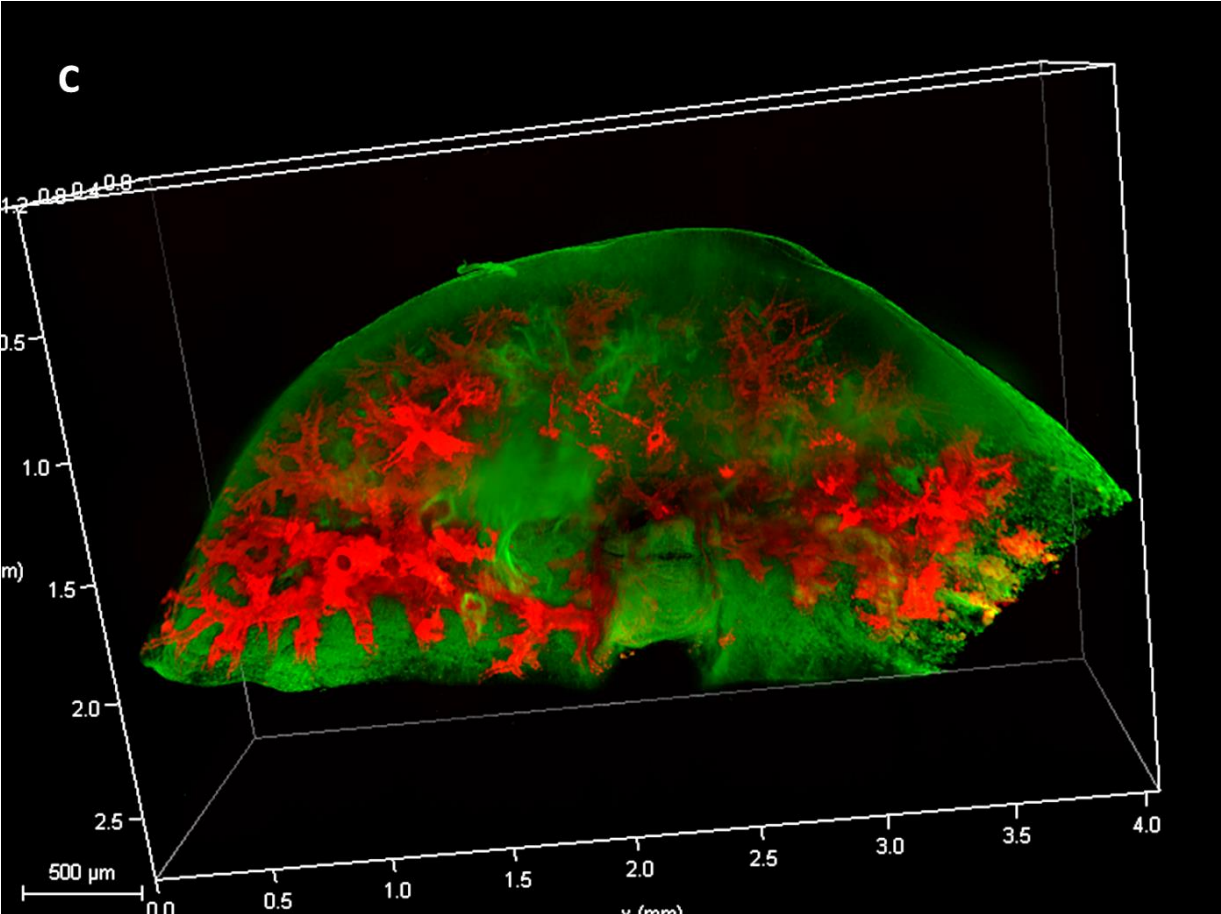


Figure 7. 3D visualization of MHI148-PEI-labeled vasculature in normal lung tissue by LSFM equipped with 5x objective. The dye was administered during the perfusion via the abdominal aorta, and the lung was collected and processed by ECI based OTC. **A:** 3D profile structure of lung tissue (green) detected by autofluorescence scanning. **B:** 3D reconstructed image of the vasculature (red) in normal mice. **C:** Overlay image of the autofluorescence (green) and vasculature scanning (red). **D:** Depth coded image of the fluorescence labeled lung vasculature. We successfully visualized the vasculature in lung at a depth of > 1.4 mm as shown by the depth-coding bar.

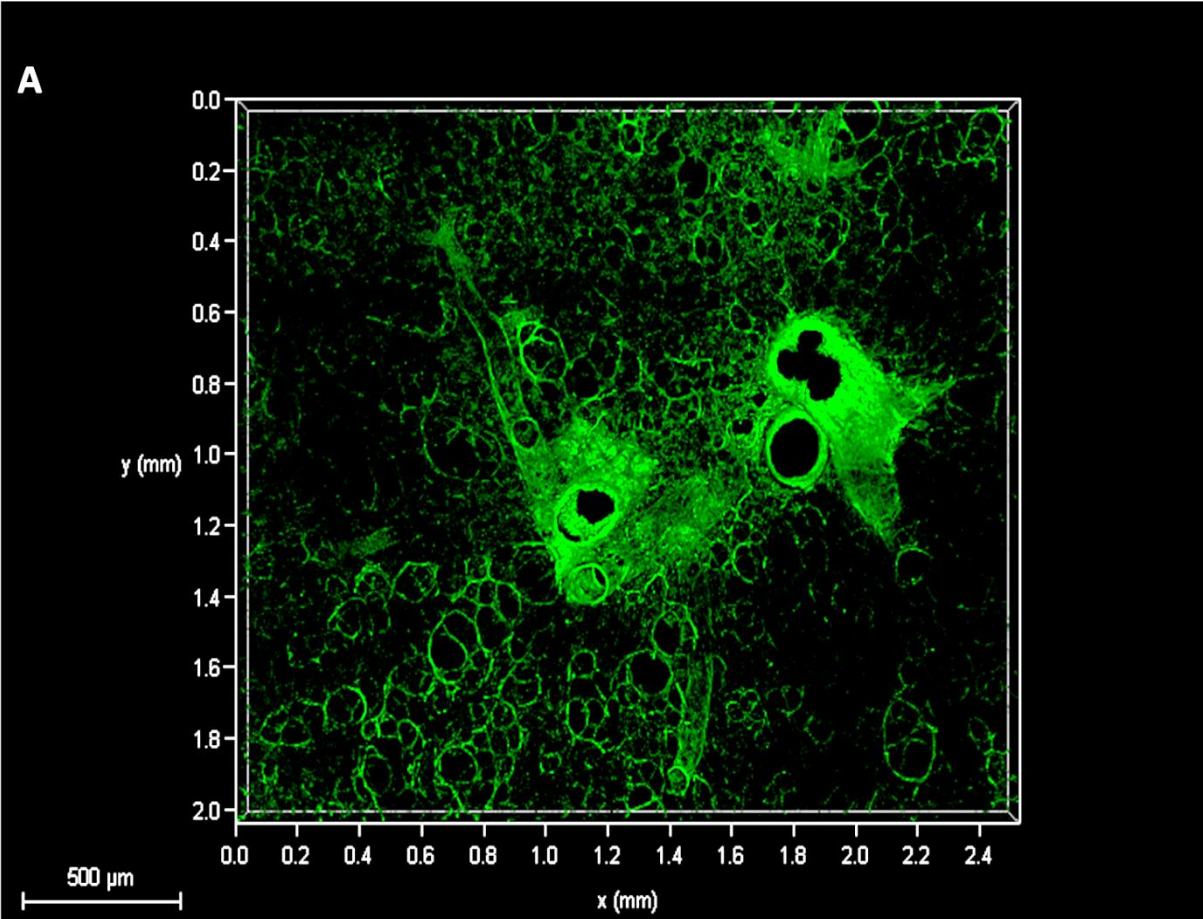
In short, by applying the retrograde perfusion and ECI based OTC procedure, a detailed 3D visualization of the lung vasculature can be performed. In **Fig. 6B** and **7B**, the vessels showed a hollow tubular structure, which was well perfused, stained and fixed. This also demonstrates that the retrograde perfusion, which is much more easier to perform as compared to the commonly used transcatheter perfusion technique, can be widely used in the pulmonary pathology research.

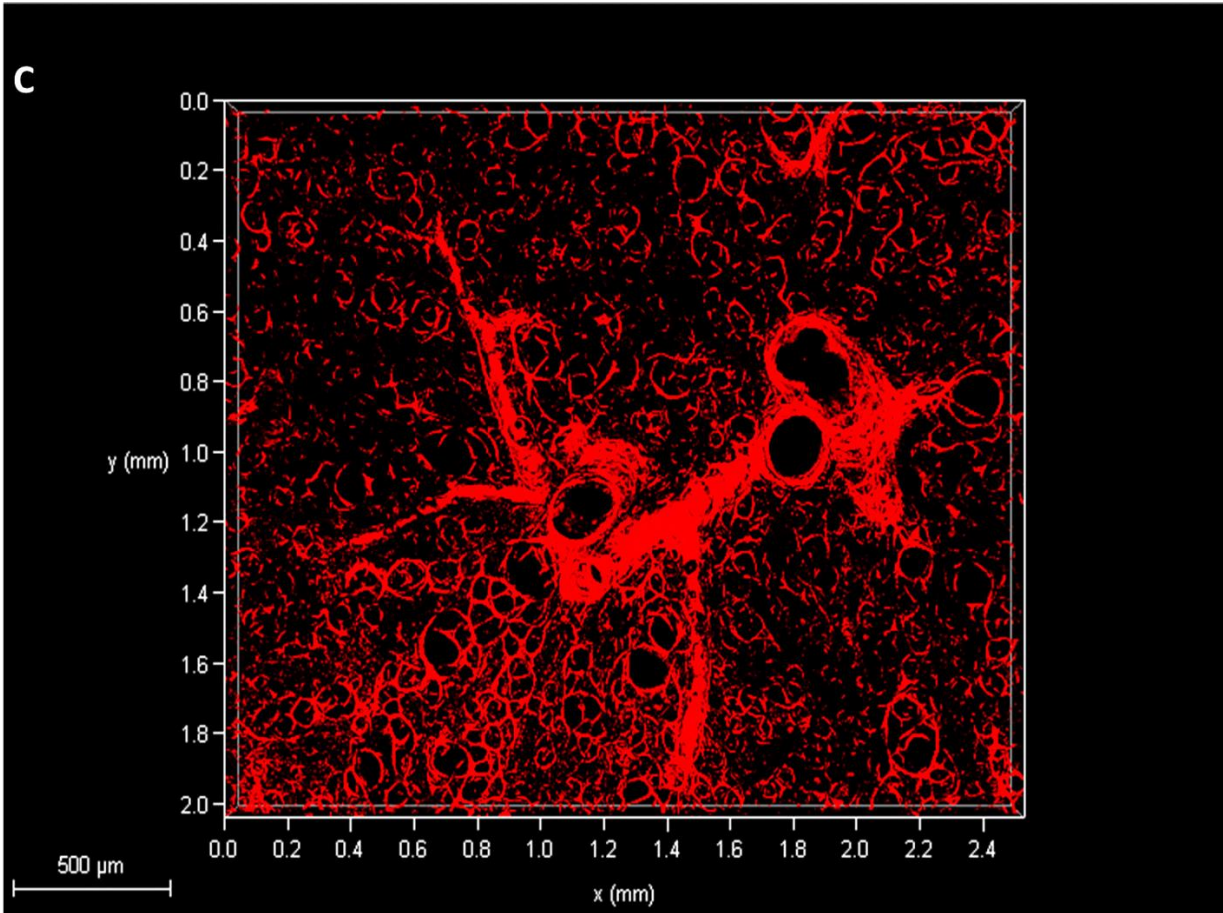
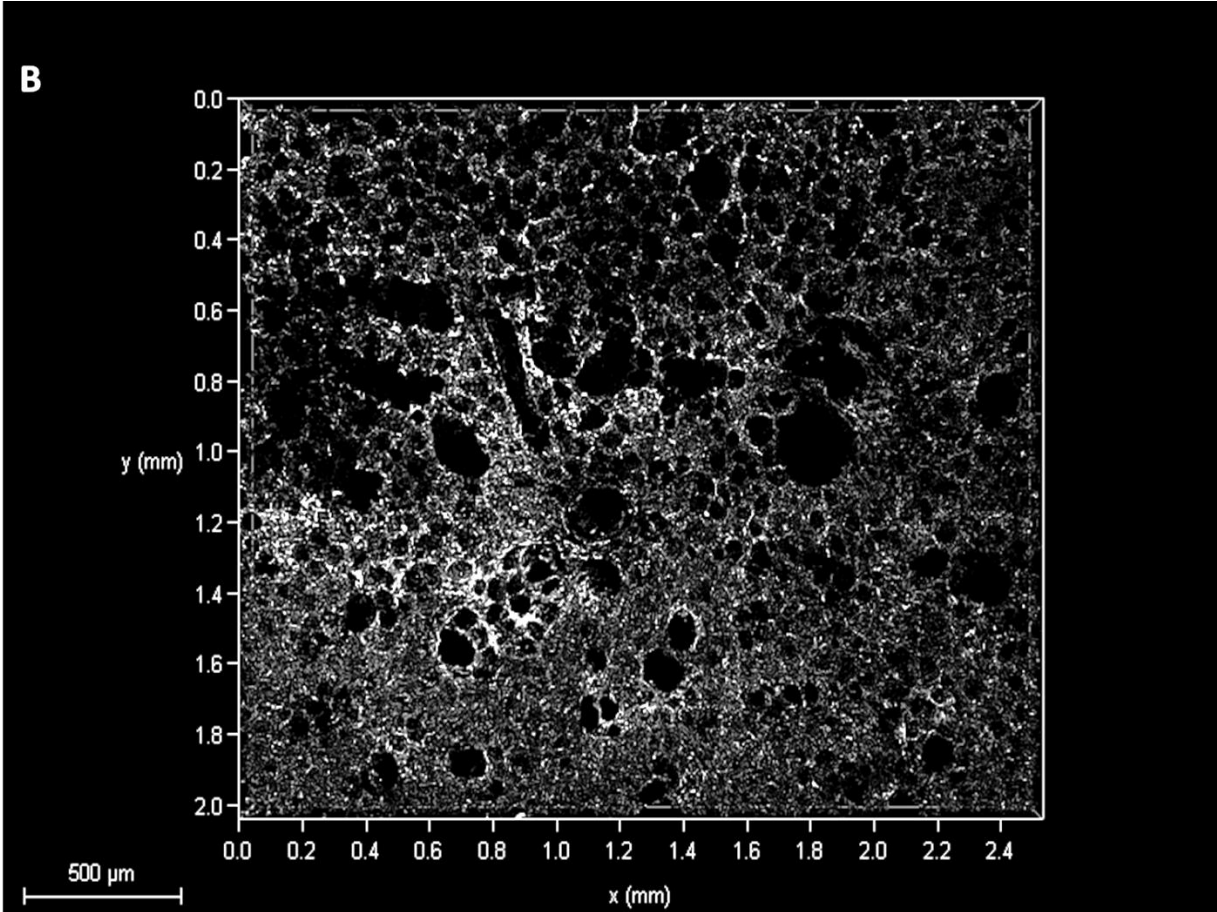
3.2 3D immunofluorescence visualization of the normal lung by ExM

Because of the constitutional heterogeneity of different cells in lung, we tried to reveal the 3D pulmonary structure by ExM and different antibody immunofluorescence stainings. (Experiments were performed five times and repeated with similar results)

Aquaporin5 (AQP5) is a specific membrane marker of the type 1 alveolar epithelial cells and CD31 is a widely used marker of the vascular endothelial cell membrane. We found that the antibodies against AQP5 and CD31, which were widely used in conventional immunohistochemistry, could also be used to reveal the structure of alveoli and vessels in 3D imaging. As we can see in **Fig 5C (3)**, the 500 μm thick mouse lung tissue after polymerization and removal of the excess hydrogel showed a high degree of transparency. In **Fig. 8A**, the autofluorescence (green) indicated the profile of lung tissue which contains alveoli, bronchi and vessels. Obviously, it is impossible to identify them individually by autofluorescence scanning. The 3D structure of alveoli (**Fig. 8B**) and vascular branches (**Fig. 8C**) in lung were revealed by anti-AQP5 and anti-CD31 antibody immunofluorescence staining after ExM. The three channels overlay (**Fig. 8D**) allowed the visualization of the spatial association between bronchi,

alveoli and vessels. By the high magnification 63x water immersion objective, we could get a more clear 3D image of the alveoli made up of type 1 alveolar epithelial cells (green) and the capillaries (red) going through the interstitial tissue between type 1 alveoli epithelial cells, as shown in **Fig. 9**.





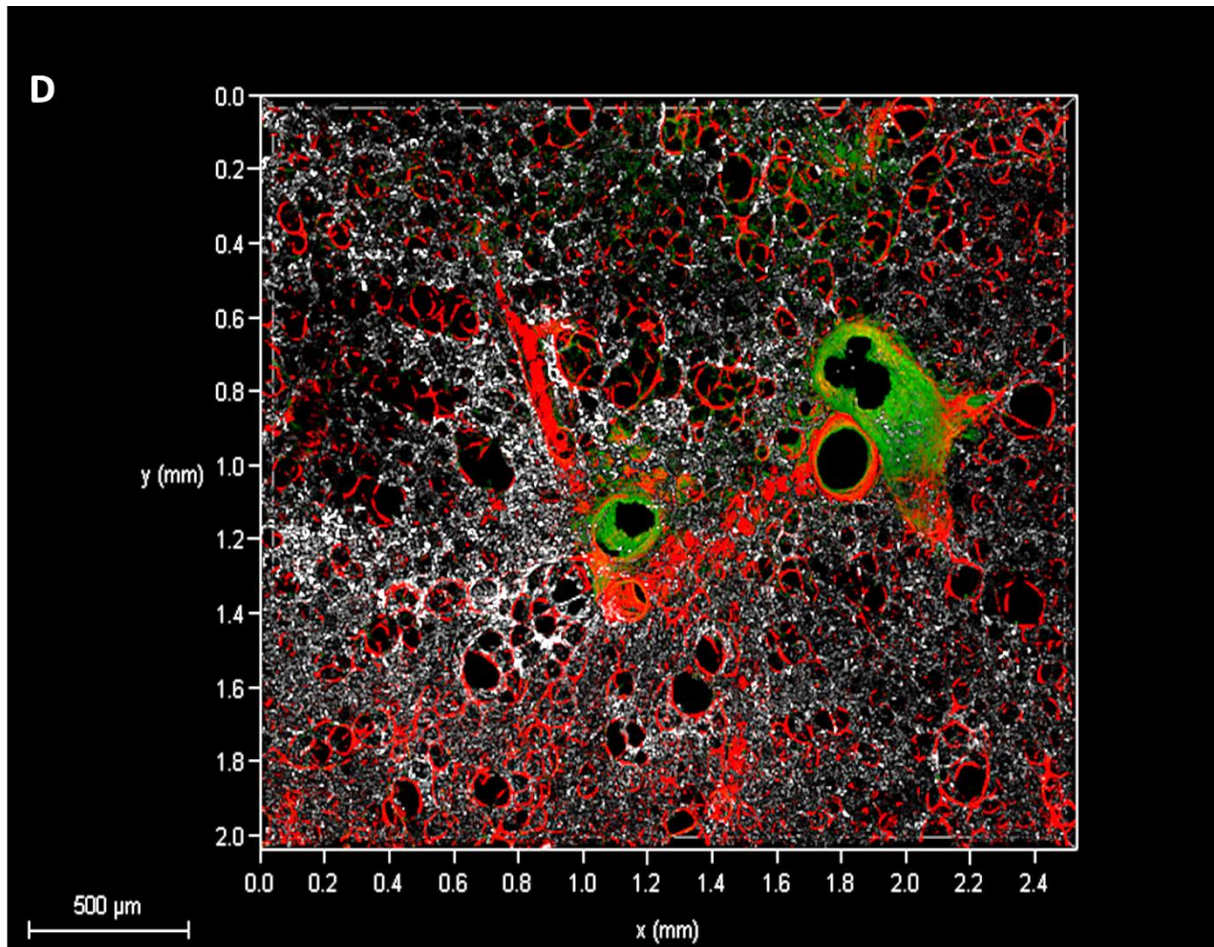


Figure 8. 3D visualization of the anti-AQP5 and anti-CD31 antibody stained lung slice (thickness: 500 μm) after ExM scanned with the 20 \times objective of LCFM. **A:** 3D profile of the normal mouse lung using autofluorescence (green), in which high intensity structures indicate vessels and bronchi. **B:** 3D structure of the alveoli (white) stained with anti-AQP5 antibody in a normal mouse lung. **C:** 3D visualization of the vasculature (red) stained with anti-CD31 antibody. **D:** Overlay image of the autofluorescence, alveoli and vasculature. Green fluorescence was used to identify lung tissue profile by autofluorescence. White fluorescence was used to identify anti-AQP 5 antibody stained type I alveoli epithelial cells. Red fluorescence was used to detect anti-CD31 antibody stained vascular endothelial cells. Scale bar, 500 μm .

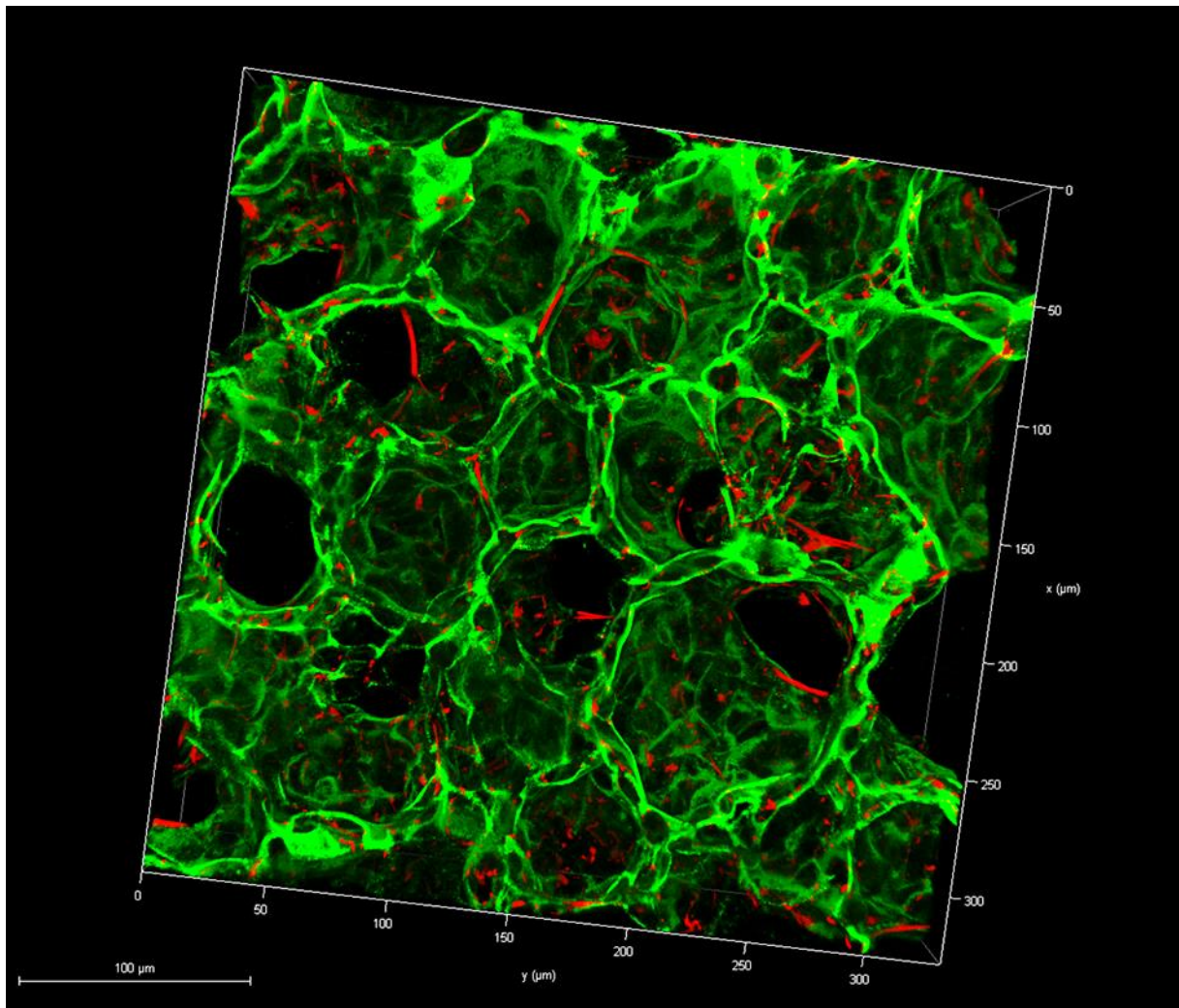


Figure 9. Reconstructed 3D image of alveoli in normal lung slice (thickness: 500 μm) after ExM and immunofluorescence staining. With the 63x water immersion objective of LCFM, we detect the capillaries (red) and the alveolar interstitium (green). Green fluorescence was used to identify anti-AQP5 antibody stained alveolar epithelial cells. Red fluorescence was used to detect anti-CD31 antibody stained vascular cells. Scale bar, 100 μm .

To further evaluate our ExM and immunofluorescence staining protocol, more antibodies were used to image the 3D bronchial structure. Since tissue autofluorescence is strong in the blue-green spectrum, fluorophores in far-red spectrum are helpful to reduce background. In the following experiment, we used Alexa Fluor-647 for both antibody stainings. The acetylation of α -tubulin on lysine 40 (K 40) is one of the earliest tubulin post-translational modifications discovered to regulate microtubule inner proteins and intracellular transport. α -Tubulin is de-acetylated by histone deacetylase family member 6 (HDAC6) and is acetylated by α -tubulin acetyl transferase.

In lung tissue, acetylated α -tubulin (α -Ac-Tub) has been verified as a marker of ciliated cells on the bronchial epithelium which exhibits an ability to clear mucus from the airway. As shown in **Fig. 10**, anti- α -Ac-Tub stained bronchial cilia (red) were mostly located on the bronchi and uniformly distributed throughout the surface of the normal bronchial epithelium. Autofluorescence (green) was used to show the profile structure of the lung tissue.

E-cadherin is a commonly expressed marker on epithelial cell membranes, but especially higher expressed on bronchial epithelial cells as compared with alveolar epithelial cells. With anti-E-cadherin antibody staining, 3D imaging after ExM revealed the branches of the bronchi (red) in **Fig. 11**. Around the bronchi, there are also some high intensity signal tubular like-structure (green) detected by autofluorescence scanning, which indicate lung vessels. Consistently, the 3D imaging strongly proves that the E-cadherin is more expressed on bronchial epithelium than on the alveolar epithelial cells.

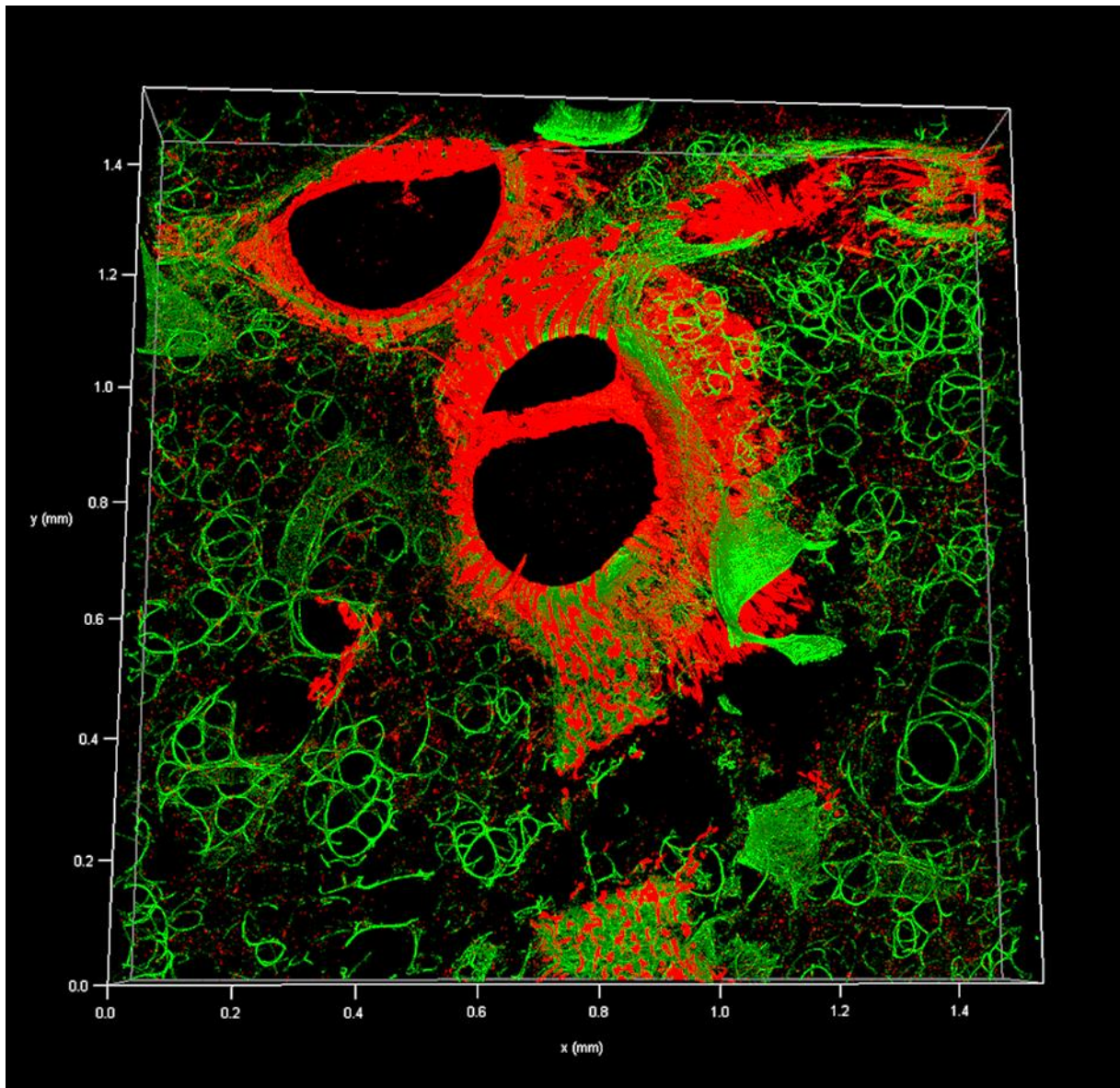
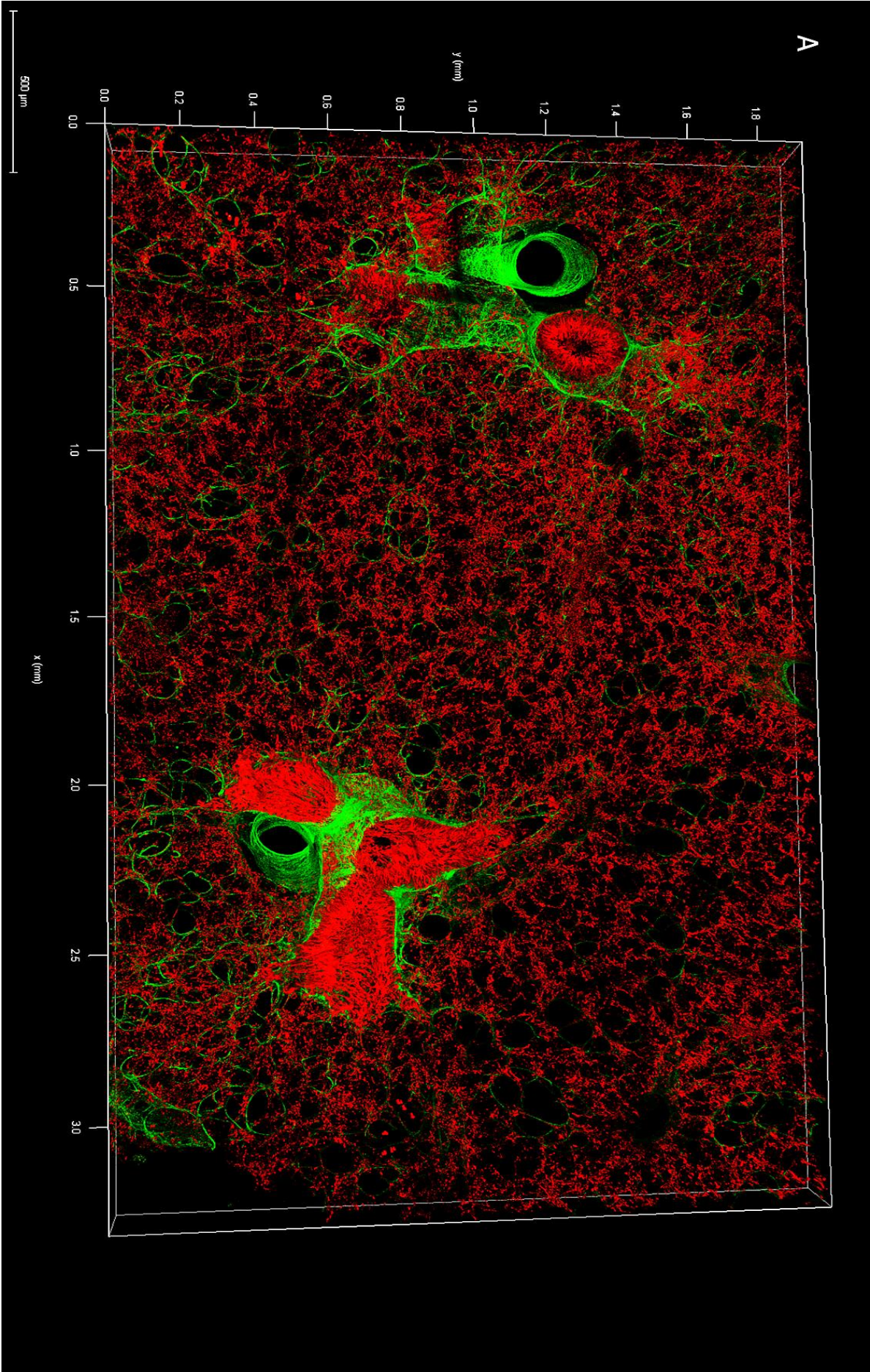


Figure 10. 3D visualization of bronchial cilia (red) stained with anti-acetyl-tubulin antibody in a 500 μm thick lung slice using the 20 \times objective of LCFM. Green fluorescence was used to identify profile structure of lung tissue by autofluorescence. Red fluorescence was used to identify anti-acetyl-tubulin antibody stained bronchial cilia.



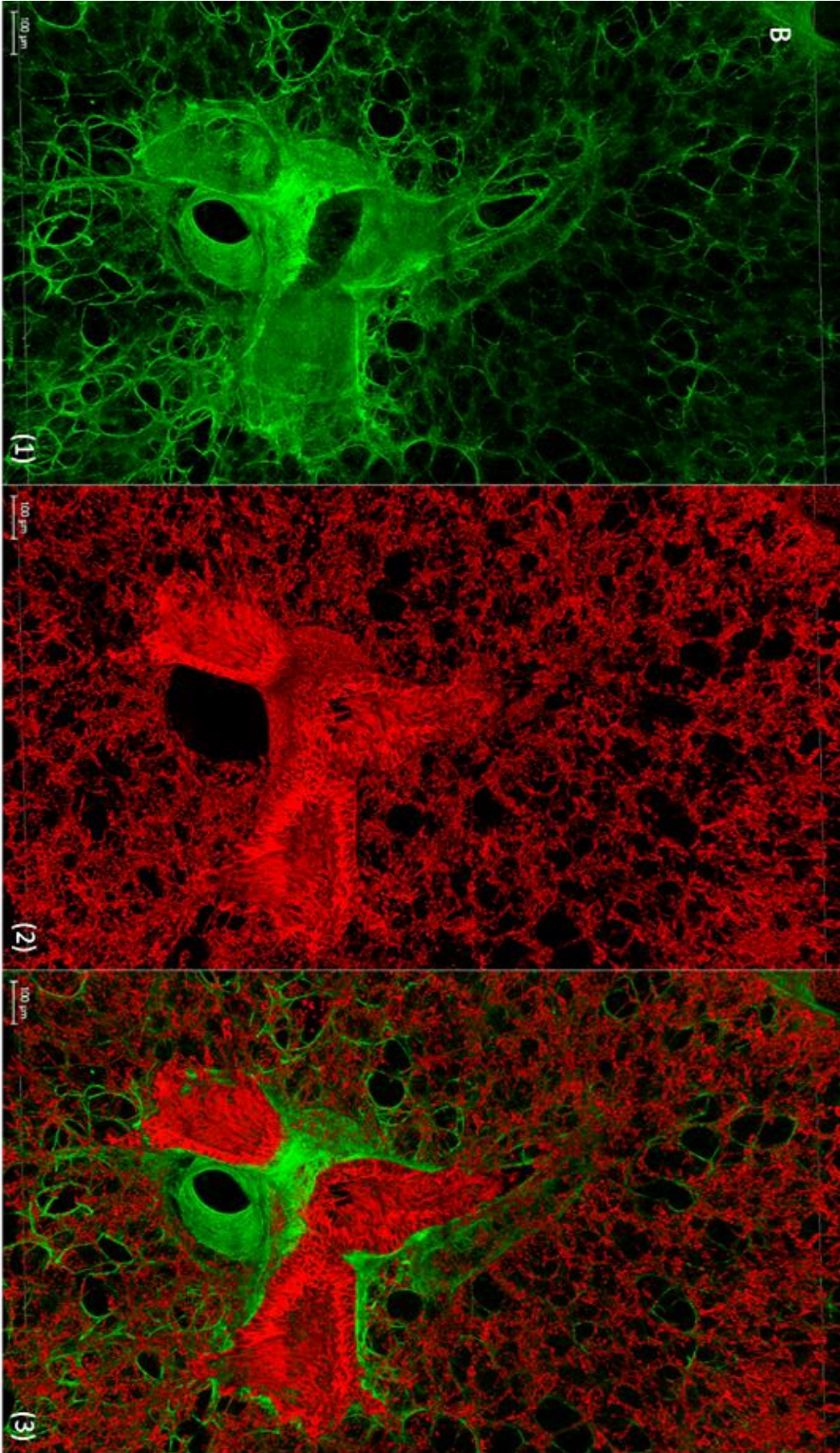


Figure 11. 3D visualization of anti-E-cadherin antibody stained epithelial cells on a 500 μm thick lung slice imaged by 20 \times objective of LCFM. **A:** 3D reconstructed image of the epithelial cells (red, mostly bronchial epithelial cell) stained with anti- E-cadherin antibody. Green fluorescence was used to identify lung tissue profile structure by autofluorescence. **B:** Higher magnification of the bronchial structure than in A with different channels ((1) green-autofluorescence, (2) red-anti-E-cadherin antibody, and (3) overlay image) showed a clearer 3D structure of the bronchial cilia.

3.3 3D imaging of the vasculature in paraffin-embedded lung blocks

In order to further extend the applicability of the established 3D imaging method, we next investigated whether this protocol can be performed on lung tissue embedded in paraffin blocks. 20 years old paraffin-embedded normal lung tissue blocks were recovered by deparaffinization and rehydration, then subjected to ExM and stained. (Experiments were performed five times and repeated with similar results)

The anti-CD31 antibody is widely used for vasculature staining in routine pathological diagnosis, and it works fine with ExM protocol. 3D imaging of an anti-CD31 antibody stained lung after denaturation revealed the big vessels (red) full of erythrocytes, which showed high autofluorescence intensity (green) (**Fig. 12A**). **Fig. 12B** shows the depth coding of anti-CD31 antibody stained big vessels and capillaries in the lung. A scan depth of 250 μm was used as indicated by the depth-coding bar with color.

As shown in **Fig. 13A**, big vessels and vascular junction were revealed in another paraffin embedded-lung after ExM and anti-CD31 immunofluorescence staining. A section depth of 330 μm was scanned (**Fig. 13B**). All these results demonstrate that our 3D imaging pipeline of ExM definitely can be applied for the pathological research on paraffin embedded lung.

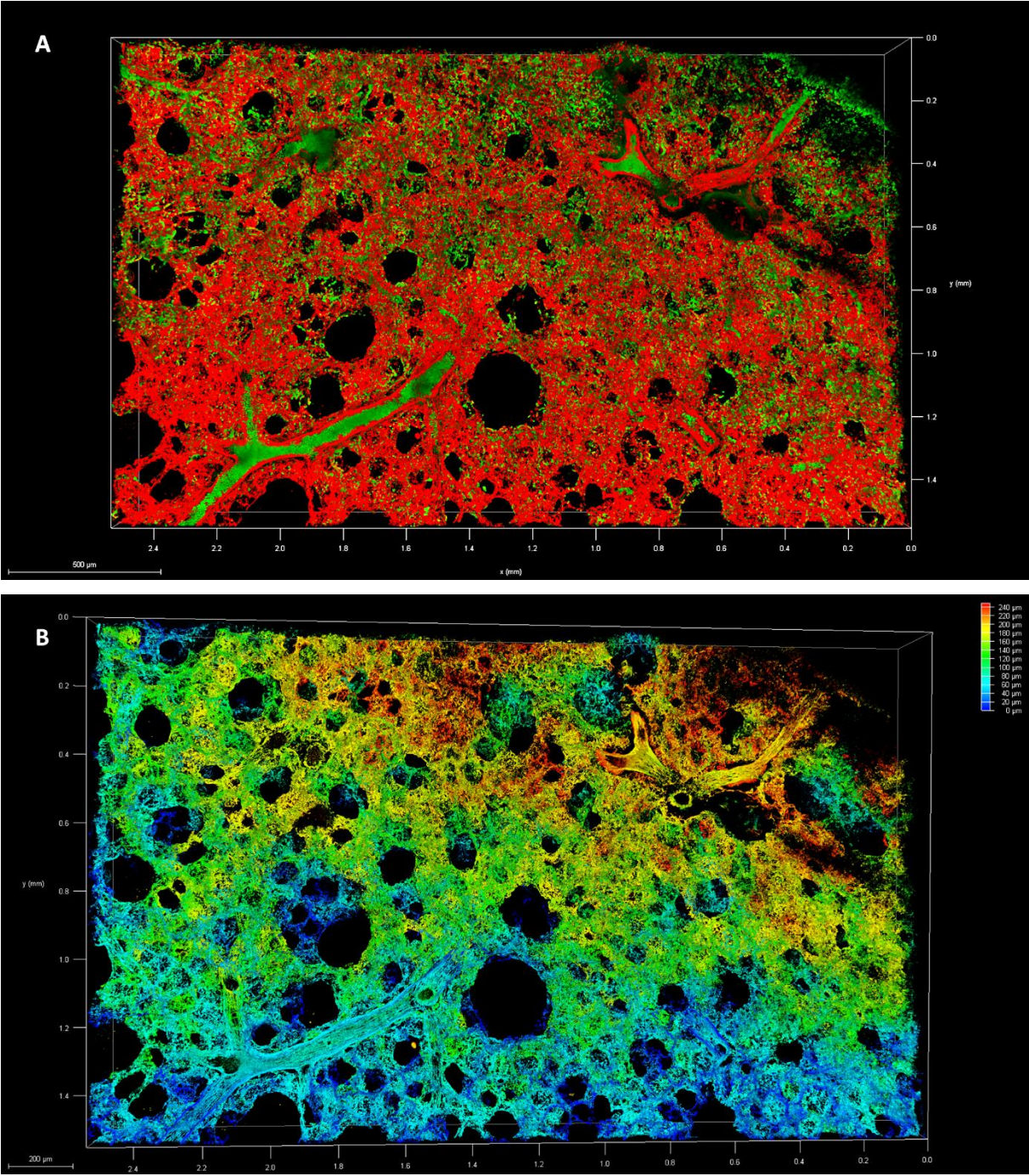


Figure 12. 3D imaging of vasculature on paraffin-embedded normal lung tissue. **A:** 3D reconstructed image of anti-CD31 antibody stained vessels (red) after ExM using LCFM (20x objective). Green fluorescence was used to identify lung tissue profile by autofluorescence. The high green fluorescence intensity in the vessels is due to erythrocytes. **B:** Depth coding image of the antibody stained vasculature and branches. A section of about 250 μm was scanned as shown in the depth-coding bar. Scale bar, 200 μm.

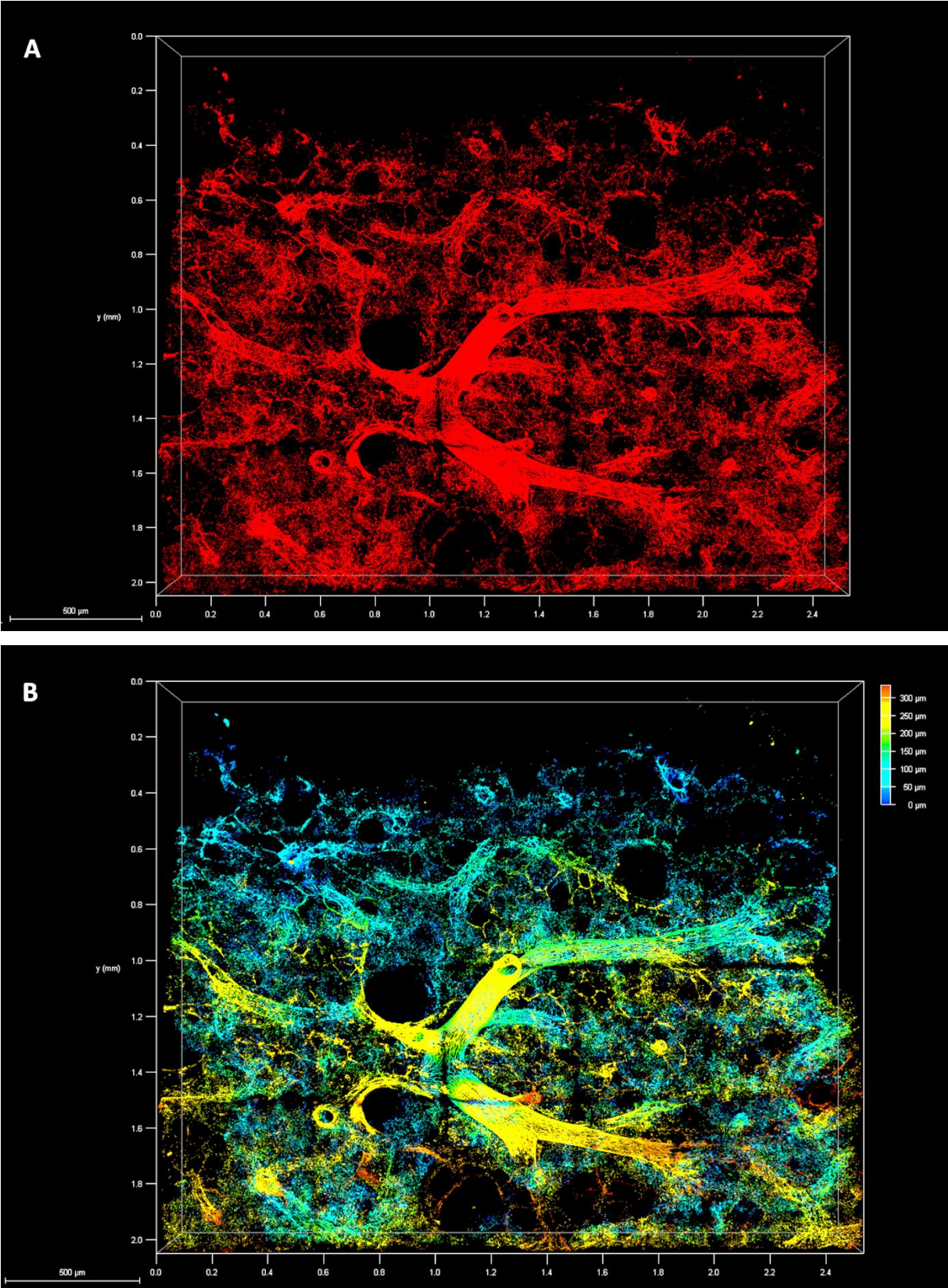


Figure 13. 3D visualization of the vasculature of paraffin-embedded normal lung tissue after ExM using LCFM (20× objective). **A:** 3D reconstructed image of anti-CD31 antibody stained vessels (red). **B:** Depth coding image of the antibody stained vasculature and branches in a lung. A depth of about 330 μm was scanned as indicated by depth-coding bar. Scale bar, 500 μm.

3.4 3D imaging of the microvasculature 10 year old in paraffin-embedded lung metastases

Toward evaluating ExM as a tool of 3D imaging analysis in cancer research, the potential of our ExM pipeline to investigate the vasculature in lung metastases was examined. The paraffin-embedded lung from a lung metastasis model induced by Lewis lung cancer cell line intravenous injection in mice was de-paraffinized and rehydrated. ExM and anti-CD31 antibody immunofluorescence staining was performed to identify the vasculature in these 10 years old lung metastases. (Experiments were performed five times and repeated with similar results)

3D reconstruction of the intense tumor capillary bed (red) could be achieved and provided a precise and integral map of the microvascular network (**Fig. 14A**). It is interesting to find that the metastasis nodule was revealed automatically with a clear circular boundary after ExM. **Fig. 14B** is the high magnification image of the highlighted area (white box) in Fig. 14A to show in detail the complex structure of the vasculature in lung metastases. As shown in **Fig. 14C**, the dark area in the central part of the tissue indicates that the sample is out-of-focus plane; however, the normal lung around the tumor nodule can be imaged in focus at this point. It means that the surface of metastases and normal lung tissue around are not in the same plane after ExM. As a result, the metastases showed up automatically under confocal microscopy.

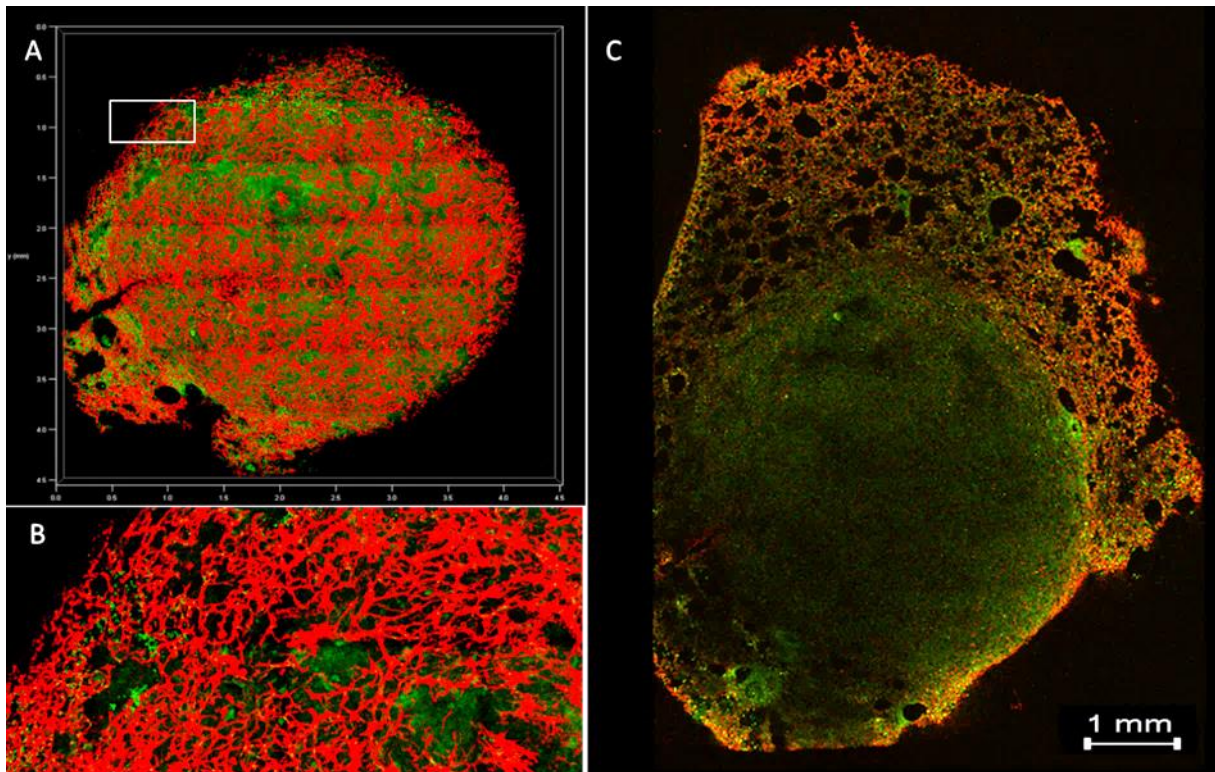
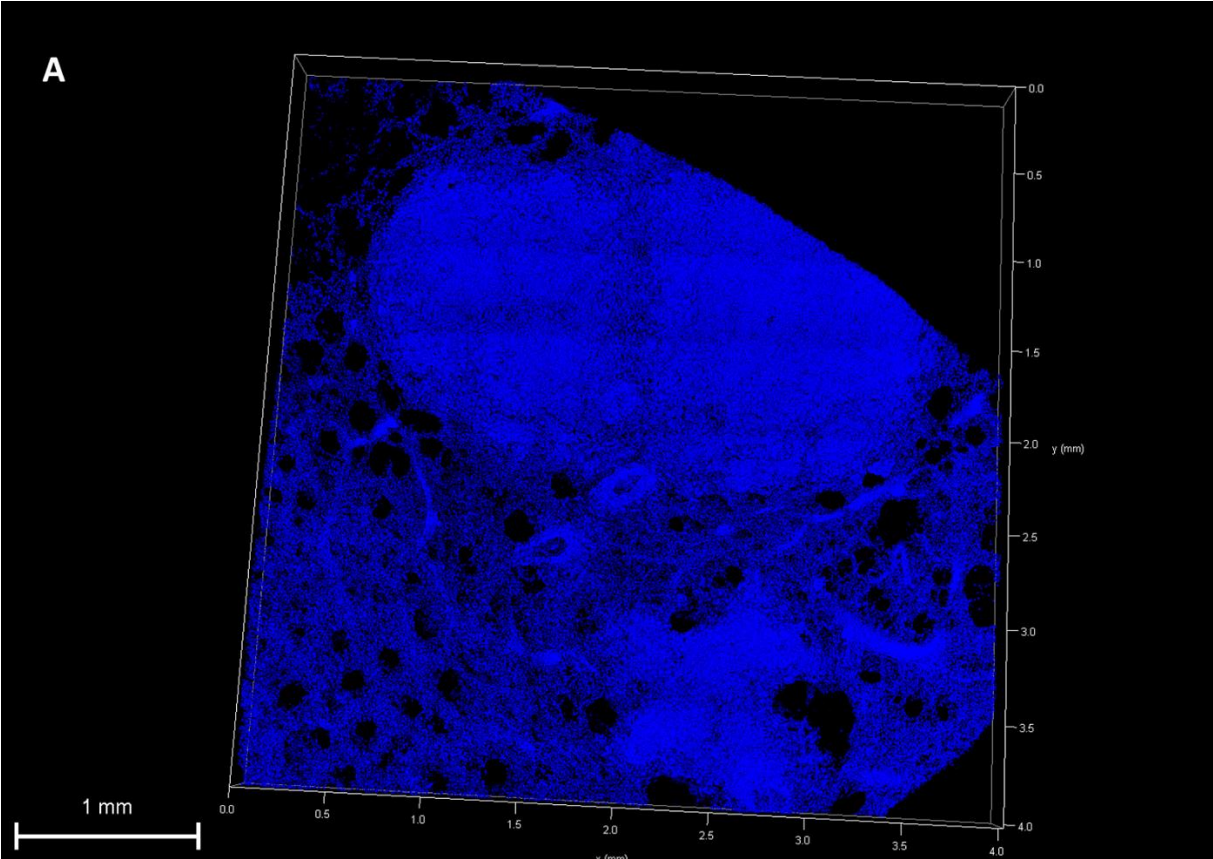
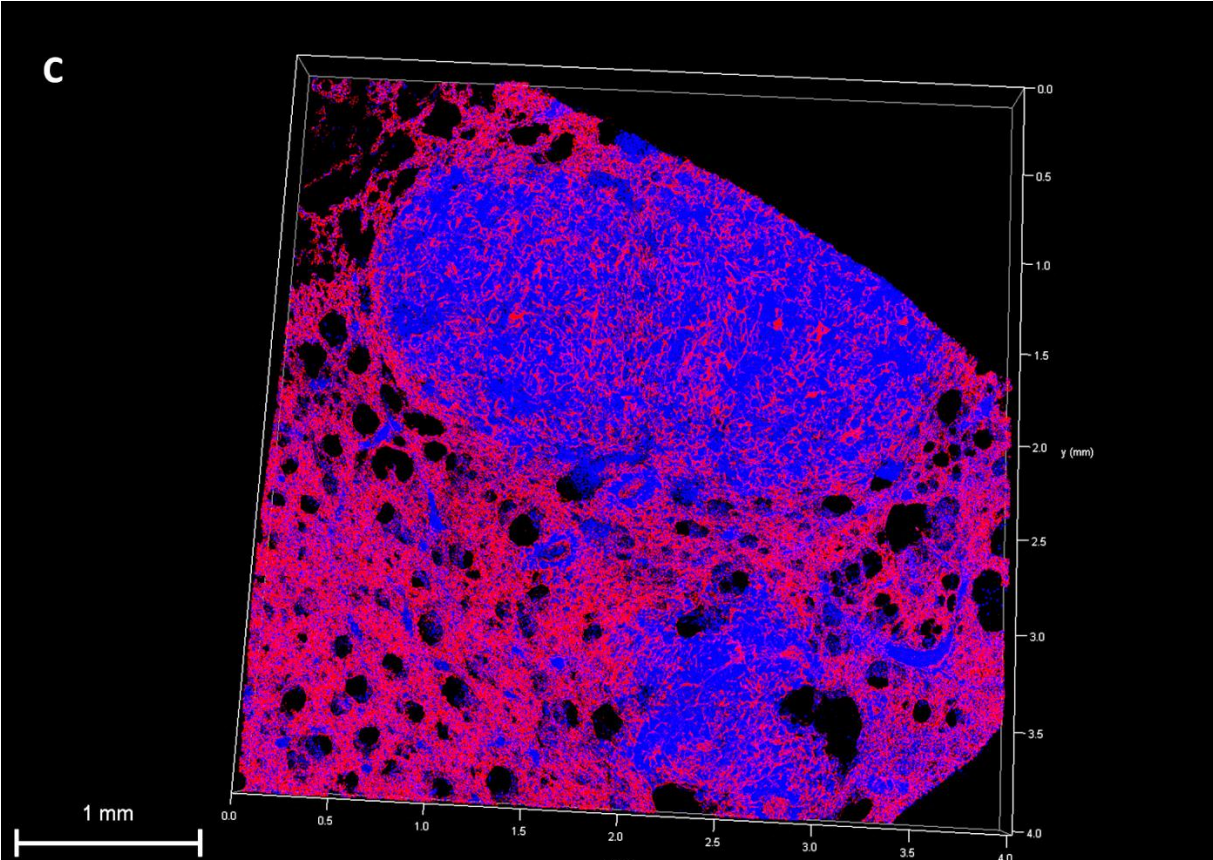
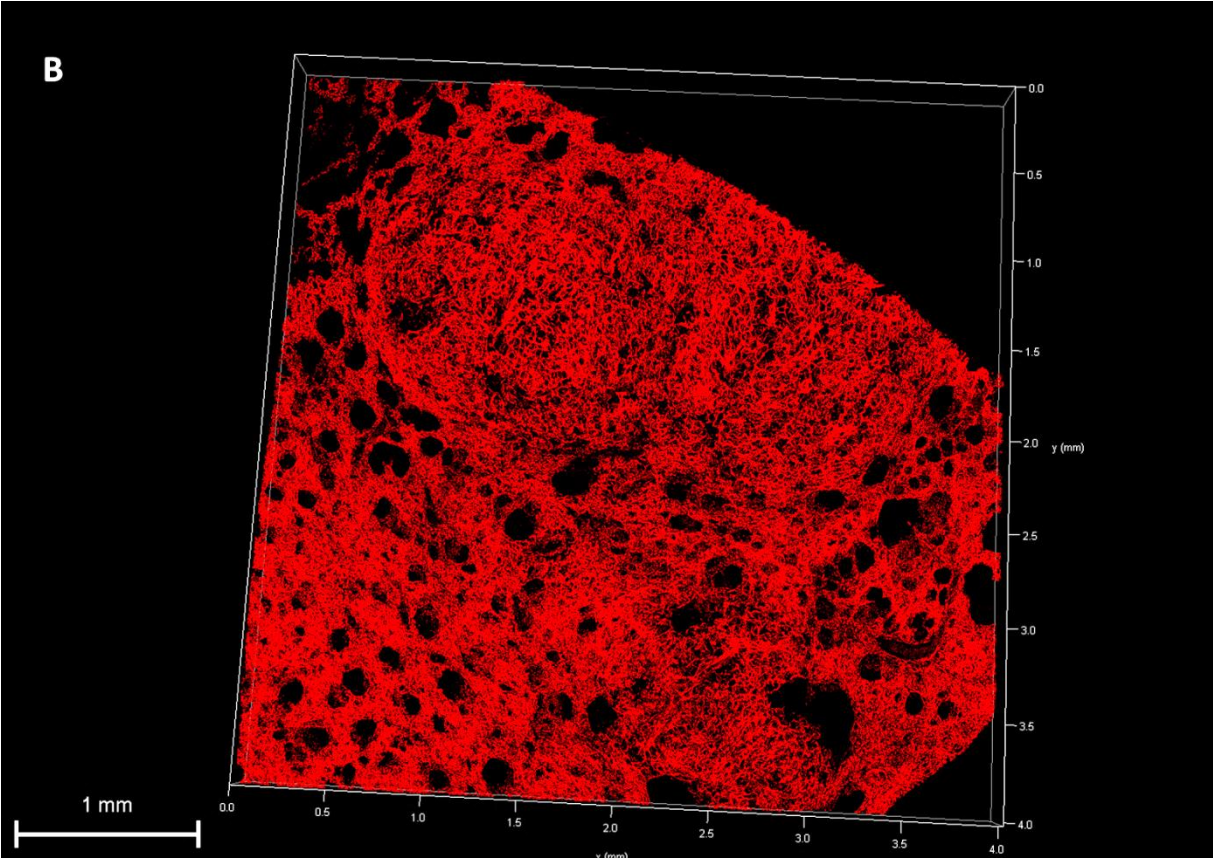


Figure 14. 3D image of the anti-CD31 antibody stained microvasculature in paraffin-embedded lung metastases tissue acquired by LCFM (20 \times objective) after ExM. **A:** 3D image of the complex capillary network (red) could be demonstrated. It is interesting to find that the metastasis nodule was revealed automatically with a clear circular boundary after ExM. **B:** High magnification image of the rectangle indicated area in A shows in detail the complex vascular network in lung metastases. **C:** The dark area in the central part of the tissue shows the profile of lung metastasis nodule which indicates that the sample is out-of-focus. The reason why they were imaged in different focus planes by confocal microscope may be that the lung metastases and normal lung tissue around were expanded differently since they are made up of different kinds of cells and matrix. Green fluorescence was used to identify lung tissue profile.

In order to further investigate the metastases nodule distribution in relationship with the vascular network, we then combined anti-CD31 antibody immunofluorescence staining with nuclear counterstaining with Sytox green. In addition, the tile scan tool of confocal microscopy allowed us to image a larger area of the lung tissue. In **Fig. 15A**, reconstructed 3D image distinguished the lung metastasis nodules, which showed high intensity and accumulation of Sytox green signal (blue), from the normal lung tissue. **Fig. 15B** demonstrated that the vasculature structure (red) in the metastasis nodules were definitely different from the normal lung tissue. This difference may also be helpful

to distinct the tumor metastases from normal lung tissue. The Sytox green and anti-CD31 antibody immunofluorescence staining are overlaid in **Fig. 15C** and depth coding of the vessels (**Fig. 15D**) gave us a better understanding of the metastases and vasculature distribution in the lung metastasis tissue. The scan had a depth of 310 μm .





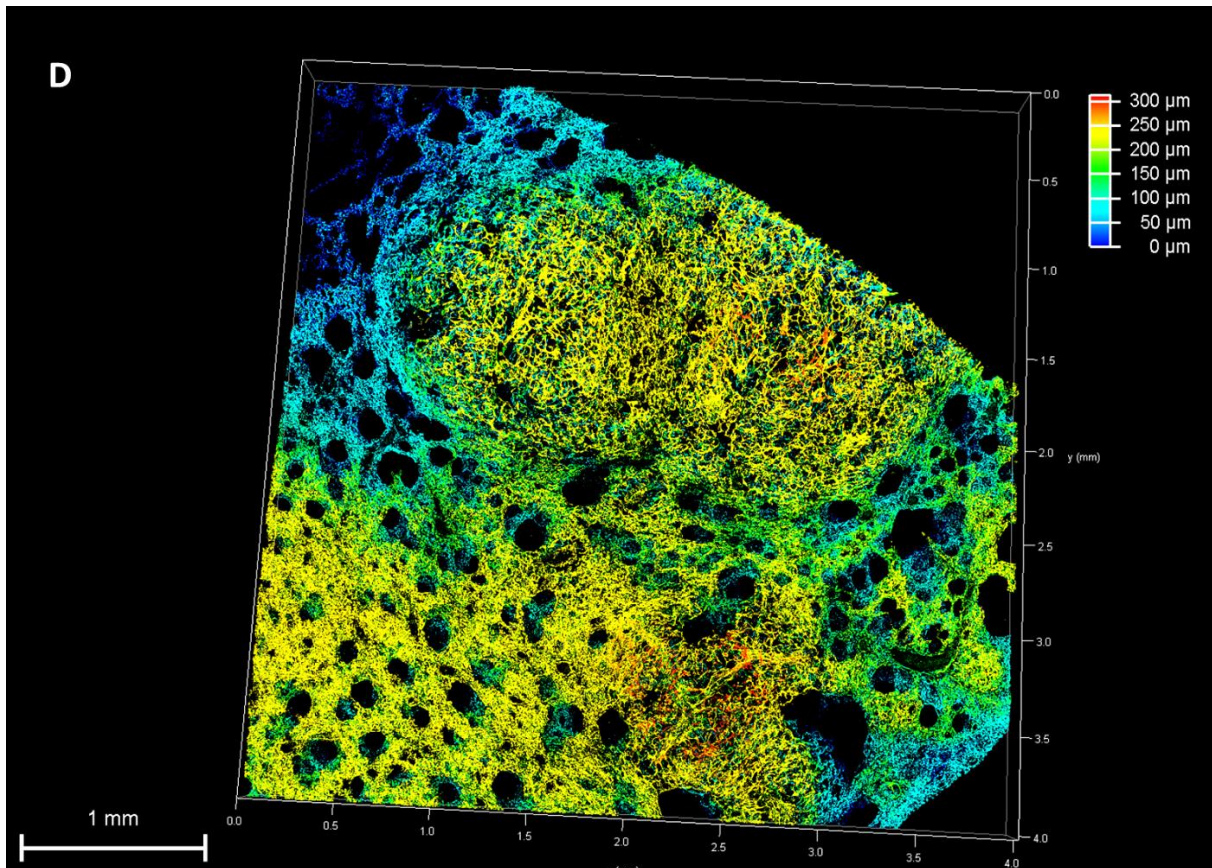


Figure 15. 3D imaging of paraffin-embedded lung metastases tissue co-stained with Sytox green and anti-CD31 antibody after ExM. **A:** The lung metastasis nodules and normal lung tissue were stained with Sytox green (blue) to show the profile structure of the tumor nodules and normal lung tissue around it. High intensity and accumulation of Sytox green can be detected in the tumor nodules. **B:** 3D image of complex vascular network (red) in lung metastasis nodules and normal lung tissue stained with anti-CD31 antibody. **C:** Overlay image of the Sytox green (blue) and anti-CD31 antibody (red) staining. **D.** Depth coding image of the anti-CD31 antibody stained vascular structure (B) in lung metastases and normal lung tissue. The scan depth of 310 μm was used as indicated by the depth-coding bar with color. All the data were imaged by 20x objective of LCFM.

3.5 3D visualization and quantitative analysis of the neutrophil cell distribution in paraffin-embedded lung metastases

Immune cell content and distribution in the tumor microenvironment can provide valuable information about metastasis, prognostic and possibly therapeutic strategy in tumor progression. To further extend the applicability of the ExM protocol, we sought to investigate the efficacy of this method for detecting and quantifying the neutrophil

cell invasion in lung metastases. (Experiments were performed five times and repeated with similar results)

Using ExM and anti-Ly6G antibody immunofluorescence staining, the 3D distribution of Ly6G-positive neutrophil cells (red) residing in the lung metastasis nodule and adjacent lung tissue was successfully visualized (**Fig. 16**). It is obvious that an increased number of Ly6G-positive neutrophil cells is observed in the lung metastasis nodule as compared with the surrounding lung tissue, suggesting the active recruitment of neutrophil cells during lung metastasis development.

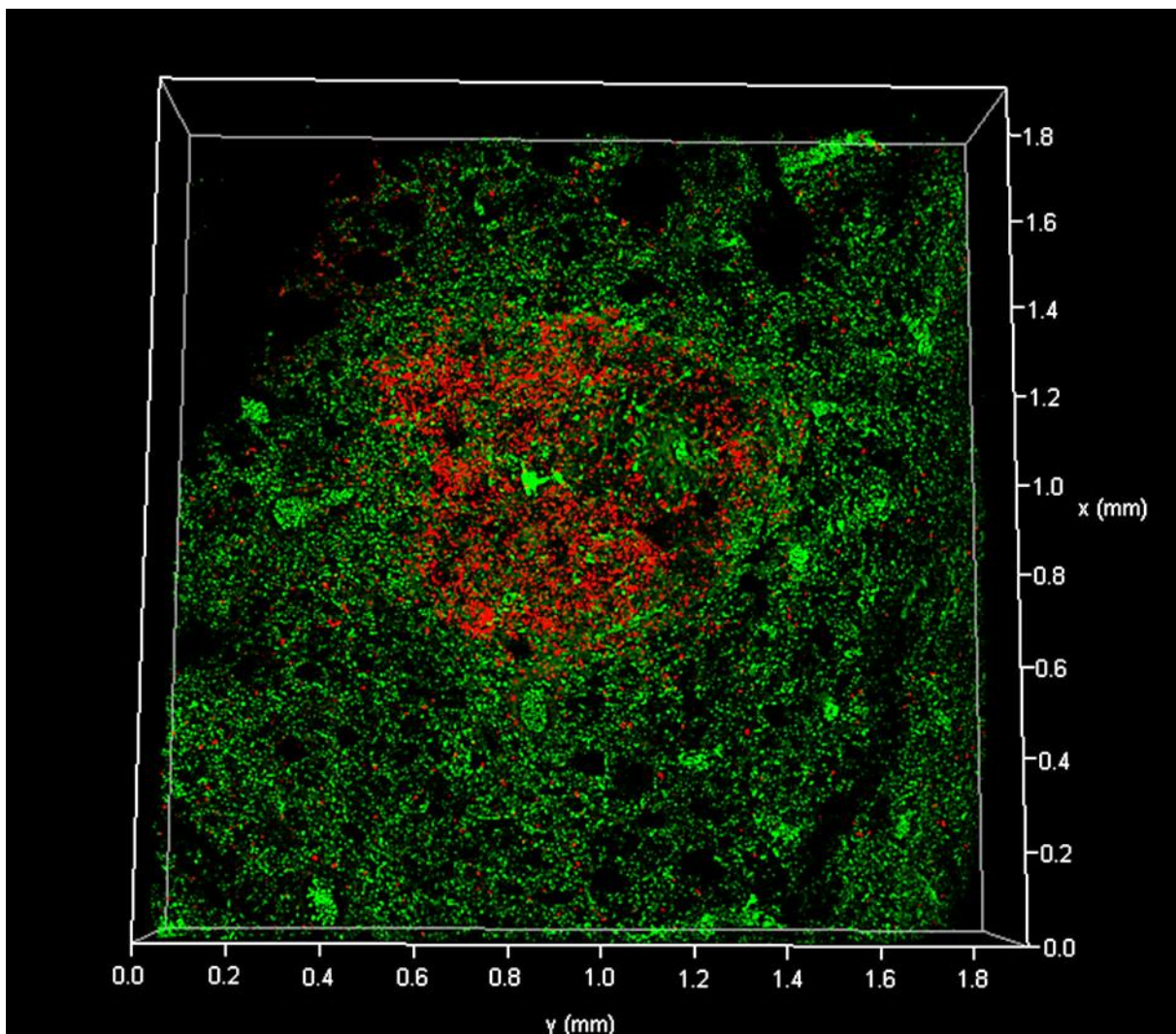
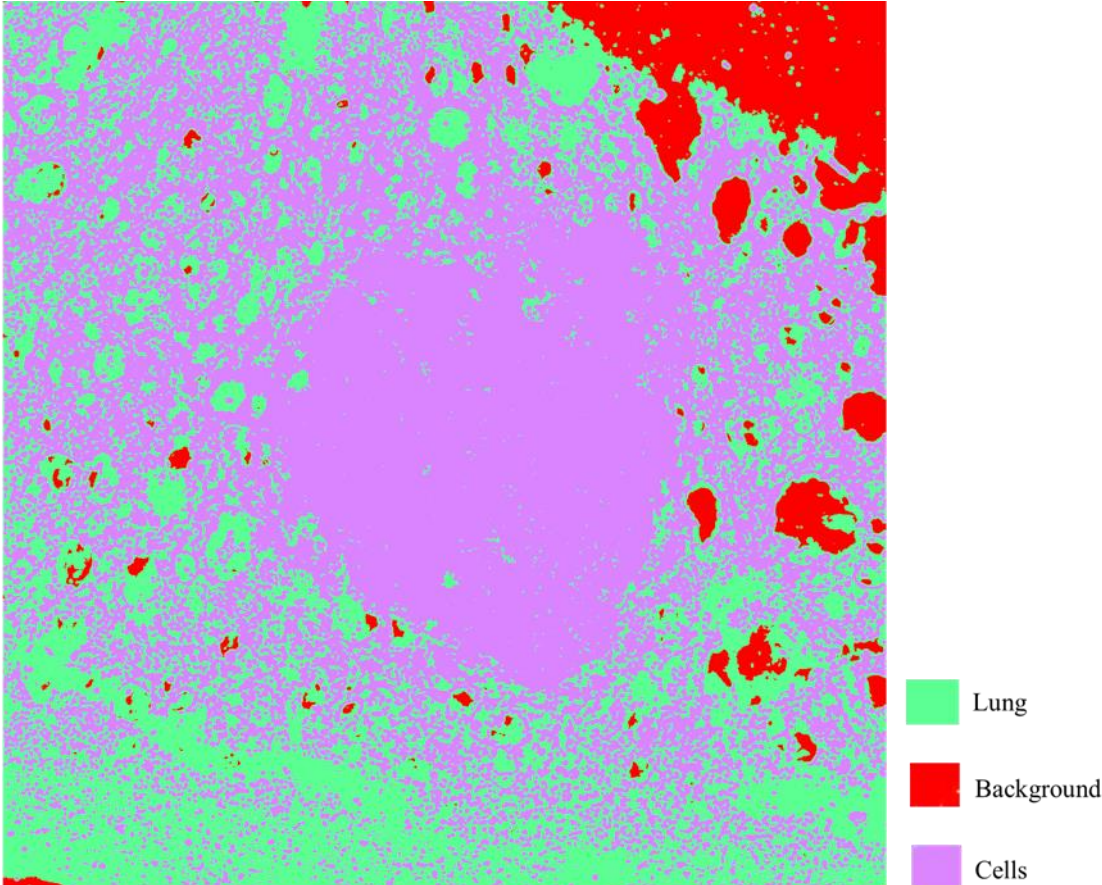
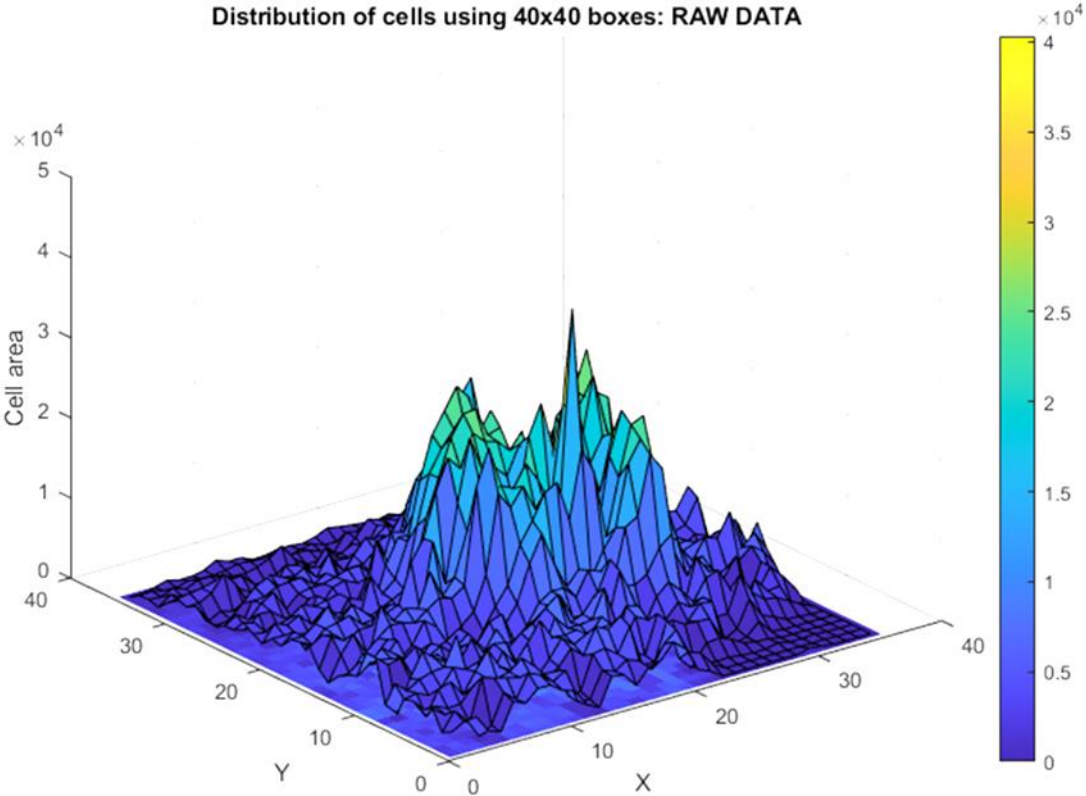


Figure 16. 3D mapping of the neutrophil cell distribution in paraffin-embedded lung metastases. The distribution of Ly6G-positive neutrophil cells (red) residing in the lung metastasis nodule and adjacent lung tissue was successfully visualized by 20 \times objective of LCFM after ExM. Obviously, an increased number of Ly6G-positive neutrophil cells occurs in the lung metastasis nodule as compared with the adjacent lung tissue. Green fluorescence was used to identify tissue profile structure by autofluorescence.

A



B



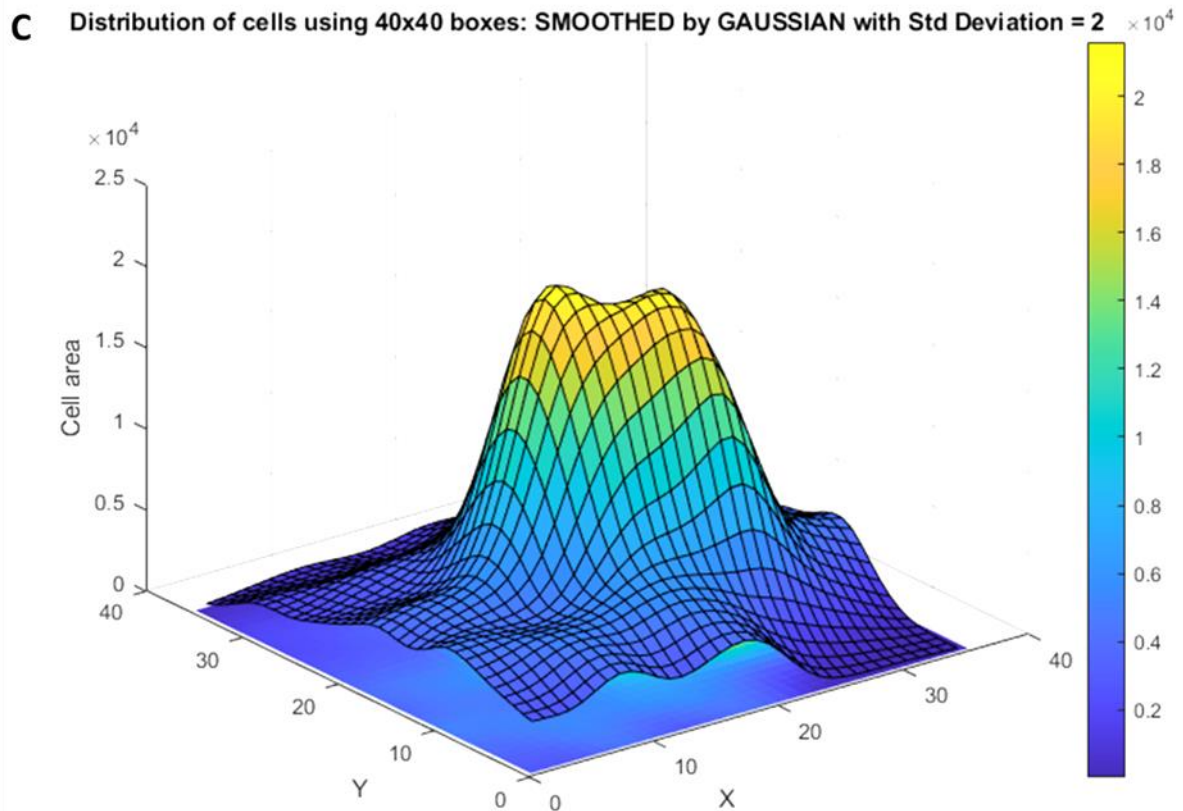


Figure 17. 3D quantitative analysis of neutrophil cells distribution in the lung metastases and adjacent lung tissue by Fiji and MATLAB. **A:** Maximum intensity projection of Fig.16. Green: lung tissue; red: background; purple: neutrophil cells. **B:** 3D plot of neutrophil cells distribution using 40x40 pixels grids: Raw data. **C:** The smoothed raw data of neutrophil cells distribution. The color bar represents the total pixels occupied by neutrophil cells.

As shown in **Fig.17A**, the maximum intensity projection of Fig.16 was obtained after 3-class classification using Fiji plugin, Trainable Weka Segmentation. It demonstrates that there is a distinct accumulation of neutrophil cells (purple) in the lung metastases, which is indicated by the area showing the lack of lung tissue (green). For 3D distribution plot, MATLAB was used. We were able to get a 3D plot of neutrophil cells distribution and a smoothed raw data using a Gaussian filter with standard distribution of 2 (**Fig.17B and 17c**), which obviously give a better understanding of the amount of neutrophil cells accumulation in lung metastases in 3D level. This analysis revealed a significant imbalance of neutrophil cells accumulation between the lung metastases and peripheral lung tissue.

4 DISCUSSION

The results of this thesis can be summarized as follows:

1. A protocol for a retrograde perfusion combined with trachea ligation of the lung in mice was established. It was possible to harvest the perfused lungs while preventing a collapse of the alveoli. Furthermore, it could be demonstrated that using our MHI148-PEI dye it was possible to stain the vasculature of an entire lung during perfusion. Thus no incubation with an antibody was needed.
2. The lung could be easily cleared by using ECI. Furthermore, the ECI could be removed and a normal immunohistochemistry could be performed.
3. A protocol was established allowing expansion of the lung (ExM).
4. A protocol was introduced to “revitalize” 20 year old paraffin embedded lungs allowing the staining of the vasculature.
5. In addition, 10 years old paraffin embedded lung metastases were visualized and their microvasculature were identified. During this process, it was noted that different tissue types (metastasis versus normal lung) expanded differently.
6. We were able to visualize and quantitative analyze the neutrophil cell distribution in paraffin embedded lung metastases.

4.1 Animal perfusion

The perfusion technique aims to remove as much blood as possible from the animal before harvesting the different organs. As the lung is a soft organ full of air it is prone to collapse after harvesting. Thus special procedures must be considered in collecting and preserving the tissue, especially for the morphological studies of the lung. There are many different methods of lung fixation/preservation: (1) right ventricular perfusion, (2) trachea instillation of fixative solution, (3) intrathoracic in situ fixation (Braber et al., 2010; Gandjeva and Tuder, 2018). However, *Hausmann* et al. demonstrated that none of these techniques could completely meet the requirements of morphological study in lung (Hausmann, 2006). The right ventricular perfusion can flush away the blood from the pulmonary vascular system completely, but severe edema may occur when the lung is perfused with inappropriate pressure values. Another weakness is that a lung collapse happens after opening the thoracic cavity due to the loss of the negative

pleural pressure. Trachea instillation with fixation solution can preserve lung tissue and keep the lung inflated in a good way, but it always results in microarchitecture distortion and size changes of the alveoli by unstable pressure perfusion. *Ochoa et al.* reported that they extracted the lung after transcatheter perfusion combined with tracheal instillation, however, the lung was still unevenly expanded after collapsing during transcatheter perfusion (Ochoa et al., 2018). It was quite hard to control the perfusion pressure manually. The intrathoracic *in situ* fixation can provide the best protective effect for the morphology of the alveoli and air space volume since lungs are extracted after the intact thorax *in toto* were fixed in formaldehyde solution for nearly 1 week (Hausmann et al., 2004). However, it always takes such a long time to complete fixation of both the lungs and thoracic cavity together, and blood still exists in the vasculature.

In our retrograde perfusion protocol, we perfuse the mice via the abdominal aorta to keep the thoracic cavity intact through the whole perfusion process. Thoracic cavity integrity is the most critical factor to maintain the negative pleural pressure that keeps the lungs expanded (Negrini and Moriondo, 2013).

During our perfusion process lung tissue will be kept inflated all the time because the operation site of perfusion is in the abdomen. Since a Jun-Air compressor and a syringe pump drive the perfusion system and all of them are connected with tubes, it is pressure- and volume-controlled. After the perfusion with a saline/heparin and 4% PFA solution at a constant pressure, the whole blood of the mice is flushed away and lungs are also preliminarily fixed without any structural distortion. Furthermore, after perfusion, the cervical part of trachea was isolated and ligated with a suture to avoid the lungs to collapse before opening thoracic cavity to extract the lungs. Based on all the images of perfused lungs in the result part (Fig. 6-11), we demonstrate that the lung morphology is very well preserved by our retrograde perfusion protocol combined with trachea ligation.

The retrograde perfusion protocol also allows collecting all the organs in mice, which is consistent with animal protection welfare principles (3R). Additionally, the staining dyes can be perfused throughout the whole body of the mice that enables the staining and harvesting of all organs in one time and incubations with dyes are no longer needed.

4.2 ECI-based OTC

In 3D imaging the dye with a proper wavelength should be considered according to the imaging purposes. For example, a bright fluorescent dye, which is close to infrared wavelength, can always give better result due to their low signal to noise ratio and higher penetration rate into the tissue (Renier et al., 2014). MHI148-PEI, a dye previously developed at the Medical Research Center of the Universitätsklinikum of Mannheim, Germany, is characterized with a large number of positive charges, infrared fluorescence emission and high molecular weight (Huang et al., 2019). The positive charges come from the branched PEI group and can promote the electrostatic binding of the dye and the glycosaminoglycans on the vessel wall (Longmire et al., 2008). As expected, in the Fig. 6-7, the infrared fluorescence spectra of MHI148-PEI gives good results about lung vasculature due to its deep penetration depth into tissue and high signal-to-noise ratio (Huang et al., 2019).

In our experiments, we always imaged the samples with a 488 nm laser to get tissue autofluorescence, which was a powerful tool to distinguish the profile structure of the tissue. The intrinsic autofluorescence arises from endogenous fluorophores, such as mitochondria, lysosomes, NADPH, flavin coenzymes, and collagen in extracellular matrix, which are unevenly distributed in different components of the tissue (Croce and Bottioli, 2014; Monici, 2005). Even though the autofluorescence is often considered as noise or background, some studies have already demonstrated that the intensity and distribution changes of autofluorescence could be applied in basic research and diagnostics without any external probes in cell biology and tissue histology (Jamme et al., 2013; Rivenson et al., 2019).

The ECI based OTC protocol was firstly reported by *Klingberg et al* in kidney research (Klingberg et al., 2017). Different from other organic solvent based OTC techniques, ECI is a cheap, non-toxic and ready-to-use solvent which is quite suitable for an efficient and fast clearing process. In the past two years, it is becoming more and more popular in different tissues apart from the kidney. *Saritas et al.* reported that multicellular microstructures of thick mouse kidney slices could be visualized in 3D after antibody labelling combined with ECI based OTC by conventional confocal microscopy (Saritas et al., 2019). *Saritas et al.* also demonstrated that a low potassium

dietary promotes the proliferation of distal convoluted tubules and medullary collecting ducts by immunolabeling after ECI based OTC (Saritas et al., 2018).

Henning et al. developed a new protocol that combined immunolabeling and ECI based OTC with an effective melanin bleaching step, which enabled 3D investigation of vascular leakage and neovascularization in the intact eyeballs (Henning et al., 2019). Using simple ECI based OTC clearing and light sheet microscopy, *Grüneboom et al.* found that there are hundreds of trans-cortical-vessels connected to the periosteal circulation in both mouse and human long bones, which permits a rapid transportation of neutrophil cells from bone marrow into the general circulation for host defense (Grüneboom et al., 2019). *Masselink et al.* verified that ECI based OTC method could be used in a wide range of biological models, such as zebrafish, axolotl, human organoids and *Drosophila melanogaster*. More importantly, the normally used fluorescent conjugations, including Alexa Fluorophores, GFP, mCherry and Brainbow, all “survived” the whole ECI clearing process (Masselink et al., 2019). However, there is not any specific report about the ECI based OTC in the histological morphology of the lung until now. The current protocols are also hampered by the long processing time and are labor intensive.

In the previous study, our group optimized the primary ECI based OTC protocol reported by the *Klingberg’s* group. We reduced the whole processing time from one day or several weeks to only 4 hours without any compromised clearing efficacy. The whole dehydration and clearing process were performed under vacuum and at room temperature by an automatic tissue processor, which allows high throughput and is more efficient. The room temperature and vacuum can improve the diffusion of reagents into the tissue. The samples were brought from 50% directly to 80% ethanol in the optimized protocol instead of from 30% to 70% ethanol in the original. This change was adopted to ensure a faster and stronger dehydration.

Additionally, the fluorescence intensity of the dye can be better preserved in the ECI, even for a long time storage, as compared with other clearing methods (Huang et al., 2019). Using confocal microscopy the MHI148-PEI fluorescent dye can still be detected in the kidney after being stored in ECI for more than one year. However, in the widely used 3DISCO protocol, one of the key drawbacks is the severe degradation

of the fluorescent signal (Erturk et al., 2012). In the Fig. 6-7, we demonstrate that our optimized ECI based OTC protocol also works well with lung tissue and MHI148-PEI staining, which enables 3D imaging of the lung vasculature.

Bronchial angiogenesis and remodeling of pulmonary circulation are reported to decline during the progression of many chronic lung disorders, such as asthma, chronic obstructive pulmonary disease, lung transplantation and even pulmonary hypertension after heart transplantation (Delgado et al., 2005; Harkness et al., 2014). The advantage of our imaging protocol is that the whole vasculature can be imaged in 3D and that it will enable an automated quantification of 3D projection and surface reconstruction in a quick way. Therefore, it could be a powerful tool for the research of vascular remodeling-related lung diseases.

Nowadays, macromolecular drugs, for example, antibodies, proteins, hormone therapy and target/immunotherapy, play an important role in the treatment of various kinds of cancers (Carter and Lazar, 2018; Serna et al., 2018). However, these drugs display different vascular penetration rates, tumor distribution profiles and pharmacokinetic characteristics in the human body circulatory system and tumor tissue (Thurber and Weissleder, 2011). Our protocol could also be used to image and analyze the spatial distribution, vascular extravasation and penetration of these macromolecular drugs in the lung cancer or metastases in 3D level, which is critical to the new anti-tumor drug development. At the same time, researchers are also encouraged to extend this protocol to test its availability on other vascular related diseases of the lung, especially with regard to the whole mount structures with 3D projection.

In the next step, we tried to combine the optimized ECI based OTC with the conventional antibody staining to extend the scope of application. Different protocols, including immunofluorescence staining before- and after- ECI clearing, had to be established in the 3D imaging of the lung tissue. Even though the immunofluorescence staining and imaging works well in both of the protocols (data not shown), the alveoli were mostly deformed at last. The main reason might be that the structural stability of intact alveoli was destroyed due to the long-term immersion in antibody staining and washing. However, it is unavoidable that it always takes quite a long time to finish 3D immunofluorescence labeling because of the low antibody penetration rate in thickness

tissues (Renier et al., 2014). Then, we decided to develop another 3D immunofluorescence labeling and imaging protocol for the lung tissue research, in which alveoli structure should be well preserved through the whole process.

Summary of this part is: our research demonstrates that the 3D distribution of lung vasculature can be imaged after perfusion with the newly developed MHI148-PEI dye and ECi-based OTC in a time saving and highly efficient way. In the future, this protocol definitely has a high potential to be used in pathology for the analysis of vessel related diseases of the lung.

4.3 ExM and 3D immunofluorescence

Expansion microscopy (ExM) is a recently developed method that enables 3D high resolution imaging by isotropically and smoothly expanding labels or biomolecules fixed in a dense, cross-linked swellable polyelectrolyte hydrogel away from each other (Chen et al., 2015). By this way, labels in a diffraction-limited area are separated in a high distance and can be resolved by conventional microscopes.

In the past few years, a diversity of ExM protocols for 3D high-resolution imaging of different samples have been reported. *Chozinski et al.* demonstrated that the fine structural details, including glomerular basement membrane, cytoskeleton and podocyte foot processes of mouse and human kidney tissue that traditionally could only be visualized by electron microscopy, could be imaged and measured by using ExM with a conventional confocal microscopy. This accessible and inexpensive protocol enables volumetric interrogation of kidney tissue with 70-300 nm resolution (Bucur and Zhao, 2018; Chozinski et al., 2018). Apart from the normal tissue, *Jiang et al.* applied an ExM protocol in a 3D imaging study of fine intracellular structures and interactions of *Drosophila* embryos, larval brains and body walls (Jiang et al., 2018). They revealed features of presynaptic active zone that could not be observed with standard confocal microscopy. Altogether, they recommended optimizing tissue-specific ExM protocols for different research objectives. Combining super-resolution with ExM, for the first time, *Cahoon et al.* proved that there are two visually distinct layers in the *Drosophila* synaptonemal complex, perhaps suggesting that each layer connects one sister chromatid from each homologous chromosome (Cahoon et al.,

2017). This could contribute to understand the architecture and mechanics of the synaptonemal complex protein.

The ExFISH protocol was also established for expansion microscopy of mRNA as well as long noncoding RNAs in both cultured cells and intact brain tissue, which enabled 3D high-resolution imaging of RNA structure and location in thick tissues (Asano et al., 2018; Chen et al., 2016). Apart from intracellular structures like centrioles, proteins and mRNA distribution in cells and tissues, many other studies proved that ExM is even suitable to study bacteria and larger viruses, including influenza, herpes or HIV down to a particle size of 65 nm (Kunz et al., 2019). *Lim et al.* extended the application of ExM protocol to bacteria studies and demonstrated its applicability in imaging microbial communities and cell-to-cell heterogeneity among bacteria infected macrophages (Lim et al., 2019).

Zhao et al. applied a modified ExM protocol, which was named: expansion pathology (ExPath), into 4 μm slices of normal lung and lung cancer, but the quality of the 2D image was so poor and the information obtained by these thin slices were limited (Zhao et al., 2017). Hence, the application of ExM protocol in lung tissue and -related diseases has so far been limited.

Based on the powerful ability of tissue clearing and the principle of embedding tissue in a dense swellable polymer network, we speculated that ExM protocol might be helpful to preserve the lung morphology in the immunofluorescence labeling and 3D imaging. Therefore, in the next part, our research focused on the high-resolution 3D imaging of lung using ExM. At the beginning, we tried to reveal the 3D structure of the perfused normal lung by ExM combined with immunofluorescence staining with different antibodies. The majority constituents of lung are capillary and alveoli, which are mainly made up of vascular endothelial cells and type I alveolar epithelial cells, so the specific markers to them were chosen to image the normal lung structure. As mentioned above, the tissue intrinsic autofluorescence can be used to detect the profile morphology of samples. We found that both of the large vessels and bronchi showed high intensity of autofluorescence after ExM, but it was hard to recognize the structures individually. With immunofluorescence labeling of the specific vascular endothelial cell marker-anti-CD31 antibody, we can easily distinguish the vessels from bronchi in 3D,

as shown in Fig.8. In Fig. 9, the 3D high-resolution structure of alveoli and capillaries in the alveolar interstitium were visualized by ExM and immunofluorescence labeling with anti-AQP5 and anti-CD31 antibody using a 63× high magnification objective, which has never been reported in previous research. The traditional methods to analyze pulmonary microvascular and alveolar epithelial permeability are lung dry/wet ratios, Evans blue fluorimetry and albumin concentration ratios between blood and bronchoalveolar lavage fluid (Gao et al., 2011; Peng et al., 2019). All of these indicators are indirect measurement methods based on the vascular pathophysiology. Regarding the high-resolution 3D structure of alveoli and interstitial, we hypothesize that the pulmonary microvascular and alveolar epithelial permeability may be analyzed by high-resolution 3D imaging with specific marker labelling directly in the future.

Bronchial cilia, the main components of the mucociliary clearance system, transport inhaled foreign substances, including irritants, dust, mucus, microorganisms and so on, out of the respiratory tract (Ganesan et al., 2013). This kind of defense mechanism is the so-called first innate protective barrier of our human body. The patients with primary ciliary dyskinesia and cystic fibrosis are susceptible to recurrent infections of the airways and lung due to the defects of mucociliary clearance system (Munkholm and Mortensen, 2014; Robinson et al., 2000). Apart from congenital defect disease, viral or bacterial infection and cigarette smoking can also cause a severe loss of cilia due to the apoptotic effect of inflammation (Wang et al., 2012; Wu et al., 2016).

However, most of the data about cilia in bronchi were obtained by electronic microscopy or immunofluorescence staining with slices. Although the electronic microscopy can obtain a high resolution scanning, it is expensive and the image acquisition can be so complex. For the immunofluorescence staining with slices, they could only image a small area of the bronchi and the image quality is often poor. It is hard to demonstrate the ciliary changes caused by congenital or exogenous factors. Therefore, we highly recommend revealing the ciliary abnormalities by our 3D imaging protocol in pulmonary diseases. Our approach can definitely give a high resolution and comprehensive overview.

For other structures than the cilia on the surface of bronchial epithelium, we tried to test our protocol in the full thickness of bronchial epithelium with the widely expressed

epithelial cell marker: anti-E-cadherin antibody. The Fig. 11 demonstrates that the anti-E-cadherin antibody penetration in the full thickness of the bronchial epithelium is excellent and it gives a good staining. Bronchial epithelium remodeling, including loss of epithelium integrity, sub-epithelium fibrosis, thickening of basement membrane, increased smooth muscle layers, submucosal gland enlargement and neovascularization, occurs in almost all airway diseases, among them the most typical diseases are chronic obstructive pulmonary disease and asthma (James et al., 2002; Redington and Howarth, 1997; Saetta et al., 2001; Schmiesing, 2004). At present, assessment methods of body fluids, such as bronchoalveolar lavage fluid, induced sputum, blood and exhaled breath condensate, provide only indirect indicators of the inflammatory and remodeling processes that may be going on. However, these indirect markers are mostly not so specific to the airway duct or can be affected by so many external factors, and the results always lack spatial localization.

The standard techniques for the assessment of bronchial epithelium remodeling mostly rely on histochemical and immunohistochemical staining with 4 μm slices to detect the changes of collagen, mucus glands, extracellular matrix proteins and profibrotic cytokines (Bergeron et al., 2007; Jeffery et al., 2003). The assessment methods of thin sections are more likely to cause significant regional sampling biases due to the only small areas, which prohibits the analysis of airway remodeling over large volume (Antonioni et al., 2015). The ExM protocol employed in our study allows evaluation of epithelial components throughout the full thickness of bronchi and the lung tissue around in 3D with a high resolution, which can be used to investigate the spatial distribution of collagen, immune cells and cytokines in the process of airway remodeling in the future. It may also be helpful to provide a global 3D view of pathological structure changes in the evaluation of developing new treatment strategy for the airway diseases.

4.4 ExM with lung metastases from paraffin blocks

In order to make a wider use of the ExM technique possible, its compatibility with material from paraffin blocks was verified in the next study. *Zhao et al.* developed an ExPath protocol and applied it in the human tissue specimens fixed with formalin and embedded in paraffin (Zhao et al., 2017). However, only sections were used in the ExPath protocol and the quality of 2D images was poor. *Nojima et al.* applied the

CUBIC pipeline, another tissue clearing and 3D imaging technique, to paraffin embedded tumor tissue blocks from patients (Nojima et al., 2017). This protocol works well with paraffin blocks, but the resolution of the 3D images was too low and the information was limited. In our research, paraffin embedded lung tissue blocks were recovered using deparaffinization and rehydration, and then they were processed with the ExM protocol directly. Fig.12 and Fig.13 demonstrate that the conventional anti-CD31 antibody and ExM protocol are working not only with newly PFA-fixed lungs but also with thick lung tissue derived from paraffin blocks, which definitely will promote the application of our ExM protocol in the clinical diagnostic pathology. Since the tissue size uniformly expands two times after denaturation, the resolution of images achieved by ExM is at least 2x2x2 times higher than the traditional histological assessment under the same confocal microscope.

Based on the nice immunofluorescence staining and 3D structure of lungs achieved by ExM, we decided to apply it in the study of vasculature and neutrophil cells in the lung metastases, which are interesting research targets concerning the treatment of tumors (Bird, 2016; Hanahan and Weinberg, 2011). The formation of complex vasculature networks / tumor angiogenesis, which not only supplies nutrients required for tumor growth but also provides a metastatic route, is a well-recognized feature of cancer (Ronca et al., 2017). Previously, researchers mainly focused on inhibiting tumor growth and metastasis by preventing or destructing tumor angiogenesis to starve the tumor (Lange et al., 2011; Shahneh et al., 2013).

The most popular therapeutic intervention for suppressing tumor angiogenesis is the application of bevacizumab, a human anti-VEGF antibody, which has been assessed in more than three hundred clinical trials in nearly twenty different kinds of tumor types (Heath and Bicknell, 2009). Despite of the conventional theory that anti-angiogenic therapy inhibits tumor growth and metastasis, growing evidence demonstrates that the anti-angiogenic strategy may result in intratumoral hypoxia due to the vascular regression and rarefaction, and eventually leads to increased tumor invasion, drug resistance and metastasis (Ebos et al., 2009; Paez-Ribes et al., 2009).

On the other side, due to the imbalance of pro-angiogenic and anti-angiogenic signaling pathways in tumor progression, tumor vessels are morphologically and

functionally distinct from the normal vasculature. The dysfunctional tumor vasculature is always leaky, immature, disorganized, dilated, saccular, malformed, tortuous, and has random interconnections as also shown in our 3D data. This situation has a profound influence on tumor microenvironment changes and drug delivery in tumors (Hagendoorn et al., 2006; Jain, 2005, 2008). In the last decades, many groups tried to “normalize” the tumor vasculature to increase drug delivery, which makes the tumor cells more vulnerable to the treatments (Jain, 2001).

This is a paradoxon. One would expect that destroying the tumor vasculature would starve the tumor; however, another thought is that it would render many drug treatments less effective and accelerate tumor metastasis. Thus normalizing the abnormal tumor vasculature is expected to enhance the efficacy of many chemotherapy and radiation therapies as it increases the delivery of drugs and oxygen to tumor parenchyma. The reason may be that the comprehensive structure of vessels in tumor and its relationship with tumor progression are still unknown at present. Therefore, we highly recommend applying our ExM protocol into the research of tumor angiogenesis in the future. It will definitely be helpful to get an overall view of morphological changes of vasculature in the tumor. Then, the relationship between tumor vasculature and tumor progression can be investigated more easily and in more details on the 3D level. The ExM protocol combined with quantification analysis software can also be used to develop and assess new treatment approaches based on tumor vasculature.

We found that the metastasis nodules were revealed automatically with a clear circular boundary after ExM by confocal microscopy. In Fig. 14C, the dark area in the central part of the tissue indicates that part of the sample is out of the focus plane; however, the normal lung around the tumor nodule can be imaged in focus at this point. This phenomenon has never been reported in other histological research on lung metastases, even with other 3D imaging methods. It means that the surface of metastases and normal lung tissue around are not in the same plane after ExM anymore. A different composition and different structure of the tissues certainly play key roles in response to the ExM protocol. Therefore, we speculate that the lung metastases and normal lung tissue around were expanded differently since they are made up of different kinds and amount of cells and matrix. Then, the metastatic

nodules showed up automatically, which may be helpful to detect micro-metastases in the lung.

More and more reports are presented targeting the non-tumor cell components of the microenvironment, which might be a novel therapeutic approach. Immune cells, especially neutrophil cells, dynamically regulate tumor progression and remote organ metastasis (Joyce and Pollard, 2009; Ostrand-Rosenberg, 2008). *Wculek et al.* demonstrated that neutrophil cells are the main driver of the pre-metastatic lung microenvironment and support metastatic initiation in breast cancer models. Pre-metastatic neutrophil cell depletion by using anti-Ly6G blocking antibody caused a significant decrease of spontaneous metastasis (Wculek and Malanchi, 2015). However, the assessment methods of neutrophil cells mostly depend on histological examination of thin histology slices or flow cytometry. Tumor biology can vary between the surface and center part, especially compared with the tumor adjacent and healthy tissue. The therapeutic interventions, such as chemotherapy and immune therapy can also effect the neutrophil cell polarization, accumulation and distribution (Coffelt et al., 2016; Donskov, 2013; Fridlender et al., 2009; Hiratsuka et al., 2006). However, the information about spatial distribution and heterogeneity of neutrophils in tumor and surrounding tissue are still limited.

Our ExM protocol enables 3D imaging to reveal the spatial distribution of neutrophil cells in lung metastases with high resolution and less tissue deformation. By quantitative analysis using Fiji and MATLAB, we were able to quantify the cell density and verify the distinct localization of neutrophil cells in lung metastases as compared with the adjacent lung tissue in 3D level. Since the neutrophil cells are tightly packed into clusters, we might not be able to obtain the actual number of neutrophil cells in the whole tissue. However, the total pixels of neutrophil cells by our statistical analysis method can definitely reflect the actual amount of neutrophil cells in the tissue because the pixels of single cell are almost fixed. This enables a detailed and comprehensive visualization and analysis. Therefore, it should be useful to reveal changes of neutrophil cells or other microenvironment components in detail, especially the 3D spatial relationship between each other, in tumor progression and new treatment strategy development.

In our present study, we typically utilize the ExM protocol, which is compatible with immunofluorescence staining and provides excellent 3D imaging of lung tissue. The ExM protocol is suitable for PFA perfused and post-fixed samples as well as deparaffinized and rehydrated paraffin embedded tissue blocks. The proportion of each hydrogel composition is critical. It needs to be not only sufficiently dense to lock the proteins stably, but also loose enough to allow the opaque lipids to be washed away by the detergent flowing through the sample. When the hydrogel is polymerized, it locks proteins and acts as a scaffold in place that greatly helps to preserve the morphology of lung tissue in the subsequent staining and imaging processes (Alon et al., 2019; Chen et al., 2015).

A higher level of ExM and resolution rate can be achieved by modifying the proportion of hydrogel components. For example, a low concentration of the cross-linker will result in more expansion, whereas a higher concentration of the cross-linker will result in less expansion (Wassie et al., 2019). We found that, for the lung tissue, the density of probes and proteins turn to be too sparse upon massive excessive expansion. Indeed, twofold expansion already effectively reduces the proteins density to eightfold in 3D level. To avoid this situation, we highly recommend to limit the ExM to twofold, and to combine it with high magnification microscopy to analyze the structure of the samples after denaturation. Overall, our protocol was done to perform more effectively high-resolution 3D imaging of lung tissue, especially for healthy and lung metastases from fresh fixed or deparaffinized tissue blocks.

In order to perform high magnification microscopy definitely new objectives with longer working distances have to be developed.

In summary: we established retrograde perfusion technique for the lung providing a better maintenance of lung morphology. Furthermore new clearing protocols were established for the lung allowing 3D imaging even of material from paraffin blocks.

5 SUMMARY

Lung tissue is difficult to analyze histologically, especially if the tissue is obtained from experimental animals. Most lung harvesting techniques result in a collapse of the organ. The aim of this thesis was to optimize the organ harvesting strategy and to introduce / analyze new 3D imaging strategies / protocols to be used in thick organ slices.

The results of this thesis can be summarized as follows:

- i. The retrograde perfusion combined with trachea ligation technique can be used in the research of lung pathology in mice. As compared with the normal trans-cardiac perfusion technique, this approach is much easier in handling and results in a much better maintenance of lung morphology.
- ii. Ethyl cinnamate based optical tissue clearing method can be applied to do the 3D imaging of lungs.
- iii. MHI148-PEI, a cationic near infrared fluorescent agent developed by our group, is an ideal dye to stain the lung vessels during perfusion.
- iv. Expansion microscopy combined with antibody immunofluorescence staining protocol was established for 3D imaging of lung tissue with high resolution, by which we revealed the 3D structure of the alveoli and vasculature in lung.
- v. We also demonstrated that expansion microscopy was applicable to paraffin embedded lung tissue blocks.
- vi. By expansion microscopy, we could image the vasculature in lung metastases tissue as well as neutrophil cells from paraffin blocks.

In this thesis new 3D imaging protocols and organ harvesting strategies could be established allowing new analyses of lung tissue.

6 REFERENCES

- Alon, S., Huynh, G.H., and Boyden, E.S. (2019). Expansion microscopy: enabling single cell analysis in intact biological systems. *The FEBS journal* 286, 1482-1494.
- Antoniou, K.M., Tomassetti, S., Tsitoura, E., and Vancheri, C. (2015). Idiopathic pulmonary fibrosis and lung cancer: a clinical and pathogenesis update. *Current opinion in pulmonary medicine* 21, 626-633.
- Asano, S.M., Gao, R., Wassie, A.T., Tillberg, P.W., Chen, F., and Boyden, E.S. (2018). Expansion Microscopy: Protocols for Imaging Proteins and RNA in Cells and Tissues. *Current protocols in cell biology* 80, e56.
- Bergeron, C., Tulic, M.K., and Hamid, Q. (2007). Tools used to measure airway remodelling in research. *The European respiratory journal* 29, 596-604.
- Bird, L. (2016). Tumour immunology: Neutrophils help tumours spread. *Nature reviews Immunology* 16, 74-75.
- Booth, M.E., Treanor, D., Roberts, N., Magee, D.R., Speirs, V., and Hanby, A.M. (2015). Three-dimensional reconstruction of ductal carcinoma in situ with virtual slides. *Histopathology* 66, 966-973.
- Boutin, M.E., and Hoffman-Kim, D. (2015). Application and assessment of optical clearing methods for imaging of tissue-engineered neural stem cell spheres. *Tissue engineering Part C, Methods* 21, 292-302.
- Braber, S., Verheijden, K.A., Henricks, P.A., Kraneveld, A.D., and Folkerts, G. (2010). A comparison of fixation methods on lung morphology in a murine model of emphysema. *American journal of physiology Lung cellular and molecular physiology* 299, L843-851.
- Bucur, O., and Zhao, Y. (2018). Nanoscale Imaging of Kidney Glomeruli Using Expansion Pathology. *Frontiers in medicine* 5, 322.
- Cahoon, C.K., Yu, Z., Wang, Y., Guo, F., Unruh, J.R., Slaughter, B.D., and Hawley, R.S. (2017). Superresolution expansion microscopy reveals the three-dimensional organization of the *Drosophila* synaptonemal complex. *Proceedings of the National Academy of Sciences of the United States of America* 114, E6857-e6866.
- Carter, P.J., and Lazar, G.A. (2018). Next generation antibody drugs: pursuit of the 'high-hanging fruit'. *Nature reviews Drug discovery* 17, 197-223.
- Chakraborty, T., Driscoll, M.K., Jeffery, E., Murphy, M.M., Roudot, P., Chang, B.J., Vora, S., Wong, W.M., Nielson, C.D., Zhang, H., *et al.* (2019). Light-sheet microscopy of cleared tissues with isotropic, subcellular resolution. *Nature methods* 16, 1109-1113.
- Chen, F., Tillberg, P.W., and Boyden, E.S. (2015). Expansion microscopy. *Science (New York, NY)* 347, 543-548.

Chen, F., Wassie, A.T., Cote, A.J., Sinha, A., Alon, S., Asano, S., Daugharthy, E.R., Chang, J.B., Marblestone, A., Church, G.M., *et al.* (2016). Nanoscale imaging of RNA with expansion microscopy. *Nature methods* 13, 679-684.

Chozinski, T.J., Halpern, A.R., Okawa, H., Kim, H.J., Tremel, G.J., Wong, R.O., and Vaughan, J.C. (2016). Expansion microscopy with conventional antibodies and fluorescent proteins. *Nature methods* 13, 485-488.

Chozinski, T.J., Mao, C., Halpern, A.R., Pippin, J.W., Shankland, S.J., Alpers, C.E., Najafian, B., and Vaughan, J.C. (2018). Volumetric, Nanoscale Optical Imaging of Mouse and Human Kidney via Expansion Microscopy. *Scientific reports* 8, 10396.

Coffelt, S.B., Wellenstein, M.D., and de Visser, K.E. (2016). Neutrophils in cancer: neutral no more. *Nature reviews Cancer* 16, 431-446.

Conchello JA, Lichtman JW. Optical sectioning microscopy. *Nature methods*. 2005;2:920–931.

Conhaim, R.L., and Staub, N.C. (1980). Reflection spectrophotometric measurement of O₂ uptake in pulmonary arterioles of cats. *Journal of applied physiology: respiratory, environmental and exercise physiology* 48, 848-856.

Costa, E.C., Moreira, A.F., de Melo-Diogo, D., and Correia, I.J. (2018). Polyethylene glycol molecular weight influences the ClearT2 optical clearing method for spheroids imaging by confocal laser scanning microscopy. *Journal of biomedical optics* 23, 1-11.

Costantini, I., Cicchi, R., Silvestri, L., Vanzi, F., and Pavone, F.S. (2019). In-vivo and ex-vivo optical clearing methods for biological tissues: review. *Biomedical optics express* 10, 5251-5267.

Croce, A.C., and Bottiroli, G. (2014). Autofluorescence spectroscopy and imaging: a tool for biomedical research and diagnosis. *European journal of histochemistry: EJH* 58, 2461.

d'Esposito, A., Nikitichev, D., Desjardins, A., Walker-Samuel, S., and Lythgoe, M.F. (2015). Quantification of light attenuation in optically cleared mouse brains. *Journal of biomedical optics* 20, 80503.

Delgado, J.F., Conde, E., Sanchez, V., Lopez-Rios, F., Gomez-Sanchez, M.A., Escribano, P., Sotelo, T., Gomez de la Camara, A., Cortina, J., and de la Calzada, C.S. (2005). Pulmonary vascular remodeling in pulmonary hypertension due to chronic heart failure. *European journal of heart failure* 7, 1011-1016.

Dotd, H.U., Leischner, U., Schierloh, A., Jahrling, N., Mauch, C.P., Deininger, K., Deussing, J.M., Eder, M., Zieglgansberger, W., and Becker, K. (2007). Ultramicroscopy: three-dimensional visualization of neuronal networks in the whole mouse brain. *Nature methods* 4, 331-336.

Donskov, F. (2013). Immunomonitoring and prognostic relevance of neutrophils in clinical trials. *Seminars in cancer biology* 23, 200-207.

- Ebos, J.M., Lee, C.R., Cruz-Munoz, W., Bjarnason, G.A., Christensen, J.G., and Kerbel, R.S. (2009). Accelerated metastasis after short-term treatment with a potent inhibitor of tumor angiogenesis. *Cancer cell* 15, 232-239.
- Erturk, A., Becker, K., Jahrling, N., Mauch, C.P., Hojer, C.D., Egen, J.G., Hellal, F., Bradke, F., Sheng, M., and Dodt, H.U. (2012). Three-dimensional imaging of solvent-cleared organs using 3DISCO. *Nature protocols* 7, 1983-1995.
- Fridlender, Z.G., Sun, J., Kim, S., Kapoor, V., Cheng, G., Ling, L., Worthen, G.S., and Albelda, S.M. (2009). Polarization of tumor-associated neutrophil phenotype by TGF-beta: "N1" versus "N2" TAN. *Cancer cell* 16, 183-194.
- Fujisawa, S., Yarilin, D., Fan, N., Turkecul, M., Xu, K., Barlas, A., and Manova-Todorova, K. (2015). Understanding the three-dimensional world from two-dimensional immunofluorescent adjacent sections. *Journal of pathology informatics* 6, 27.
- Gandjeva, A., and Tuder, R.M. (2018). Lung Histological Methods. *Methods in molecular biology (Clifton, NJ)* 1809, 315-329.
- Ganesan, S., Comstock, A.T., and Sajjan, U.S. (2013). Barrier function of airway tract epithelium. *Tissue barriers* 1, e24997.
- Gao, C., Li, R., Huan, J., and Li, W. (2011). Caveolin-1 siRNA increases the pulmonary microvascular and alveolar epithelial permeability in rats. *The Journal of trauma* 70, 210-219.
- Gao, R., Asano, S.M., and Boyden, E.S. (2017). Q&A: Expansion microscopy. *BMC biology* 15, 50.
- Germroth, P.G., Gourdie, R.G., and Thompson, R.P. (1995). Confocal microscopy of thick sections from acrylamide gel embedded embryos. *Microscopy research and technique* 30, 513-520.
- Greenbaum, A., Jang, M.J., Challis, C., and Gradinaru, V. (2017). Q&A: How can advances in tissue clearing and optogenetics contribute to our understanding of normal and diseased biology? *BMC biology* 15, 87.
- Grüneboom, A., Hawwari, I., Weidner, D., Culemann, S., Müller, S., Henneberg, S., Brenzel, A., Merz, S., Bornemann, L., Zec, K., *et al.* (2019). A network of trans-cortical capillaries as mainstay for blood circulation in long bones. *Nature Metabolism* 1, 236-250.
- Hagendoorn, J., Tong, R., Fukumura, D., Lin, Q., Lobo, J., Padera, T.P., Xu, L., Kucherlapati, R., and Jain, R.K. (2006). Onset of abnormal blood and lymphatic vessel function and interstitial hypertension in early stages of carcinogenesis. *Cancer research* 66, 3360-3364.
- Hama, H., Hioki, H., Namiki, K., Hoshida, T., Kurokawa, H., Ishidate, F., Kaneko, T., Akagi, T., Saito, T., Saido, T., *et al.* (2015). ScaleS: an optical clearing palette for biological imaging. *Nature neuroscience* 18, 1518-1529.

Hama, H., Kurokawa, H., Kawano, H., Ando, R., Shimogori, T., Noda, H., Fukami, K., Sakaue-Sawano, A., and Miyawaki, A. (2011). Scale: a chemical approach for fluorescence imaging and reconstruction of transparent mouse brain. *Nature neuroscience* 14, 1481-1488.

Hanahan, D., and Weinberg, R.A. (2011). Hallmarks of cancer: the next generation. *Cell* 144, 646-674.

Harkness, L.M., Kanabar, V., Sharma, H.S., Westergren-Thorsson, G., and Larsson-Callerfelt, A.K. (2014). Pulmonary vascular changes in asthma and COPD. *Pulmonary pharmacology & therapeutics* 29, 144-155.

Hausmann, R. (2006). Methods of Lung Fixation. *Forensic Pathology Reviews vol 4*, 437-451.

Hausmann, R., Bock, H., Biermann, T., and Betz, P. (2004). Influence of lung fixation technique on the state of alveolar expansion-a histomorphometrical study. *Legal medicine (Tokyo, Japan)* 6, 61-65.

Heath, V.L., and Bicknell, R. (2009). Anticancer strategies involving the vasculature. *Nature reviews Clinical oncology* 6, 395-404.

Helmchen, F., and Denk, W. (2005). Deep tissue two-photon microscopy. *Nature methods* 2, 932-940.

Henning, Y., Osadnik, C., and Malkemper, E.P. (2019). EyeCi: Optical clearing and imaging of immunolabeled mouse eyes using light-sheet fluorescence microscopy. *Experimental eye research* 180, 137-145.

Herbst, R.S., Morgensztern, D., and Boshoff, C. (2018). The biology and management of non-small cell lung cancer. *Nature* 553, 446-454.

Hiratsuka, S., Watanabe, A., Aburatani, H., and Maru, Y. (2006). Tumour-mediated upregulation of chemoattractants and recruitment of myeloid cells predetermines lung metastasis. *Nature cell biology* 8, 1369-1375.

Holt, J.T., Jensen, R.A., and Page, D.L. (1993). Histopathology: old principles and new methods. *Cancer surveys* 18, 115-133.

Huang, J., Brenna, C., Khan, A.U.M., Daniele, C., Rudolf, R., Heuveline, V., and Gretz, N. (2019). A cationic near infrared fluorescent agent and ethyl-cinnamate tissue clearing protocol for vascular staining and imaging. *Scientific reports* 9, 521.

Jain, R.K. (2001). Normalizing tumor vasculature with anti-angiogenic therapy: a new paradigm for combination therapy. *Nature medicine* 7, 987-989.

Jain, R.K. (2005). Normalization of tumor vasculature: an emerging concept in antiangiogenic therapy. *Science (New York, NY)* 307, 58-62.

Jain, R.K. (2008). Taming vessels to treat cancer. *Scientific American* 298, 56-63.

James, A.L., Maxwell, P.S., Pearce-Pinto, G., Elliot, J.G., and Carroll, N.G. (2002). The relationship of reticular basement membrane thickness to airway wall remodeling in asthma. *American journal of respiratory and critical care medicine* 166, 1590-1595.

Jamme, F., Kascakova, S., Villette, S., Allouche, F., Pallu, S., Rouam, V., and Refregiers, M. (2013). Deep UV autofluorescence microscopy for cell biology and tissue histology. *Biology of the cell* 105, 277-288.

Jeffery, P., Holgate, S., and Wenzel, S. (2003). Methods for the assessment of endobronchial biopsies in clinical research: application to studies of pathogenesis and the effects of treatment. *American journal of respiratory and critical care medicine* 168, S1-17.

Jensen, K.H.R., and Berg, R.W. (2017). Advances and perspectives in tissue clearing using CLARITY. *Journal of chemical neuroanatomy* 86, 19-34.

Jiang, N., Kim, H.J., Chozinski, T.J., Azpurua, J.E., Eaton, B.A., Vaughan, J.C., and Parrish, J.Z. (2018). Superresolution imaging of *Drosophila* tissues using expansion microscopy. *Molecular biology of the cell* 29, 1413-1421.

Jin, L., and Lloyd, R.V. (1997). In situ hybridization: methods and applications. *Journal of clinical laboratory analysis* 11, 2-9.

Joyce, J.A., and Pollard, J.W. (2009). Microenvironmental regulation of metastasis. *Nature reviews Cancer* 9, 239-252.

Ke, M.-T., Fujimoto, S., and Imai, T. (2013). SeeDB: a simple and morphology-preserving optical clearing agent for neuronal circuit reconstruction. *Nature neuroscience* 16, 1154-1161.

Klingberg, A., Hasenberg, A., Ludwig-Portugall, I., Medyukhina, A., Mann, L., Brenzel, A., Engel, D.R., Figge, M.T., Kurts, C., and Gunzer, M. (2017). Fully Automated Evaluation of Total Glomerular Number and Capillary Tuft Size in Nephritic Kidneys Using Lightsheet Microscopy. *Journal of the American Society of Nephrology : JASN* 28, 452-459.

Kunz, T.C., Gotz, R., Sauer, M., and Rudel, T. (2019). Detection of Chlamydia Developmental Forms and Secreted Effectors by Expansion Microscopy. *Frontiers in cellular and infection microbiology* 9, 276.

Kuwajima, T., Sitko, A.A., Bhansali, P., Jurgens, C., Guido, W., and Mason, C. (2013). ClearT: a detergent- and solvent-free clearing method for neuronal and non-neuronal tissue. *Development (Cambridge, England)* 140, 1364-1368.

Lange, T., Nentwich, M.F., Luth, M., Yekebas, E., and Schumacher, U. (2011). Trastuzumab has anti-metastatic and anti-angiogenic activity in a spontaneous metastasis xenograft model of esophageal adenocarcinoma. *Cancer letters* 308, 54-61.

Lee, H., Park, J.H., Seo, I., Park, S.H., and Kim, S. (2014). Improved application of the electrophoretic tissue clearing technology, CLARITY, to intact solid organs including brain, pancreas, liver, kidney, lung, and intestine. *BMC developmental biology* 14, 48.

Lim, Y., Shiver, A.L., Khariton, M., Lane, K.M., Ng, K.M., Bray, S.R., Qin, J., Huang, K.C., and Wang, B. (2019). Mechanically resolved imaging of bacteria using expansion microscopy. *PLoS biology* 17, e3000268.

Longmire, M., Choyke, P.L., and Kobayashi, H. (2008). Clearance properties of nano-sized particles and molecules as imaging agents: considerations and caveats. *Nanomedicine (London, England)* 3, 703-717.

Marx, V. (2014). Microscopy: seeing through tissue. *Nature methods* 11, 1209-1214.

Masselink, W., Reumann, D., Murawala, P., Pasierbek, P., Taniguchi, Y., Bonnay, F., Meixner, K., Knoblich, J.A., and Tanaka, E.M. (2019). Broad applicability of a streamlined ethyl cinnamate-based clearing procedure. *Development (Cambridge, England)* 146, dev166884.

Mayekar, M.K., and Bivona, T.G. (2017). Current Landscape of Targeted Therapy in Lung Cancer. *Clinical pharmacology and therapeutics* 102, 757-764.

Monici, M. (2005). Cell and tissue autofluorescence research and diagnostic applications. *Biotechnology annual review* 11, 227-256.

Moy, A.J., Wiersma, M.P., and Choi, B. (2013). Optical histology: a method to visualize microvasculature in thick tissue sections of mouse brain. *PLoS one* 8, e53753.

Munkholm, M., and Mortensen, J. (2014). Mucociliary clearance: pathophysiological aspects. *Clinical physiology and functional imaging* 34, 171-177.

Murillo, H., Cutalo, M.J., Jones, R.P., Lane, M.J., Fleischmann, D., and Restrepo, C.S. (2012). Pulmonary circulation imaging: embryology and normal anatomy. *Seminars in ultrasound, CT, and MR* 33, 473-484.

Murray, E., Cho, J.H., Goodwin, D., Ku, T., Swaney, J., Kim, S.Y., Choi, H., Park, Y.G., Park, J.Y., Hubbert, A., *et al.* (2015). Simple, Scalable Proteomic Imaging for High-Dimensional Profiling of Intact Systems. *Cell* 163, 1500-1514.

Negrini, D., and Moriondo, A. (2013). Pleural function and lymphatics. *Acta physiologica (Oxford, England)* 207, 244-259.

Nojima, S., Susaki, E.A., Yoshida, K., Takemoto, H., Tsujimura, N., Iijima, S., Takachi, K., Nakahara, Y., Tahara, S., Ohshima, K., *et al.* (2017). CUBIC pathology: three-dimensional imaging for pathological diagnosis. *Scientific reports* 7, 9269.

Ochoa, L.F., Kholodnykh, A., Villarreal, P., Tian, B., Pal, R., Freiberg, A.N., Brasier, A.R., Motamedi, M., and Vargas, G. (2018). Imaging of Murine Whole Lung Fibrosis by Large Scale 3D Microscopy aided by Tissue Optical Clearing. *Scientific reports* 8, 13348.

Ostrand-Rosenberg, S. (2008). Immune surveillance: a balance between protumor and antitumor immunity. *Current opinion in genetics & development* 18, 11-18.

Paez-Ribes, M., Allen, E., Hudock, J., Takeda, T., Okuyama, H., Vinals, F., Inoue, M., Bergers, G., Hanahan, D., and Casanovas, O. (2009). Antiangiogenic therapy elicits malignant progression of tumors to increased local invasion and distant metastasis. *Cancer cell* 15, 220-231.

Palmer, W.M., Flynn, J.R., Martin, A.P., Reed, S.L., Grof, C.P.L., White, R.G., and Furbank, R.T. (2018). 3D Clearing and Molecular Labeling in Plant Tissues. *Methods in molecular biology* (Clifton, NJ) 1770, 285-304.

Pan, C., Cai, R., Quacquarelli, F.P., Ghasemigharagoz, A., Loubopoulos, A., Matryba, P., Plesnila, N., Dichgans, M., Hellal, F., and Erturk, A. (2016). Shrinkage-mediated imaging of entire organs and organisms using uDISCO. *Nature methods* 13, 859-867.

Peng, C.K., Huang, K.L., Wu, C.P., Wu, Y.K., Tzeng, I.S., and Lan, C.C. (2019). Phosphodiesterase-4 Inhibitor Roflumilast Attenuates Pulmonary Air Emboli-Induced Lung Injury. *The Journal of surgical research* 241, 24-30.

Persson, C.G. (1996). Epithelial cells: barrier functions and shedding-restitution mechanisms. *American journal of respiratory and critical care medicine* 153, S9-10.

Quail, D.F., and Joyce, J.A. (2013). Microenvironmental regulation of tumor progression and metastasis. *Nature medicine* 19, 1423-1437.

Redington, A.E., and Howarth, P.H. (1997). Airway wall remodelling in asthma. *Thorax* 52, 310-312.

Reid, L. (1965). The angiogram and pulmonary artery structure and branching (in the normal and with reference to disease). *Proceedings of the Royal Society of Medicine* 58, 681-684.

Renier, N., Wu, Z., Simon, D.J., Yang, J., Ariel, P., and Tessier-Lavigne, M. (2014). iDISCO: a simple, rapid method to immunolabel large tissue samples for volume imaging. *Cell* 159, 896-910.

Reynaud, E.G., Krzic, U., Greger, K., and Stelzer, E.H. (2008). Light sheet-based fluorescence microscopy: more dimensions, more photons, and less photodamage. *HFSP journal* 2, 266-275.

Richardson, D.S., and Lichtman, J.W. (2015). Clarifying Tissue Clearing. *Cell* 162, 246-257.

Rivenson, Y., Wang, H., Wei, Z., de Haan, K., Zhang, Y., Wu, Y., Gunaydin, H., Zuckerman, J.E., Chong, T., Sisk, A.E., *et al.* (2019). Virtual histological staining of unlabelled tissue-autofluorescence images via deep learning. *Nature biomedical engineering* 3, 466-477.

Robinson, D.R., Wu, Y.M., Lonigro, R.J., Vats, P., Cobain, E., Everett, J., Cao, X., Rabban, E., Kumar-Sinha, C., Raymond, V., *et al.* (2017). Integrative clinical genomics of metastatic cancer. *Nature* 548, 297-303.

Robinson, M., Eberl, S., Tomlinson, C., Daviskas, E., Regnis, J.A., Bailey, D.L., Torzillo, P.J., Menache, M., and Bye, P.T. (2000). Regional mucociliary clearance in patients with cystic fibrosis. *Journal of aerosol medicine : the official journal of the International Society for Aerosols in Medicine* 13, 73-86.

Ronca, R., Benkheil, M., Mitola, S., Struyf, S., and Liekens, S. (2017). Tumor angiogenesis revisited: Regulators and clinical implications. *Medicinal research reviews* 37, 1231-1274.

Ryan, D.P., Gould, E.A., Seedorf, G.J., Masihzadeh, O., Abman, S.H., Vijayaraghavan, S., Macklin, W.B., Restrepo, D., and Shepherd, D.P. (2017). Automatic and adaptive heterogeneous refractive index compensation for light-sheet microscopy. *Nature communications* 8, 612.

Saetta, M., Turato, G., Maestrelli, P., Mapp, C.E., and Fabbri, L.M. (2001). Cellular and structural bases of chronic obstructive pulmonary disease. *American journal of respiratory and critical care medicine* 163, 1304-1309.

Saritas, T., Puelles, V.G., Su, X.T., Ellison, D.H., and Kramann, R. (2019). Optical Clearing and Imaging of Immunolabeled Kidney Tissue. *Journal of visualized experiments: JoVE* 149, e60002.

Saritas, T., Puelles, V.G., Su, X.T., McCormick, J.A., Welling, P.A., and Ellison, D.H. (2018). Optical Clearing in the Kidney Reveals Potassium-Mediated Tubule Remodeling. *Cell reports* 25, 2668-2675.e2663.

Schmiesing, G.A. (2004). Transportation, vaccination, eradication, consolidation: reasons for consternation? *Veterinary heritage : bulletin of the American Veterinary History Society* 27, 35-41.

Seo, J., Choe, M., and Kim, S.Y. (2016). Clearing and Labeling Techniques for Large-Scale Biological Tissues. *Molecules and cells* 39, 439-446.

Serna, N., Sanchez-Garcia, L., Unzueta, U., Diaz, R., Vazquez, E., Mangues, R., and Villaverde, A. (2018). Protein-Based Therapeutic Killing for Cancer Therapies. *Trends in biotechnology* 36, 318-335.

Shahneh, F.Z., Baradaran, B., Zamani, F., and Aghebati-Maleki, L. (2013). Tumor angiogenesis and anti-angiogenic therapies. *Human antibodies* 22, 15-19.

Siegel, R.L., Miller, K.D., and Jemal, A. (2018). Cancer statistics, 2018. *CA: a cancer journal for clinicians* 68, 7-30.

Silvestri, L., Costantini, I., Sacconi, L., and Pavone, F.S. (2016). Clearing of fixed tissue: a review from a microscopist's perspective. *Journal of biomedical optics* 21, 081205.

Spalteholz W. *Über das Durchsichtigmachen von menschlichen und tierischen Präparaten.* Leipzig: S. Hierzel; 1914

- Susaki, E.A., Tainaka, K., Perrin, D., Kishino, F., Tawara, T., Watanabe, T.M., Yokoyama, C., Onoe, H., Eguchi, M., Yamaguchi, S., *et al.* (2014). Whole-brain imaging with single-cell resolution using chemical cocktails and computational analysis. *Cell* *157*, 726-739.
- Susaki, E.A., Tainaka, K., Perrin, D., Yukinaga, H., Kuno, A., and Ueda, H.R. (2015). Advanced CUBIC protocols for whole-brain and whole-body clearing and imaging. *Nature protocols* *10*, 1709-1727.
- Syed, A.M., Sindhvani, S., Wilhelm, S., Kingston, B.R., Lee, D.S.W., Gommerman, J.L., and Chan, W.C.W. (2017). Three-Dimensional Imaging of Transparent Tissues via Metal Nanoparticle Labeling. *Journal of the American Chemical Society* *139*, 9961-9971.
- Thurber, G.M., and Weissleder, R. (2011). A systems approach for tumor pharmacokinetics. *PLoS one* *6*, e24696.
- Tillberg, P.W., and Chen, F. (2019). Expansion Microscopy: Scalable and Convenient Super-Resolution Microscopy. *Annual review of cell and developmental biology* *35*, 683-701.
- Tomer, R., Khairy, K., Amat, F., and Keller, P.J. (2012). Quantitative high-speed imaging of entire developing embryos with simultaneous multiview light-sheet microscopy. *Nature methods* *9*, 755-763.
- Tomer, R., Ye, L., Hsueh, B., and Deisseroth, K. (2014). Advanced CLARITY for rapid and high-resolution imaging of intact tissues. *Nature protocols* *9*, 1682-1697.
- Townsley, M.I. (2012). Structure and composition of pulmonary arteries, capillaries, and veins. *Comprehensive Physiology* *2*, 675-709.
- Treweek, J.B., Chan, K.Y., Flytzanis, N.C., Yang, B., Deverman, B.E., Greenbaum, A., Lignell, A., Xiao, C., Cai, L., Ladinsky, M.S., *et al.* (2015). Whole-body tissue stabilization and selective extractions via tissue-hydrogel hybrids for high-resolution intact circuit mapping and phenotyping. *Nature protocols* *10*, 1860-1896.
- Wan, P., Zhu, J., Xu, J., Li, Y., Yu, T., and Zhu, D. (2018). Evaluation of seven optical clearing methods in mouse brain. *Neurophotonics* *5*, 035007.
- Wang, H., Rivenson, Y., Jin, Y., Wei, Z., Gao, R., Gunaydin, H., Bentolila, L.A., Kural, C., and Ozcan, A. (2019). Deep learning enables cross-modality super-resolution in fluorescence microscopy. *Nature methods* *16*, 103-110.
- Wang, L.F., White, D.R., Andreoli, S.M., Mulligan, R.M., Discolo, C.M., and Schlosser, R.J. (2012). Cigarette smoke inhibits dynamic ciliary beat frequency in pediatric adenoid explants. *Otolaryngology--head and neck surgery : official journal of American Academy of Otolaryngology-Head and Neck Surgery* *146*, 659-663.
- Wassie, A.T., Zhao, Y., and Boyden, E.S. (2019). Expansion microscopy: principles and uses in biological research. *Nature methods* *16*, 33-41.

- Wculek, S.K., and Malanchi, I. (2015). Neutrophils support lung colonization of metastasis-initiating breast cancer cells. *Nature* 528, 413-417.
- Wellings, S.R., and Jensen, H.M. (1973). On the origin and progression of ductal carcinoma in the human breast. *Journal of the National Cancer Institute* 50, 1111-1118.
- Wellings, S.R., Jensen, H.M., and Marcum, R.G. (1975). An atlas of subgross pathology of the human breast with special reference to possible precancerous lesions. *Journal of the National Cancer Institute* 55, 231-273.
- West, J.B. (2013). Fragility of pulmonary capillaries. *Journal of applied physiology* (Bethesda, Md : 1985) 115, 1-15.
- Woo, J., Lee, M., Seo, J.M., Park, H.S., and Cho, Y.E. (2016). Optimization of the optical transparency of rodent tissues by modified PACT-based passive clearing. *Experimental & molecular medicine* 48, e274.
- Wu, N.H., Yang, W., Beineke, A., Dijkman, R., Matrosovich, M., Baumgartner, W., Thiel, V., Valentin-Weigand, P., Meng, F., and Herrler, G. (2016). The differentiated airway epithelium infected by influenza viruses maintains the barrier function despite a dramatic loss of ciliated cells. *Scientific reports* 6, 39668.
- Xu, J., Ma, Y., Yu, T., and Zhu, D. (2019). Quantitative assessment of optical clearing methods in various intact mouse organs. *Journal of biophotonics* 12, e201800134.
- Yu, T., Qi, Y., Gong, H., Luo, Q., and Zhu, D. (2018). Optical clearing for multiscale biological tissues. *Journal of biophotonics* 11.
- Yu, T., Qi, Y., Zhu, J., Xu, J., Gong, H., Luo, Q., and Zhu, D. (2017). Elevated-temperature-induced acceleration of PACT clearing process of mouse brain tissue. *Scientific reports* 7, 38848.
- Zhao, Y., Bucur, O., Irshad, H., Chen, F., Weins, A., Stancu, A.L., Oh, E.Y., DiStasio, M., Torous, V., Glass, B., *et al.* (2017). Nanoscale imaging of clinical specimens using pathology-optimized expansion microscopy. *Nature biotechnology* 35, 757-764.

7 APPENDIX (PUBLICATION)

1. Brenna C., Khan A.U.M., Picascia T., **Sun Q.C.**, Heuveline V., Gretz N. (2020).
New technical approaches for 3D imaging and quantification of measurements.
The Anatomical Record. (Accepted; Article DOI: 10.1002/ar.24463).

8 CURRICULUM VITAE

PERSONNEL

Name und Surname: Quanchao Sun.....
Date of birth: 20/03/1990.....
Place of birth: Jiangxi, China.....
Marital status: Married.....
Father: Zetin Sun.....
Mother: Aide Zhang.....

SCHOOL CAREER

(2004) – (2007) Jin An high school
(08/06/2007) High school certificate

UNIVERSITIES

WS 2007/09 Clinical Medicine
Jiujiang University

(10/07/2012) Bachelor's degree

(2012) – (2015) Diploma/Master thesis (Title):
Maresin 1 attenuates acute lung ischemia reperfusion injury
in mice

(19/06/2015) Master's degree

9 ACKNOWLEDGMENTS

Time is a bird forever on the wing. For the past two years' doctor degree of medicine study, I really have a meaningful and fulfilling experience in our Medical Research Center (ZMF) of the Medical Faculty Mannheim of the University of Heidelberg. Not only have I met so many professional and helpful teachers, but also kind colleagues and friends. I would like to give my deep gratitude to all of them.

First of all I want to give my sincere thanks to my supervisor, Prof. Dr. med. Norbert Gretz, who offered me the precious opportunity to study abroad from China. Without his suggestions and encouragement, it would be a tough task for me to finish my scientific project. In the preparation of this thesis, he had spent so much time reading and editing each drafts and provided me with so many inspiring advices.

Special thanks go to the other teachers and secretaries of our ZMF who helped me to solve so many problems with patience and gave me important guidance during my doctoral study. Thanks to all of my colleagues from Germany, Italy, India, Spain, Chile, Colombia and China. They never stopped giving kind help to me whenever I needed support in my experiment. I learned so much from them and they made my life and study happy in Germany.

At last, I would like to express my special thanks to my family, who always supported me and gave me the power to go on and to face any situation.

No matter how my career will develop after graduation, the experience of live and study in Germany and Europe definitely will make a big difference for my whole lifetime.